2018

2d Materials For Energy Applications

Dequan Er
University of Pennsylvania, erdeq.upenn@gmail.com

Recommended Citation

Er, Dequan, "2d Materials For Energy Applications" (2018). *Publicly Accessible Penn Dissertations*. 2875.
https://repository.upenn.edu/edissertations/2875

2d Materials For Energy Applications

Abstract

Accelerated energy demands, together with unprecedented CO2 emissions, aggravate the global energy and climate change crises, endangering the sustainable development of society in a perpetuity way. The ability to find, extract, and use energy in an effective and clean way is pivotal to the energy paradigm shift, where a large percentage of global energy demand is expected to be met through sustainable energy resources. Research in materials science is contributing towards such a sustainable future by addressing bottleneck questions in energy storage and conversion, which are two main parts of energy sustainability. In particular, recently discovered two-dimensional (2D) materials exhibit extraordinary mechanical, chemical, electronic, optical, and magnetic properties that are promising to break through current material limitations in energy applications. The main goal of this thesis is to examine the possibility of using 2D materials in improving current energy applications, in particular, battery electrodes and hydrogen evolution reaction (HER) catalysts, and to elucidate the mechanisms and guiding principles in tuning 2D materials using combinatorial simulation techniques that bridge different length scales. Representative and promising 2D material systems, including graphene-like materials, MXenes, transition metal dichalcogenides (TMDs), layered covalent-organic framework (COF), and oxides are studied. To evaluate the performance of 2D materials in battery electrodes, we employ the density functional theory (DFT) simulations to investigate the adsorption of different metal ions onto 2D MXenes and 2D graphene-like materials, and hence quantify the enhanced theoretical capacities and rate-performance. Moreover, we find the origin of such improvements and summarize guiding principles in tuning 2D materials for similar applications in batteries beyond lithium. We also show that 2D TMDs are capable of improving hydrogen production efficiency. The role of defects and electronic coupling between substrate and MoS2 catalysts is investigated, followed by a study of using the Janus asymmetry as a feasible way to activate basal plane catalytic activity. Finally, we present a multiscale modeling method that bridges different length scales, and show several successful examples in applying this method in energy applications. This thesis provides new understandings of 2D materials in energy applications. Such understandings may be used to accelerate the realization of future energy plan.

Degree Type

Dissertation

Degree Name

Doctor of Philosophy (PhD)

Graduate Group

Materials Science & Engineering

First Advisor

Vivek B. Shenoy

Keywords

2D materials, battery, catalysts, electrodes, energy applications, multiscale modeling

Subject Categories

Mechanics of Materials | Oil, Gas, and Energy

2D MATERIALS FOR ENERGY APPLICATIONS

Dequan Er

A DISSERTATION

in

Materials Science and Engineering

Presented to the Faculties of the University of Pennsylvania

in

Partial Fulfillment of the Requirements for the

Degree of Doctor of Philosophy

2018

Supervisor of Dissertation

____

Vivek B. Shenoy, Ph.D.
Director, NSF Science and Technology Center for Mechanobiology
Eduardo D. Glandt President's Distinguished Professor, Department of Materials Science and Engineering, Department of Bioengineering, Department of Mechanical Engineering and Applied Mechanics, University of Pennsylvania

Graduate Group Chairperson

____

David J. Srolovitz, Ph.D.
Joseph Bordogna Professor, Materials Science and Engineering, University of Pennsylvania

Dissertation Committee

Yury Gogotsi, Ph.D., D.Sc., Dr.h.c.
Charles T. and Ruth M. Bach Distinguished University Professor
Director, A.J. Drexel Nanomaterials Institute, Drexel University

Raymond J. Gorte, Ph.D.
Russell Pearce and Elizabeth Crimian Heuer Professor, Chemical and Biomolecular Engineering, University of Pennsylvania

Vaclav Vitek, Ph.D.
Harold Pender Professor, Materials Science and Engineering, University of Pennsylvania

2D MATERIALS FOR ENERGY APPLICATIONS

To my family and in memory of my grandfather

ACKNOWLEDGMENT

I am sincerely grateful to my advisor, Professor Vivek Shenoy, who have sharp eyes in seeing the underlying physics of problems and have played a significant role in inspiring my current understanding of computational materials science. His guidance, training, support, and patience are invaluable to the success in my career, and I feel proud and honored to spend my five years to follow such a smart and world-class scientist. I am profoundly thankful to my collaborators and committee members, Professor Yury Gogotsi, Professor Raymond J. Gorte, and Professor Vaclav Vitek, for their guidance, suggestions, patience, and time.

I would like to present my warmest gratitude to Dr. Junwen Li, who teaches me simulation softwares from scratch and encourages me during hard times. I also want to extend my thanks to collaborators, Dr. Michael Naguib, Dr. Manish Chhowalla, Dr. Jun Lou, Dr. Eric Detsi, Dr. Matteo Cargnello, Dr. Hemant Kumar, Dr. Liang Dong, Dr. Han Ye, Hong Zhong, and Nathan Frey. Moreover, I would like to give my gratitude to my colleagues in Shenoy's lab, current and former postdoc fellows and graduate students for our collaborations and friendship over these years. Many of my ideas are sharpened through beneficial discussions with Dr. Jian Han, Dr. Yanhao Dong, Dr. Wenjing Liu, Dr. Hailong Wang, Dr. Shuyang Dai, Dr. Dibakar Datta, Dr. Hossein Ahmadzadeh, Dr. Jibing Sun, Songsong Zhou, Liyan Wu, Tianshuo Zhao, and my roommate Dr. Yuan Li. I am thankful to all my friends here at Penn and around the world for their years friendship with me, including Yolanda Chen, Ruiyuan Ma, Dongliang Wang, Xuan Cao, Ze Gong, Hye-na Kim, Noa Hegesh, Han Wang at Penn, Haichen Gu in China, Han Yan in Japan, and Yuan in Germany.

Finally, I cannot go this far without the love, support and freedom from my family, especially my parents and parents in law. Their full support and encouragement always accompany my journey. Of course, I would like to thank my wife, Wei Miao, for her love, encouragement, and sweet memories.

ABSTRACT

2D MATERIALS FOR ENERGY APPLICATIONS

Dequan Er

Professor Vivek Shenoy

Accelerated energy demands, together with unprecedented CO_2 emissions, aggravate the global energy and climate change crises, endangering the sustainable development of society in a perpetuity way. The ability to find, extract, and use energy in an effective and clean way is pivotal to the energy paradigm shift, where a large percentage of global energy demand is expected to be met through sustainable energy resources. Research in materials science is contributing towards such a sustainable future by addressing bottleneck questions in energy storage and conversion, which are two main parts of energy sustainability. In particular, recently discovered two-dimensional (2D) materials exhibit extraordinary mechanical, chemical, electronic, optical, and magnetic properties that are promising to break through current material limitations in energy applications. The main goal of this thesis is to examine the possibility of using 2D materials in improving current energy applications, in particular, battery electrodes and hydrogen evolution reaction (HER) catalysts, and to elucidate the mechanisms and guiding principles in tuning 2D materials using combinatorial simulation techniques that bridge different length scales. Representative and promising 2D material systems, including graphene-like materials, MXenes, transition metal dichalcogenides (TMDs), layered covalent-organic framework (COF), and oxides are studied. To evaluate the performance of 2D materials in battery electrodes, we employ the density functional theory (DFT) simulations to investigate the adsorption of different metal ions onto 2D MXenes and 2D graphene-like materials, and hence quantify the enhanced theoretical capacities and rate-performance. Moreover, we find the origin of such improvements and summarize guiding principles in tuning 2D materials for similar applications in batteries beyond lithium. We also show that 2D TMDs are capable of improving hydrogen production efficiency. The role of defects and electronic coupling between substrate and MoS_2 catalysts is investigated, followed by a study of using the Janus asymmetry as a feasible way to activate basal plane catalytic activity. Finally, we present a multiscale modeling method that bridges different length scales, and show several successful examples in applying this method in energy applications. This thesis provides new understandings of 2D materials in energy applications. Such understandings may be used to accelerate the realization of future energy plan.

TABLE OF CONTENTS

LIST OF TABLES

LIST OF ILLUSTRATIONS

PREFACE

Chapter 2 to Chapter 8 of this thesis have appeared in the following publications:

1. **D. Er**, J. Li, M. Naguib, Y. Gogosti, and V. B. Shenoy. *Ti_3C_2 MXene as a High Capacity Electrode Material for Metal (Li, Na, K, Ca)-ion Batteries*. **ACS Applied Materials & Interfaces**, 6(14): 11173-11179 June 2014
2. P. Urbankowski, B. Anasori, T. Makaryan, **D. Er**, S. Kota, P. Walsh, M. Zhao, V. B. Shenoy, M. W. Barsoum, and Y. Gogotsi. *Synthesis of Two-dimensional Titanium Nitride Ti_4N_3 (MXene)*. **Nanoscale**, 8:11385-11391 May 2016
3. **D. Er**, E. Detsi, H. Kumar, and V. B. Shenoy. *Defective Graphene and Graphene Allotropes as High Capacity Anode Materials for Mg-ion Batteries*. **ACS Energy Letters**, 1, 638-645 August 2016
4. D. Voiry, R. Fullon, J. Yang, C. Silva, R. Kappera, I. Bozkurt, D. Kaplan, M. J. Lagos, P. E. Batson, G. Gupta, A. D. Mohite, L. Dong, **D. Er**, V. B. Shenoy, T. Asefa, and M. Chhowalla. *The Role of Electronic Coupling between Substrate and 2D MoS_2 Nanosheets on Electro-Catalytic Production of Hydrogen*. **Nature Materials**, 15, 1003–1009 June 2016
5. **D. Er**, H. Ye, N. C. Frey, H. Kumar, J. Lou, and V. B. Shenoy. *Prediction of Significantly Enhanced Catalytic Activity for Hydrogen Evolution Reaction in Janus Transitional Metal Dichalcogenides*. **Nano Letters**, Accepted
6. H. Kumar, **D. Er**, L. Dong, J. Li, and V. B. Shenoy. *Elastic Deformations in 2D van der waals Heterostructures and their Impact on Optoelectronic Properties: Predictions from a Multiscale Computational Approach*. **Scientific Reports**, 5:10872 June 2015

7. **D. Er**, L. Dong, and V. B. Shenoy. *Mechanisms for Engineering Highly Anisotropic Conductivity in a Layered Covalent Organic Framework*. **Journal of Physical Chemistry C**, 120(1): 174-178 December 2015
8. **D. Er**, J. Li, M. Cargnello, P. Fornasiero, R. J. Gorte, and V. B. Shenoy. *A Model to Determine the Chemical Expansion in Non-stoichiometric Oxides Based on the Elastic Force Dipole*. **Journal of the Electrochemical Society**, 161 (11): F3060-F3064 September 2014

The following publications that I co-authored during my PhD study are not presented in this thesis:

1. S. Najmaei, X. Zou, **D. Er**, J. Li, Z. Jin, W. Gao, Q. Zhang, S. Park, L. Ge, S. Lei, J. Kono, V. B. Shenoy, B. I. Yakobson, A. George, P. M. Ajayan, and J. Lou. *Tailoring the Physical Properties of Molybdenum Disulphide Monolayers by Control of Interfacial Chemistry*. **Nano Letters**, 14(3): 1354-1361 February 2014
2. L. Dong, Y. Kim, **D. Er**, A. M. Rappe, and V. B. Shenoy. *2-Dimensonal π-conjugated Covalent-Organic Frameworks as Quantum Anomalous Hall Topological Insulators*. **Physical Review Letters**, 116:096601 February 2016
3. J. Zhang, S. Jia, K. Iskandar, L. Dong, **D. Er**, W. Chen, H. Guo, Z. Jin, V. B. Shenoy, L. Shi, and J. Lou. *Janus Monolayer Transition Metal Dichalcogenides.* **ACS Nano**, 11(8): 8192-8198 August 2017
4. H. Ye, J. Zhou, **D. Er**, C. Price, Z. Yu, Y. Liu, J. Lowengrub, J. Lou, Z. Liu, and V. B. Shenoy. *Toward a Mechanistic Understanding of Vertical Growth of van der Waals Stacked 2D Materials: A Multiscale Model and Experiments.* **ACS Nano**, 11(12): 12780-12788 December 2017.

5. N.C. Frey, B. Byles, H. Kumar, **D. Er**, E. Pomerantseva, and V. B. Shenoy. *Prediction of optimal structural water concentration for maximized performance in tunnel manganese oxide electrodes.* **Phys. Chem. Chem. Phys.,** In press
6. H. Zhong, **D. Er**, L. Dong, and L. Wen. *Theoretical study on the poly(m-phenylene) derivatives with lower HOMO–LUMO gaps.* **Synthetic Metals**, 229, 16-21 July 2017
7. H. Zhong, **D. Er**, and L. Wen. *Theoretical study on influence of CaO and MgO on the reduction of FeO by CO.* **Applied Surface Science**, 399, 630-637 March 2017

Chapter 1 Introduction

1.1 Introduction

The utilization of energy has accompanied the development of mankind since the first lit of fire that brings brightness, warmth, and cooked food. The discovery and utilization of coal, which is a deposit of solar energy into buried plants millions or billions of years ago, further drive the ancient civilization. Steam engines and electricity powered by coal are indispensable to the industrial revolution in 18th century. Later, petroleum brings us not only higher density fuels to power our vehicles but also chemical products such as plastics, resin, rubber, and fibers. Fossil fuels including coal, oil, and nature gas are primary energy sources in our modern society, and their consumption is rapidly increasing, posing economic and environmental challenges to the society. By 2050, the global energy consumption will rise by 28% in total, while nonmembers of Organization for Economic Cooperation and Development (OECD) will increase at a speed of 41%.[1,2] This is a significant increase in energy demand not only to countries who have the majority of world population, but also to the global energy landscape. Such accelerated energy consumption depletes fossil fuels faster and results in more emissions of green-house gas including oxides of carbon, nitrogen, sulfur, etc. It should be noted that the major sectors of energy demand increase are electric power, industry, and transportation, where new technologies that maximize the energy efficiency and mitigate the CO_2 emission are pivotal. It is an imperative to systematically optimize our energy landscape by 1) increasing the efficiency of current devices and infrastructures to minimize the energy waste, 2) searching and realizing alternative and sustainable clean resources, and 3) increasing the proportion of non-fossil fuels to further mitigate CO_2 emissions.

To fulfill this goal, the two keys are energy storage and energy conversion, where challenges for material scientists remain. First, energy storage devices are critical to improve the efficiency of energy applications systematically. These devices, including batteries, capacitors, flywheels, compressed air, fuel cells, and pumped hydro, engage widely in energy applications, and a large portion of energy waste occurs during the deposition and extraction inside these energy storage devices. Therefore, the high performance of energy storage devices is indispensable in 1) converting and storing intermittent renewable resources into current power grids, 2) transforming continuous on-grid electricity into discrete forms for constant and stable individual and commercial use. Among different energy storage devices, battery is the most promising one due to its high energy density, portable size, safety, compatibility, and high efficiency.[3] Not only the boom of electronics, but also recent development in electric vehicles (EVs) require higher capacity, lower cost, more compact, and more efficient batteries, extending the battery application from consumer to transportation sector. However, the bottleneck is that currently used electrode materials in batteries operate close to their theoretical limit.[4] Therefore, it is urgent to find next-generation material systems as promising battery electrodes.[5] Second, it is necessary to find renewable alternatives to fossil fuels. Renewable energy from water splitting, wind, solar, and biomass can provide good amount of energy to the grid cleanly and sustainably. Among them, hydrogen, which is a high energy density and a zero-emission fuel whose only byproduct is H_2O after combustion, holds promise for use in applications such as hydrogen fuel-cell vehicles and portable electronics. It is again aligned with the main energy demand sectors; therefore, the low-cost, high-efficiency production of hydrogen is pivotal. To address the current difficulty, that is only very few percent of hydrogen is produced from renewable sources through water electrolysis while the rest of it is still derived from fossil fuels, a low-cost and high-performance catalyst for

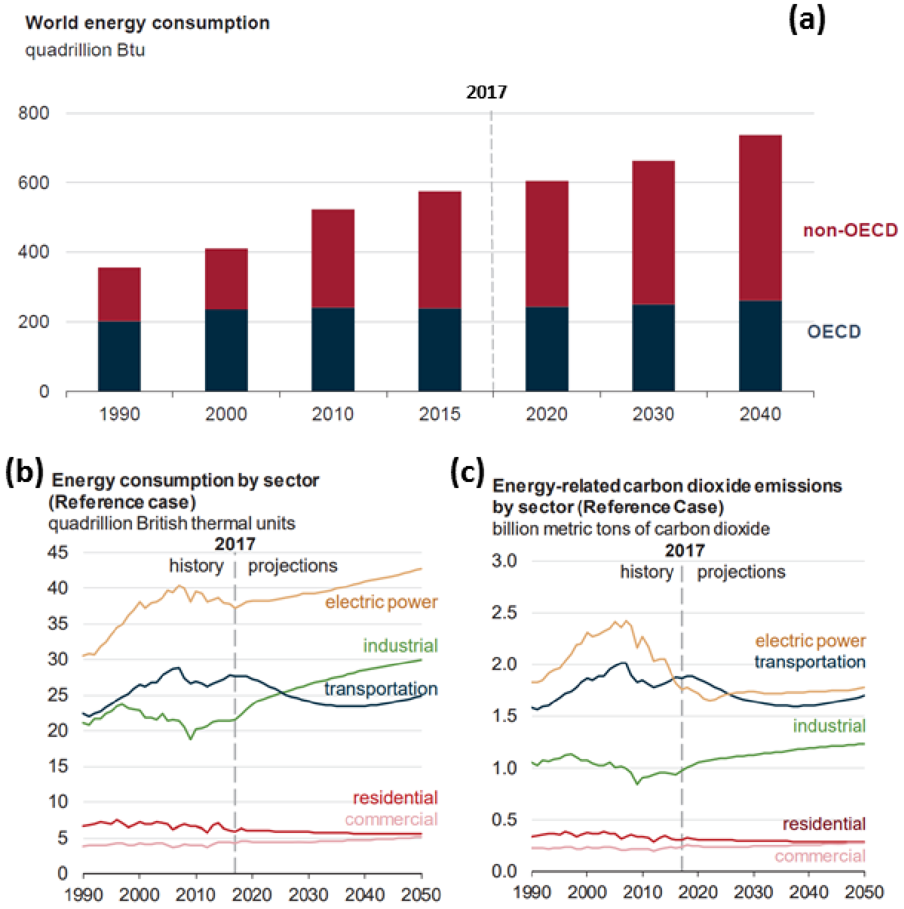

Figure 1-1 Energy consumptions worldwide. **(a)** Historical and projected fuel consumption of OECD and non-OECD countries. **(b)** energy consumption by sector, and **(c)** corresponding CO_2 emissions in US. Adapted from Ref 1,2.

hydrogen evolution reaction (HER) is needed. Currently used alloy or noble metal catalysts such as platinum (Pt) are expensive and scarce. In the past decades, significant efforts have been made in searching for the low-cost, earth-abundant, and non-toxic alternatives of the Pt-group metals catalysts in various material systems such as metal alloys, chalcogenides, nitrides, phosphides, borides, and carbides.[6–14]

Recently realized two-dimensional (2D) materials are a promising solution to the aforementioned energy storage and energy conversion problems, due to their unique morphology and tunable electrical, chemical, optical, and mechanical properties.[15] The first realized 2D material, graphene, is promising with some properties close to theoretical limits such as extreme large surface-to-mass ratio, high electron mobility at room temperature (2.5×10^5 $cm^2V^{-1}s^{-1}$), excellent mechanical behavior (Young’s modulus > 1TPa), and very high thermal conductivity (> 3000 W mK^{-1}).[15–18] Not only do graphene offer us a new way to think of solving material challenges in energy applications, its successors in the 2D materials family present us a rich, flexible, and unprecedented possibility in energy applications. The expanded 2D material family includes layered 2D oxides, MXenes (transition metal carbides and nitrides), 2D transition metal dichalcogenides (TMDs), and graphene-like materials (hexagonal boron nitride h-BN, graphene allotropes, phosphene, germanene).[19] Moreover, a much wider material portfolio is offered by stacking these 2D materials, forming heterostructures that are very different from their traditional 3D counterparts or 2D monolayers.[14,19] For example, band-gap engineering can be achieved simply by changing the number of layers, hence enabling atomic-thin transistors and electronic devices.[15,20] Likewise, 2D TMDs have been demonstrated as a promising alternative catalyst in various forms for HER applications due to its unique crystal , chemical, and electronic properties.[6,7,21–23] These new discovered 2D materials expand the current functional material scope and deserve detailed studies in the structure, methods of synthesis, transferring, scaling, and most importantly tailoring in mechanical, optical, magnetic, electronic, and chemical properties for desired energy applications.[24]

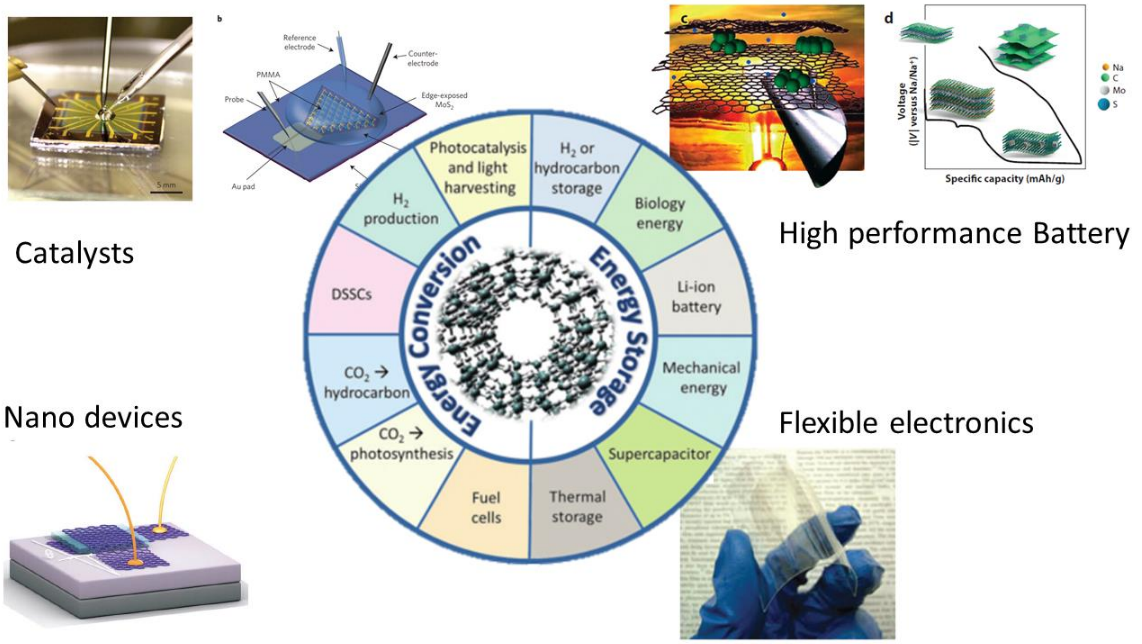

Figure 1-2 Selected promising applications of 2D materials. Reprint from Ref. 22,263 with permissions.

1.1.1 Energy storage devices beyond LIBs

Each cell of battery stores electrical energy in the form of chemical energy between two electrodes with the help of electrolytes, providing the ability to power external circuits.[25] In specific, a typical rechargeable electrochemical cell consists of two electrodes, the anode and the cathode, separated by an electrolyte as shown in **Figure 1-3a**. [25] The first battery was the Volta’s cell (1800) that has alternating discs of zinc and copper separated by cardboard and uses a brine solution as the electrolyte.[3] Later, many forms of battery came out, including widely used lead acid battery and NiMH batteries. Lithium-ion batteries

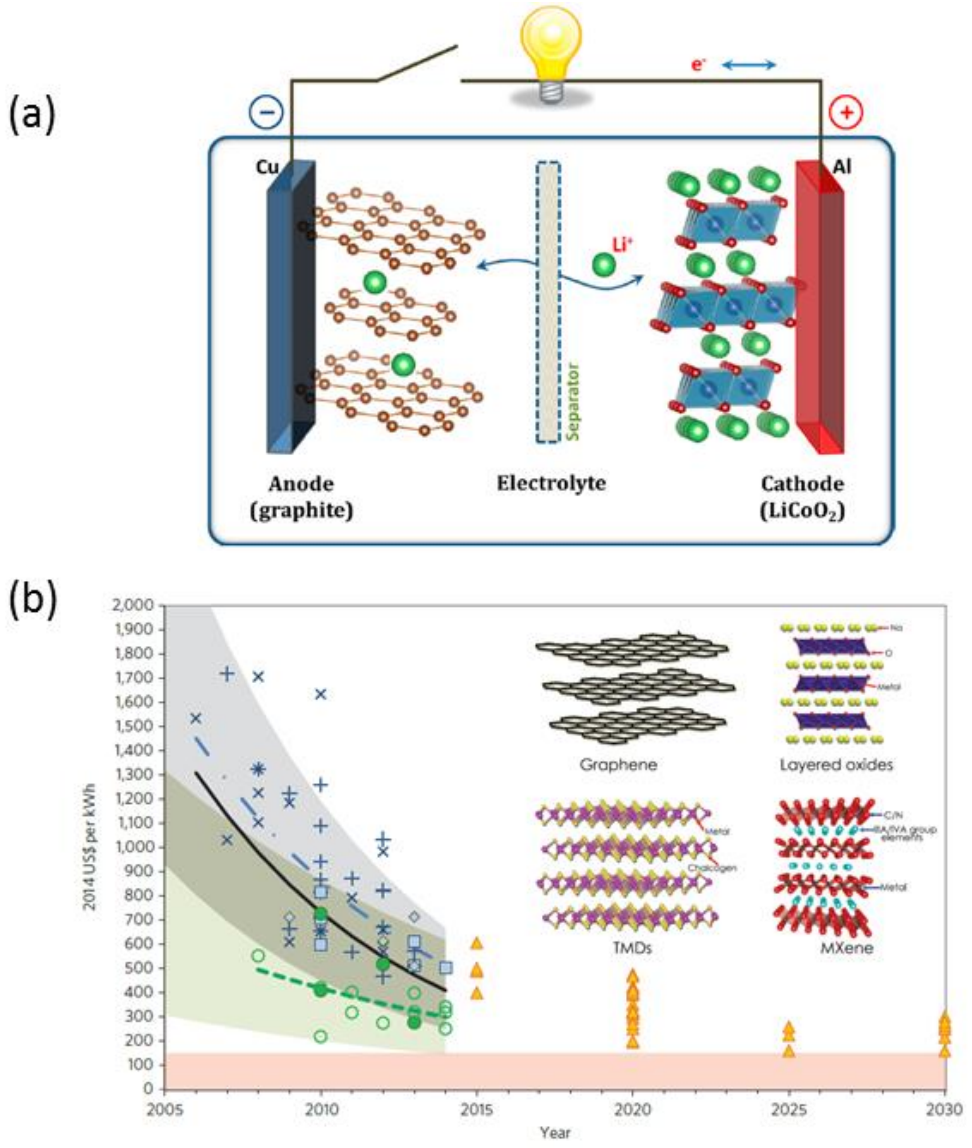

Figure 1-3 Overview of batteries beyond Li. **(a)** Schematic illustration of the first Li-ion battery ($LiCoO_2$/Li electrolyte/graphite). Reprinted from Ref. 25 with permission. **(b)** Cost of batteries from industrial market-leading manufactures. A desired US$150 per kWh is essential for electric vehicles (EV) and grid storage, calling for new 2D materials as shown in inset. Reprint from Ref. 264,265 with permission.

(LIBs) have attracted most attention since their first commercialization by Sony in 1991 (as illustrated in **Figure 1-3a**), because of their high energy density and wide voltage window.[25,26] The emerge of LIBs has enabled the wireless revolution of personal electronics such as cell phones, laptops, digital cameras, and tablets. While the last two decades have seen a remarkable use of LIBs in personal electronics,[27,28] nowadays applications of Li-ion batteries have been extended to the transportation sector,[29–31] owing to the rapid advancement of technology and the urgency to fix our environmental issues partly caused by combustion vehicles.[32,33] Meanwhile stationary applications of batteries are a new trend in integrating sustainable energy onto the current grid.

Challenges remain for current LIBs. First, the performance of current batteries should be improved. Since current set-up of LIBs operate close to their material theoretical limit, it is urgent to find a new family of materials or a new means to tune current materials with low cost, enhanced capacity, power density, cyclability, high-rate performances, etc. Therefore, better electrodes, which are the current bottleneck in battery development, are needed as shown in **Figure 1-3b**. Second, it goes without saying that the amount of energy stored in Li-ion batteries for new applications such as battery electric vehicles (e.g. ~85 kWh for Tesla Model S batteries) is more than three orders of magnitude higher than the energy required in traditional applications such as portable electronics (e.g. ~5 Wh for iPhone 5 batteries), meaning that the quantity of Li resources needed in new battery applications is significant. This new trend, together with the growing popularity of electric vehicles and the scarcity of raw Li resources for large-scale applications have worsen the case. Consequently, the search for suitable alternative to Li and corresponding proper electrode materials is of great importance. Therefore, in **Chapter 2** to **Chapter 3** we show possible solutions using 2D materials beyond current LIBs.

1.1.2 2D materials for Hydrogen evolution reactions

Hydrogen is an important form of renewable energy resource as the global population and fossil fuel consumption continue to rise.[34–37] Its combustion produces only water, during which a very high energy density can be utilized without undesired byproducts of burning traditional fossil fuels. Such a clean and efficient energy source can lessen our dependence on fossil fuels and reduce carbon dioxide emissions to ensure a stable global environment. Using the electrolysis of water to generate hydrogen is not a new idea. In 1895, a Danish scientist Poul la Cour utilized wind power to electrolyze water into hydrogen and stored them as a form of chemical energy.[14] However, until recent the large-scale production of hydrogen is enabled by the development of catalysts. Today, hydrogen is primarily produced by reforming the methane in natural gas, where CO_2 is produced as a byproduct. Harvesting hydrogen under the *principles of green chemistry* is highly desired. Therefore, water splitting is the most desired, which has the highest atom economy, less hazardous chemical involved, and high efficiency. In order to maximize the hydrogen revolution reaction (HER), electrocatalysts are typically applied to facilitate the reaction by changing the reaction pathways and lowering the overpotentials from the reactants to final products, and eventually increase the intrinsic kinetic rate.[37]

Noble metals such as platinum (Pt) or its alloys are commonly used today as catalysts.[22,38–40] They provide the highest exchange current density near the zero overpotential, and hence result in the highest turnover frequency (TOF), which describes how many molecules are generated per second per active site. Other novel metal catalysts, such as ruthenium (Ru) and Palladium (Pd), have relatively good HER performance but seldom have been applied in industry due to their high cost and scarcity. In this context, it is pivotal to find a low-cost and earth-abundant catalyst that can achieve a HER performance comparable to that of Pt.[11–14] In the past decades, significant efforts have been made in searching for such catalysts in various materials systems including metal alloys, chalcogenides, nitrides, phosphides, borides, and carbides.[6–14]

Among these catalysts, 2D TMD system has been extensively studied as a promising alternative HER catalyst due to its unique open morphology that never requires 3D diffusion of the H atoms to the reactive sites, and its preferred chemical and electronic properties.[6,7,21–23] Moreover, changes in band structures due to the 2D nature have been identified as the origin of enhanced HER significantly. The edges of 2H-phase MoS_2 have been demonstrated to be active catalytic sites.[23,38] However, a large portion of the MoS_2 monolayer is consisted of inactive basal plane sites, and one main task is to activate their HER catalytic activity. Further discussions of utilizing, modifying, and tailoring this material system will be discussed in this thesis.

To better understand the HER, we first examine the water-splitting reaction:

$$\mathrm{H_2O} \rightarrow H_2 + \frac{1}{2} O_2 \tag{1-1}$$

where the ΔG is 237.1 kJ/mol or equivalently 1.23 V at the standard condition.[41] This reaction can be further divided into two half reactions: the water oxidation reaction and the water reduction reaction.

Cathode: $$2H^{+} + 2e^{-} \rightarrow H_2 \tag{1-2}$$

Anode: $$H_2O \rightarrow 2H^{+} + \frac{1}{2}O_2 + 2e^{-} \tag{1-3}$$

Above equations described the most common HER half reactions in acidic conditions, in which we are interested. We are interested in the mechanism of this HER reaction in acidic environment as shown in **Figure 1-4a**. There are typically three steps for the hydrogen production. The first one is called the Volmer process, which is the rate limiting step.

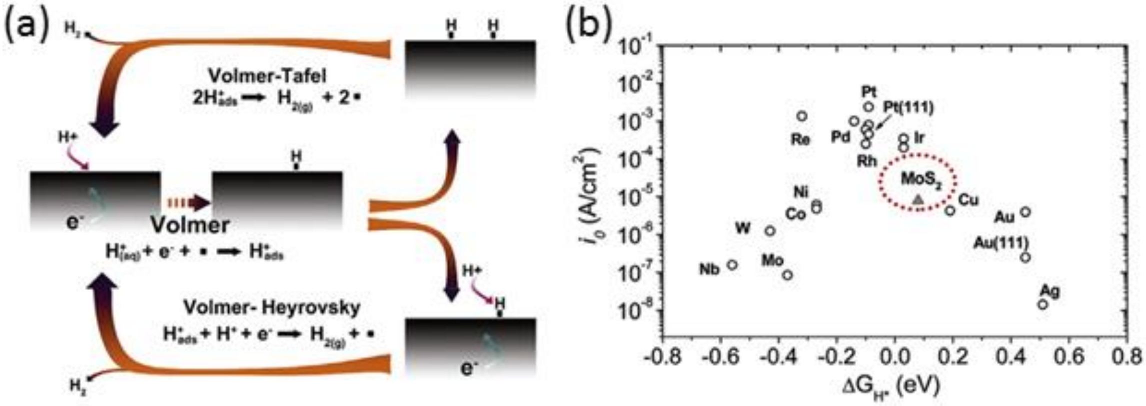

Figure 1-4 Mechanisms and activity trend of HER catalysis **(a)** The mechanisms of HER on the surface of an electrode in acidic solutions. **(b)** The "Volcano" plot for HER catalysts shows the exchange current densities plotted against the free energy of hydrogen adsorption. Materials at the peak of the volcano curve are preferred for HER. Reprint from Ref 37,38 with permission.

$$\mathrm{H}^{+} + e^{-} + * \rightarrow H_{ads}^{*} \tag{1-4}$$

This is the hydrogen (proton) adsorption process facilitated by surface adsorption sites (*) and electrons. The adsorbed hydrogen atom (H_{ads}^{*}) can then participate in either the Tafel reaction or the Heyrovsky reaction. The first one involves the generation of hydrogen gas by combining two adsorbed hydrogen atoms.

$$2H_{ads}^{*} \rightarrow H_2(g) + 2\,* \qquad (1\text{-}5)$$

While the Heyrovsky reaction involves another electron and another proton.

$$H_{ads}^{*} + e^{-} + \mathrm{H}^{+} \rightarrow H_2(g) + * \qquad (1\text{-}6)$$

Given the fact that the Volmer process is the rate-limiting one, catalysts aiming to improve the Volmer adsorption process are highly needed. Because the near-zero Gibbs free energy (~ 0eV) of adsorbed atomic hydrogen corresponds to the ideal efficiency, where hydrogen is bonded neither too strongly ($\Delta G_H < 0$) to detach from the catalyst surface, nor too weakly ($\Delta G_H > 0$) to participate in subsequent reactions, we can take the adsorption energy of atomic hydrogen on the homogeneous catalyst surface as a descriptor. Therefore, it is an important task to theoretically predict and evaluate the HER performance of 2D materials in the line of efforts searching for high-performance HER catalysts. According to the Sabatier plot or the "volcano" curve, which is the guidance criteria for catalysts in HER as shown in **Figure 1-4b**, we are looking for the one that can provide the highest exchange current between H atom and the catalysts while maintaining a low overpotential. Our task is then to improve the performance of 2D catalysts to the *peak* of the volcano curve. In **Chapter 4** and **Chapter 5** we show a way to tune the HER catalytic activity in TMD catalysts.

1.1.3 Modeling 2D materials is necessary but not easy

Although great breakthroughs in 2D materials have been made and several 2D materials have been synthesized and identified as promising candidates for various energy applications, the search is still ongoing. Unlike the ease of peeling graphene from graphite using the "Scotch tape method", many 2D materials are difficult to make. Neither the isolation of individual 2D monolayers from 3D counterparts nor building 2D materials from the bottom using techniques such as chemical vapor deposition (CVD) or physical epitaxy growth is experimentally easy.[42–45] Moreover, the prediction of novel 2D materials, especially those are not easy to realize experimentally so far, should accelerate the speed of scientific discovery and technological achievement of 2D material-based energy applications. Therefore, computational approaches in understanding the mechanisms in energy storage and conversion might further shed light on tuning the properties of current material systems.

A state-of-the-art density functional theory (DFT) is capable to accurately and efficiently compute materials properties such as the energetics, formation energy, band gap, and thermal properties. This theory has been dramatically developed since its first publication in 1965 by Kohn and Sham, approximating the many-electron system into an effective single-electron system. [46,47] Later developed potentials, functionals, and computer codes make it possible to accurately predict the thermodynamics, mechanical properties, electronic properties of various bulk materials. [For details see **Appendix 1**] DFT can provide fast and accurate results in developing new materials, in which it is widely used for quantitative understanding of the microscopic properties that control macroscopic phenomena. For example, DFT calculations of voltage and diffusion kinetics have been widely applied in the design and optimization of lithium ion batteries (LIBs), demonstrating the impact of first-principles in material design.[48] Another example is the rational and computational design of solid catalysts with deep understanding of surface chemical reactions and catalytic activity.[49] One drawback is that DFT requires huge computational power; therefore, the largest scale it can capture is less than ~100 nm or equivalently hundreds of atoms. There are other simulation methods such as molecular dynamics (MD) and Monte Carlo (MC), which can deal with larger length scale but suffer from the problem of empirical parameters/potentials. Also in 2D materials, the length scales of in-plane (up to ~μm) and out-of-plane (Å to nm) differ so dramatically that a multiscale method should be developed to capture such mesoscale phenomena. Therefore, we developed a multiscale method in **Chapter 6-Chapter 8** using DFT informed parameters and macroscopic or mesoscopic methods such as continuum mechanics and finite element methods (FEM), aiming to gain a deeper understanding of 2D materials.

1.2 The goals of this thesis

The main goal of this thesis is to examine the possibility of using 2D materials in improving current energy applications, in particular, battery electrodes and HER catalysts, and to elucidate the mechanisms and conclude guiding principles in tuning 2D materials using combinatorial simulation techniques from different length scales. Typical and promising 2D material systems, including graphene-like materials, MXenes, TMDs, layered covalent-organic framework (COF), and oxides are studied. A general framework of DFT-informed multiscale method will be introduced with several examples in the scope of the mechano-electro-chemical coupling behavior of materials. Moreover, by comparing theoretical results and experimental data, we validate our method and hence make predictions in tailoring the mechanical, electronical, and chemical properties of 2D materials. This thesis focuses on three sections:

1.2.1 2D materials as promising electrodes beyond LIBs

In this section, we show promising 2D material solutions as non-LIB electrodes that can possibly host many metal ions. The recently discovered family of 2D MXenes is discussed and its application is presented. MXenes can possibly host Li, Na, K, Ca ions. In **Chapter 2**, the promise of a representative Ti_3C_2 MXene will be discussed. The predicted capacities of these ions are calculated. Moreover, we attribute the promising capacity to the structural and electronic properties. Further, a novel method in synthesizing nitride MXenes is presented, greatly expanding the current MXene library. The bare and terminated nitride MXene's structure stability, electronic and magnetic properties will be discussed.

Another promising solution lies in the modification of previous non-capable graphene and carbonous 2D networks. We will show in **Chapter 3** that defective graphene and graphene allotropes provide a promising solution in Mg ion batteries. We will further introduce a guiding principle in tuning graphene-like materials for electrode applications.

1.2.2 Tuning the HER catalytic activity of 2D TMDs

In this section, we present a new TMD family of 2D materials as an alternative to the current HER catalysts. First, in **Chapter 4** we shall see that the previous-believed non-reactive 2H basal plane of MoS_2 monolayers can be activated by improving the electrical coupling between the substrate and the catalyst. Moreover, we identified the efficient charge injection and the presence of naturally occurring vacancies are responsible to the observed increase in catalytic activity of the 2H basal plane.

In parallel, in **Chapter 5** we show that the inherent structural asymmetry in the recently synthesized family of Janus TMDs as a new means to stimulate HER activity. We identify the WSSe system as a promising candidate, where the basal plane can be activated without large applied tensile strains and in the absence of significant density of vacancies. Moreover, we attribute the origin of enhanced HER catalytic activity to the introduction of in-gap states and a shift in the Fermi level in hydrogen adsorbed systems due to Janus asymmetry.

1.2.3 Understanding 2D material properties using multiscale simulations

In this section, the general method of DFT-informed multiscale modeling will be discussed in **Chapter 6** followed by a validating example of the Moiré pattern. With this multiscale modeling method, we investigate on modifying the physical, mechanical, and chemical properties of material systems.

Chapter 7 presents a theoretical study to understand the carrier mobility and photoconductivity on the structural and stacking sequence using DFT simulations. This model successfully revealed that the conduction along the vertical direction is achieved by electron hopping between adjacent layers along the vertical pathways. This model not only explains conductivity enhancement mechanisms in COFs, but also provides guidelines in designing highly conductive 2D polymer optoelectronic devices.

Chapter 8 shows a multiscale model to determine the chemical expansion in non-stoichiometric oxides. An elastic dipole tensor that describes the long-range elastic fields created upon formation of oxygen vacancies has been introduced to bridge different length scales. Our work provides an efficient way in computing chemo-mechanical coupling in oxides by introducing the elastic dipoles.

Finally for the completeness of this thesis, some additional theoretical and experimental details will be provided in the **Appendix**

Chapter 2 MXenes as a high capacity electrode material for metal ion batteries

Reprinted (adapted) with permission from **D. Er**, J. Li, M. Naguib, Y. Gogosti, and V. B. Shenoy. *Ti_3C_2 MXene as a High Capacity Electrode Material for Metal (Li, Na, K, Ca)-ion Batteries*. **ACS Applied Materials & Interfaces**, 6(14): 11173-11179 June 2014, and

P. Urbankowski, B. Anasori, T. Makaryan, **D. Er**, S. Kota, P. Walsh, M. Zhao, V. B. Shenoy, M. W. Barsoum, and Y. Gogotsi. *Synthesis of Two-dimensional Titanium Nitride Ti_4N_3 (MXene)*. **Nanoscale**, 8:11385-11391 May 2016

Synopsis

Two-dimensional (2-D) materials are capable of handling high rates of charge in batteries since metal ions do not need to diffuse in a 3-D lattice structure. However, graphene, which is the most well-studied 2-D material, is known to have no Li capacity. Here, adsorption of Li, as well as Na, K, and Ca, on Ti_3C_2, one representative MXene, is predicted by first-principles density functional calculations. In our study, we observed that these alkali atoms exhibit different adsorption energies depending on the coverage. The adsorption energies of Na, K, and Ca decrease as coverage increases, while Li shows little sensitivity to variance in coverage. This observed relationship between adsorption energies and coverage of alkali ions on Ti_3C_2 can be explained by their effective ionic radii. A larger effective ionic radius increases interaction between alkali atoms, thus lower coverage is obtained. Our calculated capacities for Li, Na, K, and Ca on Ti_3C_2 are 447.8, 351.8, 191.8, and 319.8 mAh/g, respectively. Compared to materials currently used in high-rate Li and Na ion battery anodes, MXene shows promise in increasing overall battery performance. Moreover, we report the synthesis of the first two-dimensional transition metal nitride,

Ti_4N_3, MXene. Density functional theory calculations of bare, non-terminated Ti_4N_3 and terminated $Ti_4N_3T_x$ were performed to determine the most energetically stable form of this MXene. Bare and functionalized Ti_4N_3 are predicted to be metallic, which is beneficial for battery applications. Bare Ti_4N_3 is expected to show magnetism, which is significantly reduced in the presence of functional groups.

2.1 Introduction

Energy storage systems have powered the world of technology. Their applications vary from portable electronic devices and electric vehicles, to large scale power grid systems that are needed to manage intermittent renewable energy. Among different energy storage systems, batteries have several advantages such as their compact size and their high efficiency.[50,51] More specifically, lithium-ion batteries (LIBs) have attracted most attention since their first commercialization by Sony in 1991, because of their high energy density and wide voltage window. Most current LIBs are mounted on personal portable electronic devices, entertainment devices, and electric vehicles (EVs). Besides these applications, energy storage in large scale plays an increasing important role in high-tech manufacturing where it is essential to maintain uninterrupted power supply. Large-scale backup devices that smooth the daily power fluctuations are usually deployed in high-tech high-cost semiconductor industry such as chip fabs. Moreover, renewed attentions have been drawn to electrifying the transportation sector, especially after the success of EVs such as Tesla. Massive transportation and tucks that require higher amount of energy storage and power density call for next-generation batteries. With dramatically increasing demands on LIBs, concerns such as Li rarity and uneven distribution of global Li reserves, high cost, potential safety issue and insufficient energy density have to be answered. Unsurprisingly, the current growth rate of LIB use in electric vehicles and grid-level storage systems poses huge problem on Li scarcity. Also Li-ion plating is problematic with dendrites formation that can short the cell and lead to fires. More importantly, the currently used materials in LIBs operate close to their theoretical limit.[4] Therefore, it is pivotal to develop rechargeable batteries beyond LIBs with higher energy density and lower cost especially for EVs and stationary applications.

A possible solution for overcoming the aforementioned problems would be the non-lithium batteries based on alternative metal ions, such as alkali metals (Na^+ and K^+), alkaline earth metals (Mg^{2+} and Ca^{2+}), and group IIIA metal (Al^{3+}). Multivalent ions, such as aluminum, magnesium, and calcium may offer higher energy density than monovalent Li, if two or three electrons can transfer per ion. At the same time, non-Li ions have the advantages of high abundance and low price. For example, Na-ion batteries (NIBs) can be a good candidate to replace LIBs in the future because of its abundance and low cost.[52,53] In addition to NIBs, other alkaline ions such as potassium have been found promising.[54] Moreover, non-lithium metal ions do not form dendrites to the same degree as Li and are less problematic in air and moisture exposure. However, in most of the unconventional metal ion batteries described above, more improvements are still needed in order for them to get to real world applications. Most of the challenging questions involve in the optimum electrolyte for each system and finding hosting materials to work as electrodes. For example, Graphite, which is a successful anode material for LIBs, cannot be used in NIBs, because the Na-C interaction is found to be too weak to contribute to the necessary

Coulomb interactions.[55] Finally the main challenge remains in the lack of suitable electrodes that can host multivalent metal ions and enable fast diffuse and kinetics.

2D materials are of special interest as host materials for metal ion batteries, due to their unique leaf-like structures and superior properties including small weight and large surface-to-mass ratio, which enables fast ion diffusion and offers more ion insertion channels with the whole surface exposed. 2D materials provide stability, high active surface area, and open shortened path for ion insertion/deinsertion. There have been many research efforts on utilizing various forms including single-, few-, and many-layer 2D materials for battery electrodes. For example, modifications to pristine graphene structures have been shown as a possible means to enhance the capacity in LIBs.[56]

Recently, a new family of 2-D early transition metal carbides and carbonitrides, so-called “MXenes”, was synthesized by selective etching of A atoms from MAX phases with hydrofluoric acid (HF) at room temperature.[57,58] The MAX phase is a large family (+70 phases) of ternary metal carbides with composition of $M_{n+1}AX_n$, where M is an early transition metal, A is one of the group A elements, X is carbon and/or nitrogen, and n can be 1, 2, or 3.[59] The M-X bond in MAX phases has a mixed covalent/metallic/ionic character, whereas the M-A bond is metallic,[60] therefore the bonds between the MAX layers cannot be broken mechanically. Since M-A bonds are weaker than M-X bonds, selective loss of the A element can be achieved by etching the MAX phase with an aqueous solution containing fluoride ions, such as aqueous hydrofluoric acid (HF), [57,58] a mixture of lithium fluoride and hydrochloric acid,[61] or with ammonium bifluoride,[62] yielding

MXenes. To date, the following MXenes[63] (**Figure 2-1**) have been synthesized experimentally: Ti_3C_2,[58] Ti_2C, $(Ti_{0.5}Nb_{0.5})_2C$, Ta_4C_3, $(V_{0.5}Cr_{0.5})_3C_2$, Ti_3CN,[57] V_2C, Nb_2C, V_2C, Mo_2C, $(Mo_2Ti)C_3$, Zr_3C_2.[64,65] Since their discovery, MXenes have attracted great attention and have displayed interesting properties. For example, the conductivity of multilayered MXenes was found comparable to that of multilayered graphene.[57] Theoretical studies regarding different properties also began soon after the experimental discovery of MXene systems. Shein and Ivanovskii[66,67] have studied the structural features and relative stabilities of the MXene $Ti_{n+1}C_n$ and $Ti_{n+1}N_n$ (n = 1,2,3). Density functional theory (DFT) calculations showed that some MXenes are semiconductors with tunable band gap that can be controlled by changing the surface termination,[58,68] but nonterminated MXenes are metallic and are expected to have the highest conductivity.[69] Kurtoglu et al.[70] have estimated the in-plane elastic constants of MXenes, using DFT, to be more than 500 GPa, which means that MXenes are expected to have higher stiffness than structural steel (400 GPa).

MXenes have been found to be promising electrode materials for LIBs[71,72] and lithium ion capacitors.[73] Although the capacity of MXenes for Li is close to that of commercial graphite electrodes in LIBs (372 mAh/g), MXenes have shown an excellent capability to handle high cycling rates. For example, at a cycling rate of 36 C, a reversible capacity of 110 mAh/g was obtained for additive-free terminated Ti_3C_2.[72] Note that graphite cannot handle such high cycling rates. This may be attributed to the smaller diffusion barrier for Li atoms on Ti_3C_2. Using DFT calculations, Shen et al.[74] found that the diffusion barrier of Li atoms on Ti_3C_2 (0.07 eV) is smaller than that in anatase TiO_2 (0.35−0.65 eV) and graphite. However, studies of electronic properties and applications of MXenes are needed to utilize other metal ions in batteries. In this chapter, we choose Ti_3C_2 as the representative and best studied MXene and report on its performance as an electrode material for different metals (Li, Na, K, and Ca) ion batteries using first-principles DFT calculations.

Moreover, nitride MXenes have several potential advantages over carbide MXenes. Transition metal nitrides are known to have a higher electronic conductivity than carbides, and the TiN is known as a promising plasmonic material.[75] Based on computational results, it has been predicted that Ti_4N_3 with O, F, or OH functional groups on its surfaces has a higher density of states at the Fermi level, $N(E_F)$, than either Ti_4C_3 or Ti_3C_2 with the same terminations.[69] Furthermore, $N(E_F)$ increases with increasing n in $Ti_{n+1}X_n$ for carbides and nitrides covered by functional groups.[69] Increased electron count due to the presence of N atoms may outweigh the withdrawal of electrons by surface groups, thereby preserving a nitride MXene's metallic character independent of the surface termination.[76] Although treatment in aqueous acidic solutions has been used as a common procedure for producing carbide and carbonitride MXenes, this method failed so far to etch out the layers of Al atoms and produce nitride MXene.[76,77] The difficulty in producing nitride MXenes may be caused by two factors. Calculated cohesive energies of $Ti_{n+1}N_n$ are less than those of $Ti_{n+1}C_n$, whereas the formation energies of $Ti_{n+1}N_n$ from $Ti_{n+1}AlN_n$ are higher than those of $Ti_{n+1}C_n$ from $Ti_{n+1}AlC_n$.[67] Lower cohesion energy implies lower stability of the structure of $Ti_{n+1}N_n$, whereas the higher formation energy of $Ti_{n+1}N_n$ implies that the Al atoms in $Ti_{n+1}AlN_n$ are more strongly bonded, therefore requiring more energy for their extraction. Another possibility of why nitride MXenes have previously not been produced is that the lower stability of $Ti_{n+1}N_n$ caused it to dissolve in aqueous HF solution, the etchant used to attempt to chemically exfoliate $Ti_{n+1}AlN_n$ to produce $Ti_{n+1}N_n$. Therefore in this chapter, a molten salt method will be reported together with DFT calculations to analyze the stability and the electronic and magnetic properties of this nitride Ti_4N_3 MXene.

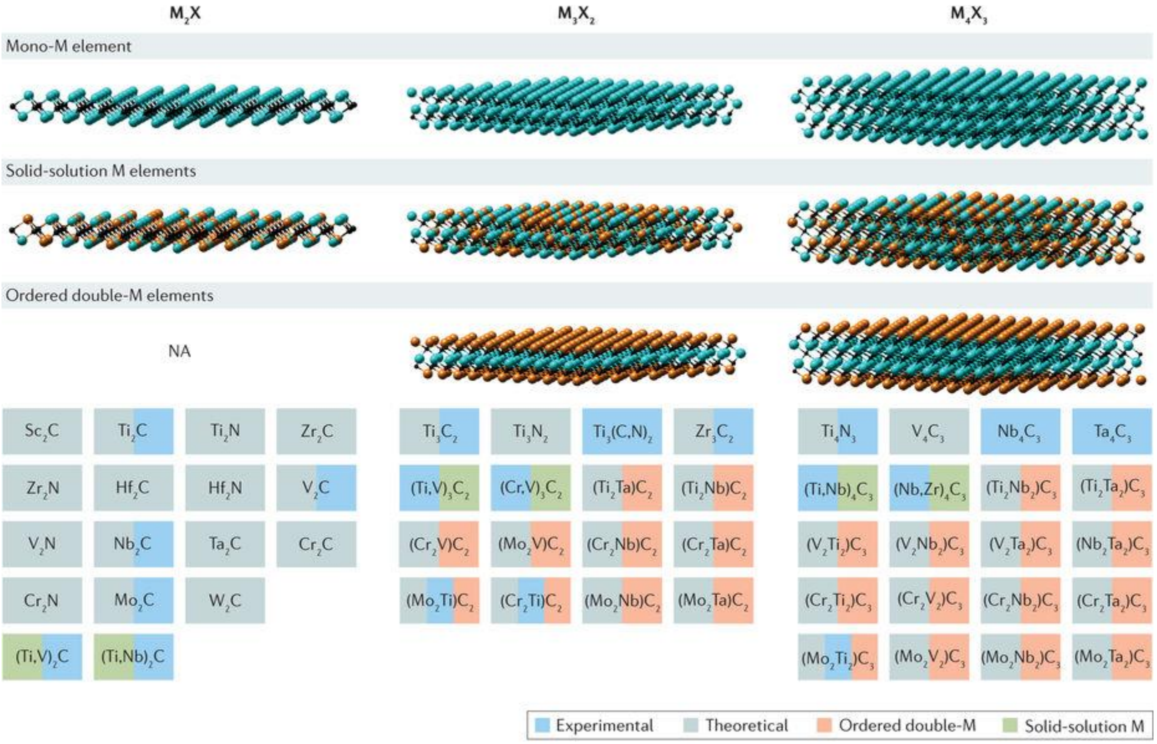

Figure 2-1 MXenes reported so far. Reprinted from Ref 63 with permission.

2.2 **Method**

All our calculations were performed using the Vienna ab initio simulation package (VASP)[78] with the projector augmented wave (PAW)[79,80] potentials for core electrons and the Perdew− Burke−Ernzerhof (PBE)[81] form of the generalized gradient approximation (GGA) for exchange and correlation functional. An energy cutoff of 650 eV was used for the plane wave expansion of valence electron wave functions. The Brillouin zone was sampled using a Monkhorst−Pack special k-point mesh of Γ-centered 12 × 12 × 1 for the unit cell of Ti_3C_2.To simulate the adsorption of single Li, Na, K, and Ca, we used a 3 × 3 × 1 supercell, corresponding to the adatom content $x = 1/9$ in $Ti_3C_2M_x$. Higher adatom contents up to $x = 2.0$ were also investigated. To avoid interactions between simulated two-dimensional Ti_3C_2 monolayer sheet and the periodic images, a vacuum space larger than 10 Å was used. All structures were relaxed with all atoms allowed to move until the force on each atom was less than 0.05 eV/Å (0.002 eV/ Å for nitride MXene calculations). In nitride MXene magnetic calculations, a denser *k*-point mesh of 24×24×1 was employed for the calculation of the spin-polarized partial density of states (PDOS).

To obtain the open circuit voltage (OCV),[82] we considered the reaction

$$\mathrm{Ti_3C_2} + x\mathrm{M} \rightarrow \mathrm{Ti_3C_2M}_x \tag{2-1}$$

where x is the number of adatoms inserted in the unit cell of Ti_3C_2. The electronic potential during this process can be written in the form of Gibbs free energy

$$\mathrm{V} = -\frac{\Delta G_f}{zF} \tag{2-2}$$

where z and F are the number of valence electrons during the adatom process and the Faraday constant, respectively; ΔG_f is the change in Gibbs free energy during the adatom process which is defined as

$$\Delta \mathrm{G_f} = \Delta E_f + P\Delta V_f - T\Delta S_f \tag{2-3}$$

$P\Delta V_f$ is on the order of 10^{-5} eV and the term $T\Delta S_f$ is comparable to 26 meV at room temperature; thus, the entropy and pressure terms are negligible.[82] $\Delta \mathrm{G_f}$ is then approximately equal to the formation energy, ΔE_f, involved in the adsorption process, which is defined as

$$\Delta \mathrm{E_f} = E_{Ti_3C_2M_x} - (xE_M + E_{Ti_3C_2}) \tag{2-4}$$

where $E_{Ti_3C_2M_x}$ is the total energy of the composite system with x metal atoms adsorbed in the unit cell of Ti_3C_2, E_M is the total energy of a single Li, Na, or K atom in a bulk BCC structure or Ca in a bulk FCC structure, and $E_{Ti_3C_2}$ is the total energy of an isolated Ti_3C_2. The OCV is related to the formation energy by

$$\mathrm{OCV} = -\frac{\Delta G_f}{x} \approx -\frac{\Delta E_f}{x} \tag{2-5}$$

2.3 **Results**

2.3.1 Structure Models

By removing the Al atom from bulk Ti_3AlC_2, monolayer Ti_3C_2 is constructed with quintuple layers stacked in a sequence of Ti(s)−C−Ti(c)−C−Ti(s), where Ti(s) corresponds to the surface Ti atoms and Ti(c) corresponds to the center Ti atoms in Ti_3C_2. The relaxed structure was found to have a lattice constant a = 3.1005 Å, which is in good agreement with the experimental value 3.057 Å.[72] The structure can also be described as trilayer Ti-atomic layers being interleaved with two C atomic layers forming an edge-shared TiC_6 octahedral structure as shown in **Figure 2-2**. The unit cell of Ti_3C_2 is highlighted in a 3 × 3 × 1 supercell. Here we only consider the adsorption on the surface of Ti_3C_2 MXene. It is easy to recognize the high symmetry adatom sites A, B, and C as indicated in Figure 1 on the surface: The A site is at the center of a hexagon composed of carbon atoms, the B site is directly above the carbon atom, and the C site is directly above the Ti atom. Compared to the surface adsorption, the insertion of metal ions into the inner interstitial site is energetically less favorable. We have performed calculations of bulk interstitial adsorption for Li, Na, K, and Ca. The adsorption energies are 4.40, 12.23, 15.39, and 12.21 eV, respectively. The disruption of structure integrity was also observed.

2.3.2 Adatom Adsorption

The binding of metal ions on Ti_3C_2 was studied by calculating the adsorption energy E_{ad} using larger super cell with x = 1/9 in $Ti_3C_2M_x$. Because $E_{ad} = -OCV$, the large positive OCV indicates energetically favorable adsorption. In **Table 2-1**, we list the calculated OCVs for Li, Na, K, and Ca adatoms on A, B, and C sites. For all atoms, the OCV of A is close to that of B whereas that of C is lower. A- and B- site OCVs are higher than that of the C site by about 100 meV. The OCV of each site increases with the alkali atom mass, suggesting stronger adsorption for heavier alkali elements. However, this tread does not apply for Ca due to its different valence ([Ar]4s2) electron configuration. In the following discussions, we focus on the adsorption of A and B sites sine the C sites are less energetically favored.

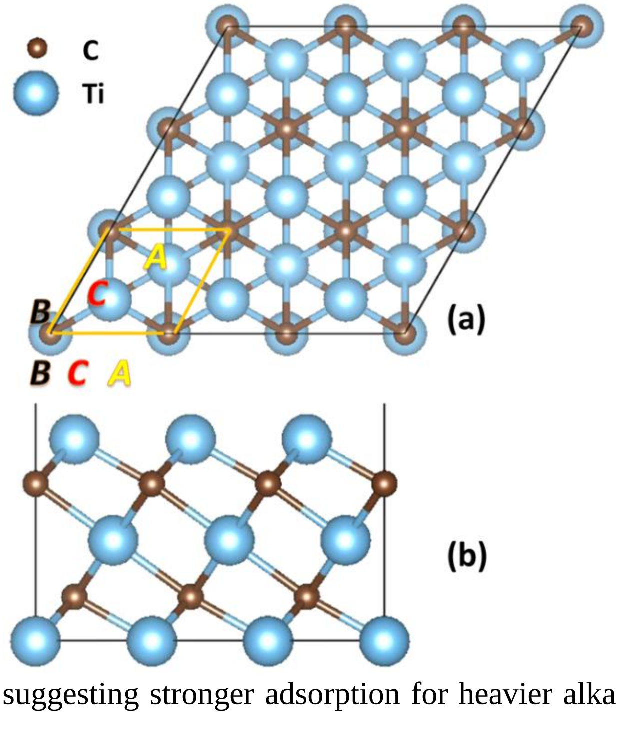

Figure 2-2 Schematic diagram showing the crystal structure of a Ti_3C_2 monolayer with **(a)** top and **(b)** side view. The large blue balls represent Ti atoms and small brown balls represent C atoms. The highlighted unit cell indicates the high symmetry A, B, and C adatom sites.

Table 2-1 Energetic and Structural Properties of Li, Na, K, and Ca Adatoms on Ti_3C_2 Monolayer. OCV, Bader charge (q), and adatom height (h) of energetically favorable A, and B sites for Li, Na, K, and Ca on Ti_3C_2.

	OCV (eV)			q (e^-)		h(Å)	
	A	B	C	A	B	A	B
Li	0.43	0.30	0.43	0.21	0.19	2.51	2.50
Na	0.74	0.72	0.74	0.40	0.38	2.84	2.82
K	1.90	1.81	1.90	0.47	0.36	3.27	3.25
Ca	1.43	1.33	1.42	1.31	1.24	2.72	2.70

In addition to the OCVs, the adsorption strength of adatoms on different sites is also reflected in the adatom height h which is defined as the vertical distance between the adatom and the topmost surface Ti atom. The adatom heights for A and B sites are listed in **Table 2-1**. It can be seen that for A and B sites the adatoms have very close height, consistent with the comparable OCVs for these two sites. With the increase of element mass of alkali adatoms, h increases for both sites excluding Ca.

To gain deeper insight into the difference in adsorption for different metal atoms on Ti_3C_2, we performed the electronic structure calculations. **Figure 2-3** depict the computed total density of states (TDOS) and projected density of states (PDOS) for the adsorption of Li, Na, K, and Ca, respectively. There is a significant overlap at 0.70 eV below the Fermi level between the Ti 3d orbital and the Li 2s orbital, indicating s-d hybridization and therefore, strong binding of Li atoms on the Ti_3C_2 surface. Similarly for Na, K, and Ca, the s−d hybridizations are also observed with peaks located at 0.33, 0.285, and 1.23 eV below the Fermi level, respectively.

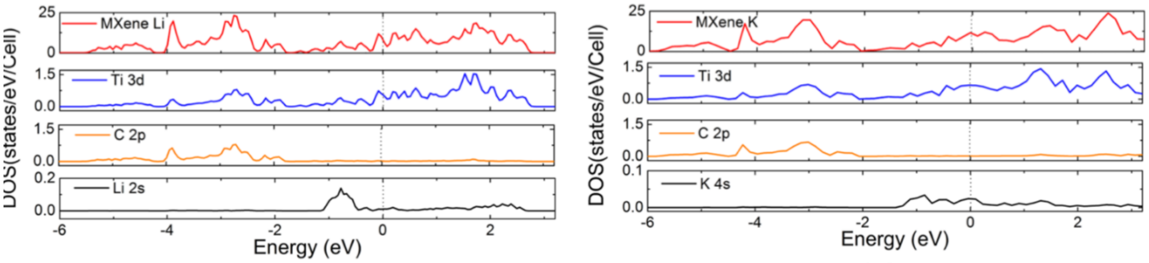

(a) Ti_3C_2+Li

(c) Ti_3C_2+K

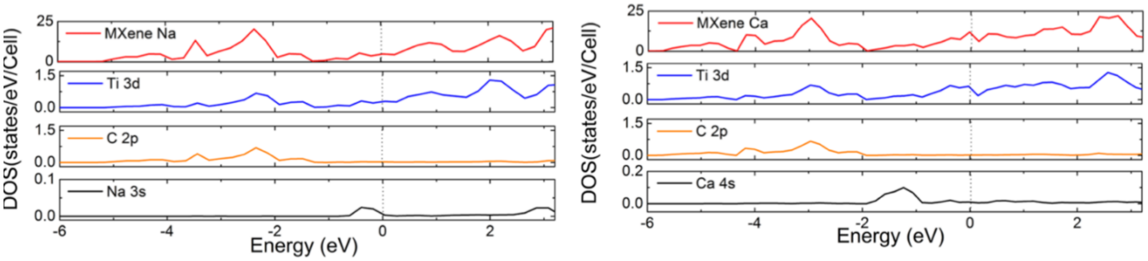

(b) Ti_3C_2+Na

(d) Ti_3C_2+Ca

Figure 2-3 Total DOS and PDOS of Ti 3d, C 2p, and s orbitals of **(a)** Li, **(b)** Na, **(c)** K, and **(d)** Ca for the composite system of $Ti_3C_2M_{1/9}$. The Fermi levels are set to zero and are indicated by the dashed lines.

To visualize the effect of adatom adsorption on the charge distribution, we calculated the bonding charge density which is obtained as the difference between the valence charge density before and after the bonding. **Figure 2-4** shows the bonding charge density in the plane passing through both the adatom and the high symmetry line on the Ti_3C_2 monolayer. Red and blue colors indicate the electron accumulation and depletion, respectively. These bonding charge distributions clearly show the charge transfer from the adatoms to the Ti_3C_2 monolayer. The amount of charge transfer was estimated quantitatively by using Bader charge analysis and the results are presented in **Table 2-1** for Li, Na, K, and Ca at energetically favored A and B sites. The Bader charge analysis is qualitatively consistent with our PDOS calculations. The area covered by the PDOS of valence s-states for Li is about 0.1 electrons, which indicates a charge transfer from Li to Ti_3C_2.

It is well-known that the diffusion barrier is a key factor that determines the rate at which a battery can be charged and discharged. We have investigated the diffusion barriers for Li, Na, K, and Ca in the Ti_3C_2 monolayer using the nudged elastic band (NEB) method[83] as implemented in VASP in order to evaluate the promise of Ti_3C_2 as high-rate electrode materials. The migration pathways are selected along the high symmetry line between energetically favorable adsorption sites on the surface and in **Figure 2-5** we depict the optimized pathways. The calculated diffusion barrier for Li is 0.068 eV, in close comparison to the previously reported value.[74] For Na, K, and Ca, the diffusion barriers are 0.096, 0.103, and 0.118 eV, respectively. Compared to commercial anode materials based

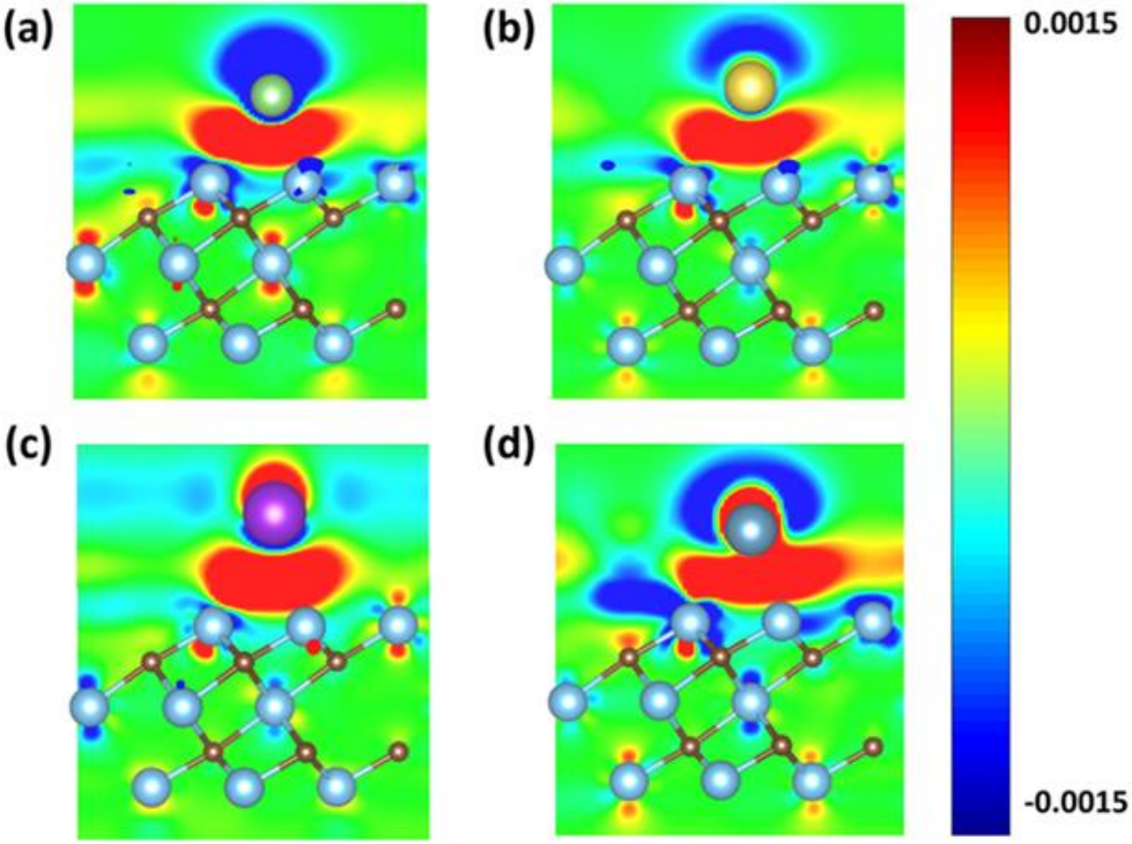

Figure 2-4 Bonding charge density for adatoms **(a)** Li, **(b)** Na, **(c)** K, and **(d)** Ca (being adsorbed at the A site) in $Ti_3C_2M_x$ system obtained as the charge density difference between the valence charge density before and after the bonding. Red and blue colors indicate the electron accumulation and depletion, respectively. The color scale is in the units of e/Bohr^3.

on TiO_2 polymorphs with a diffusion barrier about 0.35−0.65 eV for Li, Ti_3C_2 can exhibit faster transport and higher charge/ discharge rate for Li, and even for other alkali elements. Another commercial anode material, graphite, needs to overcome a diffusion barrier larger than 0.3 eV for Li. This suggests that Ti_3C_2 is a promising candidate for high rate electrode materials.

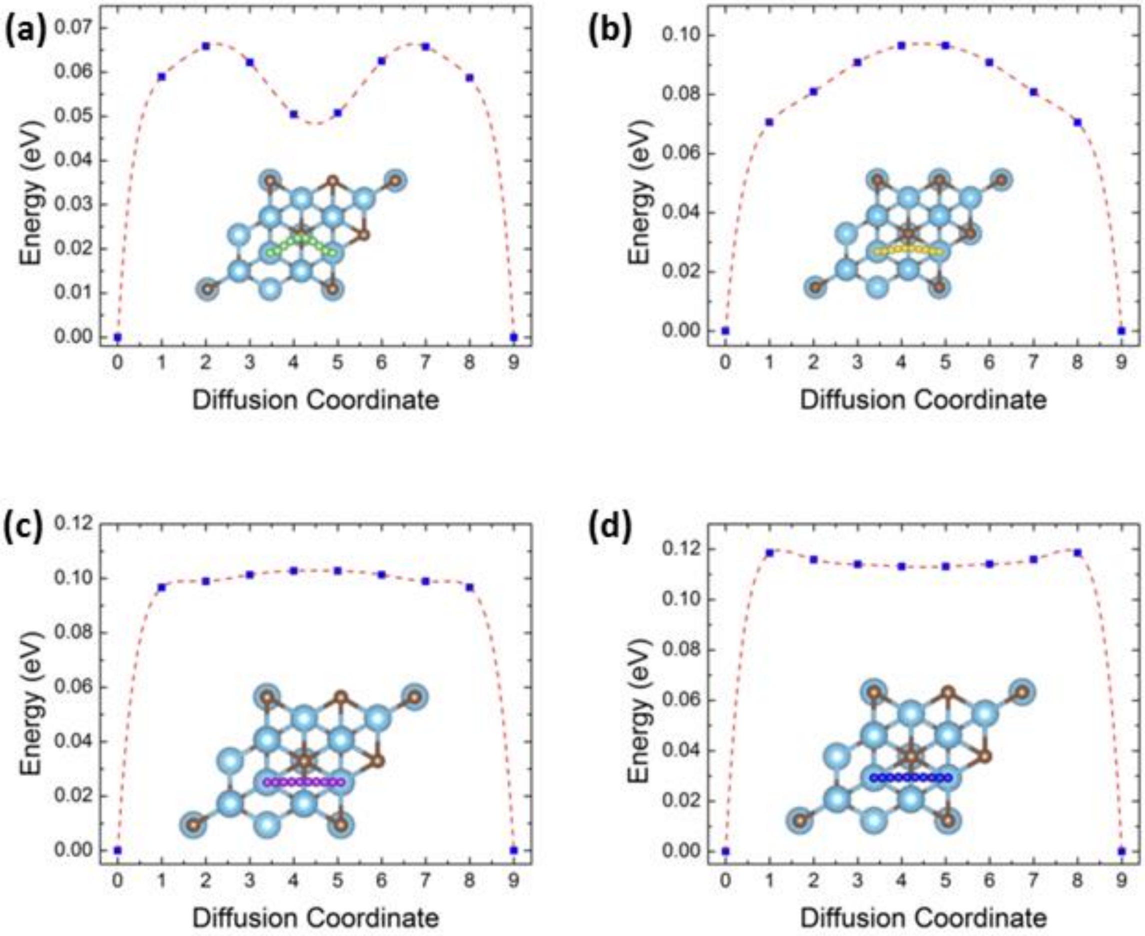

Figure 2-5 Schematic representation of the top view of the energetically optimized migration pathways and the corresponding diffusion barrier profiles of **(a)** Li, **(b)** Na, **(c)** K, and **(d)** Ca on Ti_3C_2 MXene.

2.3.3 Open Circuit Voltage and Theoretical Specific Capacity

In addition to the adsorption of single adatom on the Ti_3C_2 MXene, we also evaluated the OCVs as a function of the adatom concentration by varying x in the $Ti_3C_2M_x$ system. We considered different x in the $Ti_3C_2M_x$ system, namely, 0.11, 0.25, 0.5, 0.75, and 1, by using different supercells with stoichiometry $(Ti_3C_2)_9M$, $(Ti_3C_2)_4M$, $(Ti_3C_2)_2M$, $(Ti_3C_2)_4M_3$ and Ti_3C_2M, respectively. Moreover, in order to determine whether adatoms can occupy other adsorption sites after fully covering the A sites of lowest adsorption energy, we computed

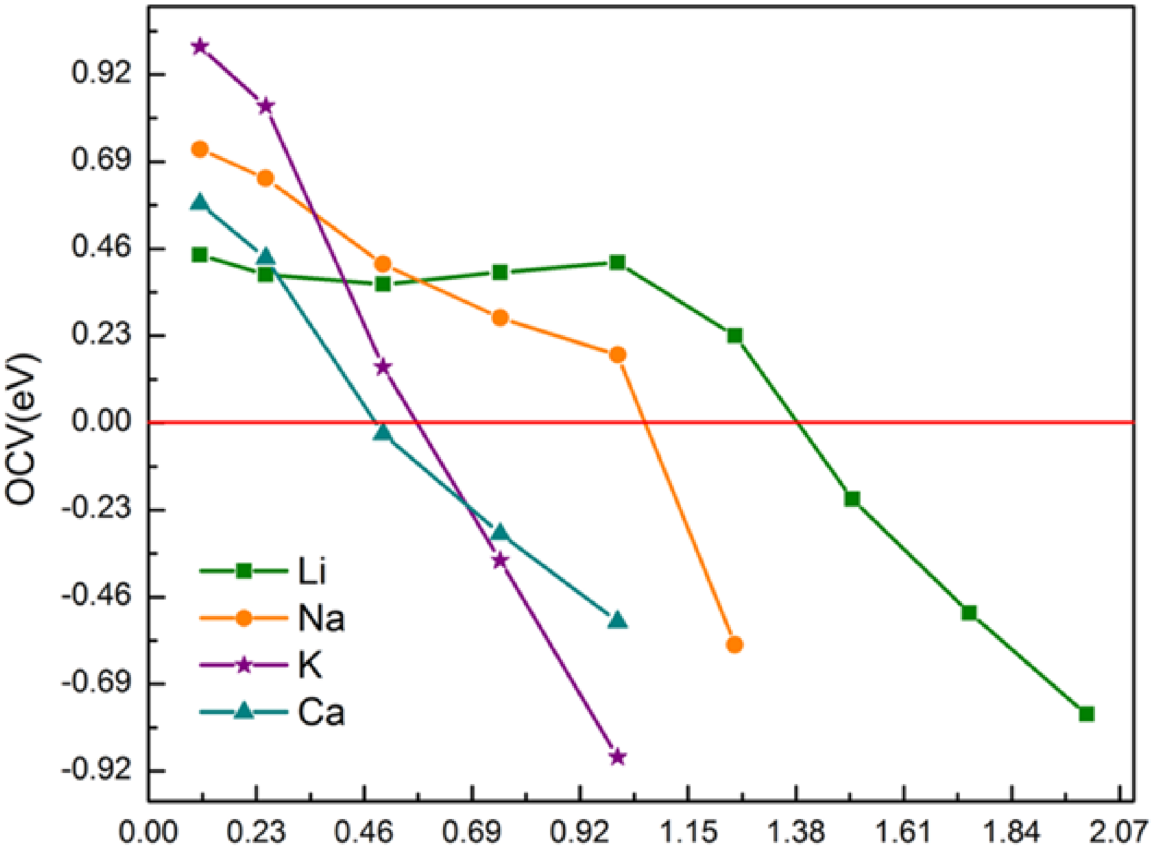

Figure 2-6 OCV changes with adatom content for the single-side adsorption of Li, Na, K, and Ca on the Ti_3C_2 surface. x <1 corresponds to the adatom adsorption on the A site, and x >1 corresponds to partial coverage of B sites and full coverage of A site. The x corresponding to zero OCV is used to estimate the maximum adatom content and capacity.

the possibility of B sites adsorption by varying the number of adatoms in a 2 × 2 × 1 supercell from 1 to 4, corresponding to the adatom content x = 1.25, 1.5, 1.75, and 2.

In **Figure 2-6**, we depict the calculated OCVs as a function of the adatom concentration represented by x in the $Ti_3C_2M_x$ system. Only the highest OCV among different configurations is shown for each concentration. For all alkali elements studied herein except Li, the OCVs decrease with increased adatom concentration, but with different slopes. In **Figure 2-6**, OCVs of Na, K, and Ca decrease as x increases, while Li shows little sensitivity to the variance of x in the range $x \leq 1$. The OCV of Li starts to decrease when $x > 1$. Only A is shown in **Figure 2-6** because the difference of OCVs between the A and B sites is less than 100 meV, which means one specific representation is enough for the trend. At low adatom content ($x < 0.25$), the OCVs of K, Na, Ca, and Li decrease; however, this trend changes at high adatom content ($x > 0.8$). The OCV of Li is now the highest, followed by Na, Ca, and K in that order. Once the OCV is zero, we reach a situation where no more adatoms can be adsorbed, which corresponds to the maximum x in $Ti_3C_2M_x$. Consequently, the capacity of each element on the Ti_3C_2 surface can be determined. For K and Ca, the estimated maximum x is approximately 0.6 and 0.5, respectively, meaning that the OCVs have dropped to zero before fully covering the A site. At x = 1, the OCVs of Li and Na are positive, indicating that additional adatoms can be adsorbed on the Ti_3C_2 surface where the A site is fully covered. For Li and Na, the maximum x is approximately 1.4 and 1.1 by assuming a linear relationship between two adatom contents around zero OCV. This result suggests that the Li and Na adatoms can seek other energetically favorable sites after fully covering the A site.

It is noted that the above discussion is based on the calculation assuming single-side adsorption. The fact that the charge transfer mainly occurs between the surface Ti(s) atoms and the adatom suggest the possibility of adsorption on double sides. In order to verify this, we considered a 2 × 2 × 1 supercell of Ti_3C_2 monolayer with increased adatom content on both surfaces. Our computations reveal that the 2 × 2 × 1 supercell of the Ti_3C_2 monolayer can accommodate up to 8 Li, 8 Na, 4 K, and 4 Ca adatoms, which corresponds to the chemical stoichiometry of $Ti_3C_2Li_2$, $Ti_3C_2Na_2$, Ti_3C_2K, and Ti_3C_2Ca with symmetric configuration of adatoms on both sides. The calculated OCVs are 0.413, 0.137, 0.128, and 0.087 eV, respectively. Therefore, we can estimate the maximum adatom content to be 2.8, 2.2, 1.2, and 1 for Li, Na, K, and Ca, respectively. For single-site adsorption, the maximum capacity CM (mAh/g) can be computed from the maximum adatom content $x_{\max}$ as

$$C_M = \frac{1}{M_{\mathrm{Ti_3C_2}}}\left[x_{\max} \times z \times F \times 10^3\right] \tag{2-6}$$

where z is the valence number (z = 1 for Li, Na, and K; z =2 for Ca), F is the Faraday constant (26.810 Ah/mol), and MTi_3C_2 is the atomic mass of Ti_3C_2 (167.62 g/mol). Based on the assumption of double-side adsorption, the theoretical capacities of Li, Na, K, and Ca on Ti_3C_2 MXene are calculated to be 447.8, 351.8, 191.8, and 319.8 mAh/g, respectively.

2.3.4 Effective Ionic Radius

As shown in **Figure 2-6**, the maximum coverage of adatoms on Ti_3C_2 monolayer vary with the alkali elements of different atomic numbers, which can be attributed to the effective size of the ionized adatom. For a given ion, the ionic radius is strongly dependent on the charge state. Therefore, an effective ionic radius $R^{\Delta q}$ can be defined as $R^{\Delta q} = R^0 + (R^1 - R^0)\,\Delta q$ by assuming a linear dependence on the charge state Δq with R^0 the atomic radius and R^1 the ionic radius of charge state +1. As shown in **Table 2-2** the adsorbed Li, Na, K, and Ca atoms are acting as electron donors and about 0.79, 0.60, 0.53, and 0.69 |e| are transferred from Li, Na, K, and Ca atoms to the Ti_3C_2 monolayer. The corresponding $R^{\Delta q}$ are 0.86, 1.34, 1.81, and 1.63 Å, respectively. The effective ionic radius is closely related to the maximum coverage of the alkali elements. For the full coverage of energetically favorable A sites, the distance between two nearest adatoms is 3.10 Å which indicates a critical radius 1.55 Å for the ionized adatoms. The $R^{\Delta q}$ of Li is much smaller than 1.55 Å, which is consistent with the fact that the OCVs are not sensitive to the coverage as indicated in **Figure 2-6**. For Na, the effective ionic radius is close to 1.55 Å, the coulomb repulsion between ionized adatoms leads to the reduced OCVs when increasing the coverage, but a full coverage of A sites can still be obtained. The fact that $R^{\Delta q}$ of K is greater than 1.55 Å makes the maximum adatom content x ~ 0.6. Although $R^{\Delta q}$ of Ca is smaller than that of K, the maximum x is only 0.5 due to the small OCV for low coverage. We found that for Li, Na, and K a linear relationship between the effective ionic radius and the maximum adatom content x in $Ti_3C_2M_x$ can be established as

$$x_{\max} = -1.68 \times R^{\Delta q} + 4.318 \tag{2-7}$$

in which $x_{\max}$ is calculated by taking into account the double-side adsorption. Care must be exercised that this relationship does not hold for Ca because Ca has two valence electrons which results in stronger interactions with the Ti_3C_2 monolayer. Correspondingly, we can establish a relationship between the capacity and the effective ionic radius by combining Equations (2-6) and (2-7)

$$C_M = \frac{1}{M_{\mathrm{Ti_3C_2}}}\left[(-1.68 \times R^{\Delta q} + 4.318) \times z \times F \times 10^3\right] \tag{2-8}$$

This expression provides a simple description for the theoretical capacity of alkali metals in terms of the effective ionic radius of the ionized adatoms. In **Figure 2-7**, we plot the calculated maximum adatom contents and capacities of $Ti_3C_2M_x$ as a function of effective ionic radius with Li, Na, K, and Ca adsorbed on two sides.

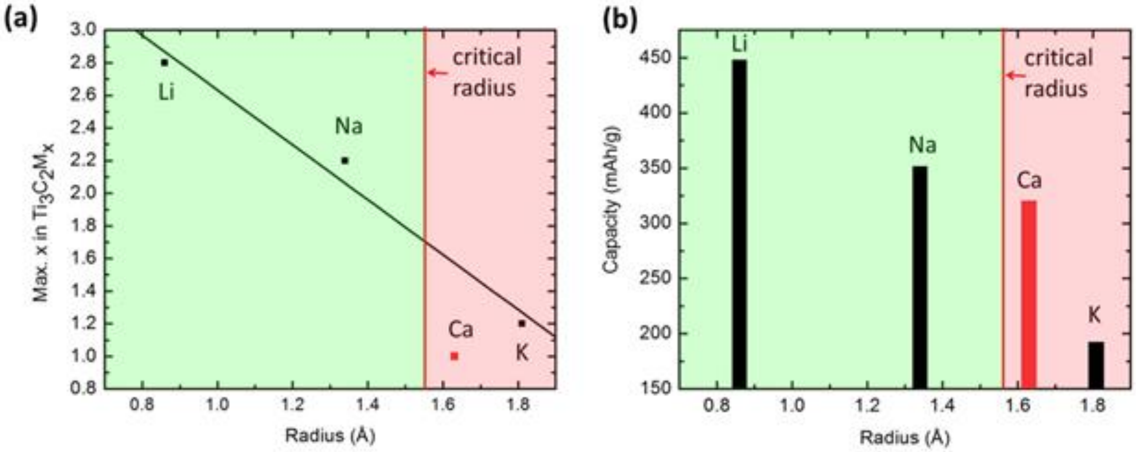

Figure 2-7 Relationship between **(a)** maximum adatom content **(b)** capacity and ionic radius for adsorption on both sides. The maximum adatom content and capacity of Li, Na, and K follow a linear relationship. Ca deviates from the linear expression due to its different valence electron structure.

Table 2-2 Relationship between Charge Transfer (Δq) and Effective Ionic Radius ($R^{\Delta q}$). $R^{\Delta q}$ is a linear interpolation of the atomic radius (R^0) and the ionic radius (R^1)

	R^0 (Å)	R^1 (Å)	Δq (e^-)	$R^{\Delta q}$ (Å)
Li	1.55	0.68 (Li^+)	0.79	0.86
Na	1.90	0.97(Na^+)	0.60	1.34
K	2.35	1.33(K^+)	0.53	1.81
Ca	1.97	0.99(Ca^{2+})	0.69	1.63

2.3.5 Comparison to Graphene

Our predicted high capacity of Ti_3C_2 MXene is in contrast to extensively studied graphene sheets. Although it displays various appealing properties, pristine single layered graphene is not a good candidate for electrode materials in LIBs.[84,85] For comparison, we performed the electronic structure calculations for pristine graphene with Li adatoms using a 2 × 2 × 1 supercell. **Figure 2-8** shows the total DOS of graphene with a Li adatom, and the DOS projected onto C *2p* and Li *2s* orbitals. It can be seen that in the range 0− 16 eV below the Fermi level, the C *2p* orbital contributes most to the energy states. However, no significant peak of the Li *2s* orbital below the Fermi level was observed. The peak of the Li *2s* orbital occurs at 0.815 eV above the Fermi level, where there is an overlap of the peak of the C *2p* orbital and the total DOS. This peak corresponds to an s-p antibonding orbital. Therefore, the lack of overlapped peaks below the Fermi level indicates the absence of hybridization

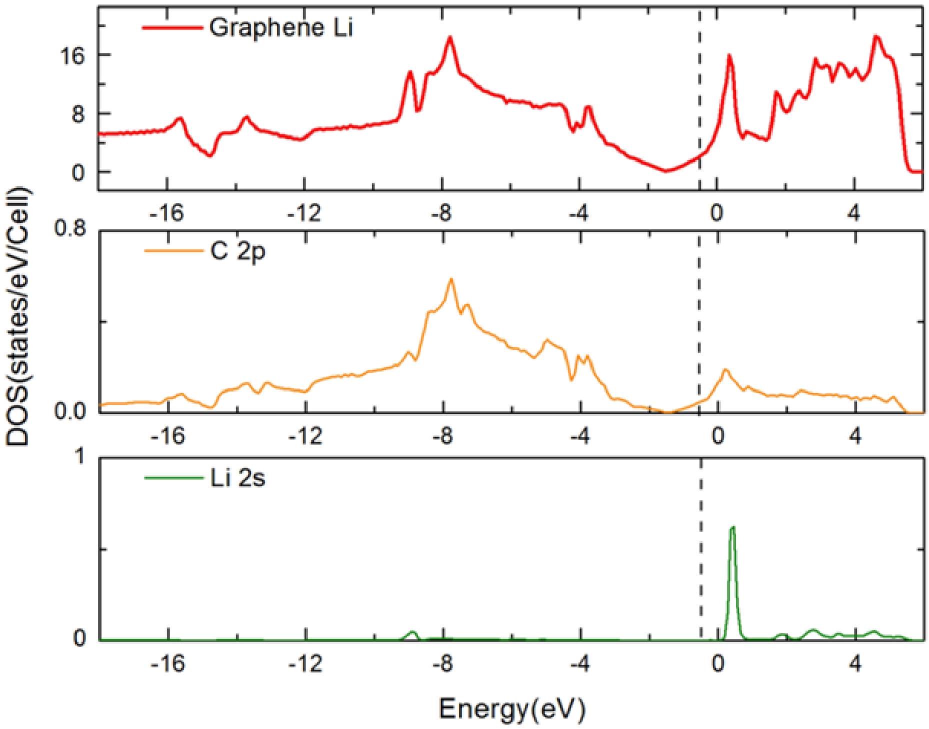

Figure 2-8 Total DOS of the pristine graphene with Li adatom and the PDOS onto C 2p and Li 2s orbitals.

of orbitals and therefore, a weaker bonding. As shown in **Figure 2-3**, an overlap of the Li *2s* orbital with the Ti *3d* orbital in Ti_3C_2 MXene occurs at 0.70 eV below the Fermi level. A significant and broad peak of Li overlaps with several peaks of the Ti *3d* orbital, which indicates the existence of an $s-d$ hybridization during Li adsorption.

2.3.6 Synthesis of Nitride MXenes

The first successful synthesis of nitride MXenes [experimental details can be found in the **Appendix**] using a molten salt method provides another solution besides carbide MXenes. To study the structure and electronic properties of non-terminated Ti_4N_3 and terminated $Ti_4N_3T_x$ (T = F, O, and OH) monolayers, we carried out spin-polarized DFT calculations. Monolayer Ti_4N_3 was constructed from a MAX phase with a calculated lattice parameter a = 2.9915 Å and a thickness of L = 7.44 Å as shown in **Figure 2-9 a**. We first evaluated the relative stability of the fully terminated Ti_4N_3 monolayers with different arrangements of surface terminations (F, O, and OH). Two energetically favorable arrangements of the surface terminations are considered, A and B, shown in **Figure 2-9 b** and **c**. The total energy differences with respect to configuration AA are listed in **Table 2-3**. Our calculations indicate that configuration AA (**Figure 2-9 d**) is the lowest energy for the F and O terminations, whereas for OH, the AB configuration (**Figure 2-9 e**) is more stable.

We then evaluated the formation energies of different surface terminations in order to predict which surface termination is more energetically preferred. In our case:

$$E_{\mathrm{form}}(T) = [E_{tot}(\mathrm{Ti_4N_3T_x}) - E(\mathrm{Ti_4N_3}) - xE(T)]/x \quad (2\text{-}9)$$

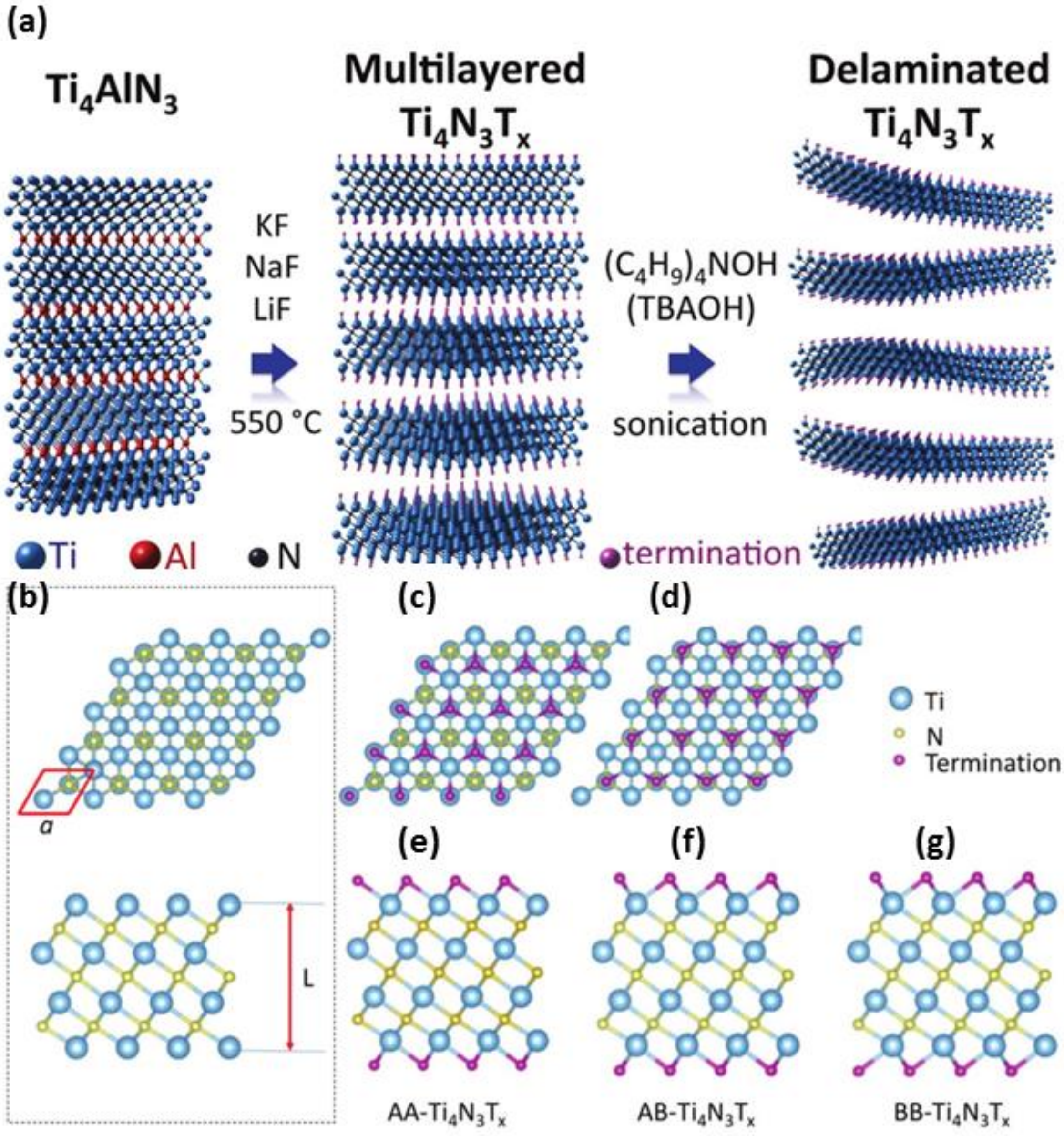

Figure 2-9 (a) Schematic illustration of the synthesis of $Ti_4N_3T_x$ by molten salt treatment of Ti_4AlN_3 at 550 °C under Ar, followed by delamination of the multilayered MXene by TBAOH. **(b)** Crystal structure of Ti_4N_3 monolayers (top and side views). For the single-sided terminations, two energetically favorable arrangements of the surface terminations are considered: **(c)** hollow site of surface Ti denoted by A, and **(d)** atop site of carbon denoted by B. In the case of double-sided terminations, the possible configurations of terminations are **(e)** AA-$Ti_4N_3T_x$, (f) AB-$Ti_4N_3T_x$, and (g) BB-$Ti_4N_3T_x$.

termination group, the total energies of the terminated $Ti_4N_3T_x$ monolayers, non-terminated Ti_4N_3 monolayers, and surface termination groups (–F, –O, and –OH) calculated from VASP, respectively. The formation energies of single-sided and double-sided terminated $Ti_4N_3T_x$ monolayers are listed in **Table 2-3**. Based on these results we conclude that O terminations are energetically preferred compared to F and OH functional groups, while the OH termination is the least favorable one (even compared to F) with an energy difference of more than 0.4 eV per unit cell.

Table 2-3 Relative stability of functionalized $Ti_4N_3T_x$ with different arrangement of surface terminations, where the most stable configuration is in bold font. Formation energies of -F, -O, and -OH surface terminations with single-side and double-side covered $Ti_4N_3T_x$ MXene. Calculated magnetic moment per unit cell for $Ti_4N_3T_x$ MXene.

		Ti_4N_3	**$Ti_4N_3F_x$**	**$Ti_4N_3O_x$**	**$Ti_4N_3(OH)_x$**
$E-E_0$ (eV)		AA	**0.000**	**0.000**	0.000
		AB	0.085	0.5284	**-0.012**
		BB	0.159	1.046	0.010
E_{form} (eV)	Single (Ti_4N_3T)	N/A	-5.804	-7.855	-5.332
	Double ($Ti_4N_3T_2$)	N/A	-5.781	-7.773	-5.347
Magnetic moment per unit cell (μB)		7.00	0.88	0.37	0.00

In order to analyze deeply the electronic properties of $Ti_4N_3T_x$, we calculated the spin-polarized partial density of states (PDOS) of the most stable configurations considering the contribution of different orbitals in **Figure 2-10**. For the $Ti_4N_3T_x$ and Ti_4N_3 monolayers, the main contribution near the Fermi level comes from the Ti 3*d* orbital, while a hybridization between Ti 3*d* orbital and N 2*p* orbital occurs from -2.0 to -8.0 eV below the Fermi level. The calculated total DOS at the Fermi level of bare, -F, -O, and -OH terminated

Ti_4N_3 monolayers are 4.62, 4.0, 3.8, and 1.9, respectively. This result indicates that the Ti_4N_3 monolayer is more metallic while the terminations lower the DOS at the Fermi level, similar to carbide MXenes.[69] On the other hand, the low DOS at the Fermi level of the OH terminated $Ti_4N_3T_x$ monolayer partially explains why OH is not energetically favorable. Note that previous studies[67,69] have only discussed about the non-spin-polarized PDOS of F terminated $Ti_4N_3T_x$ case, while we are reporting a spin-polarized study on all possible terminations in $Ti_4N_3T_x$ (T = F, O, and OH). In **Figure 2-10**, a magnetic moment of 7.00 μB per unit cell was observed in Ti_4N_3, which results mainly from the unoccupied 3*d* orbitals of the Ti atoms. Surface terminations such as OH can dramatically lower the magnetic moment to zero.

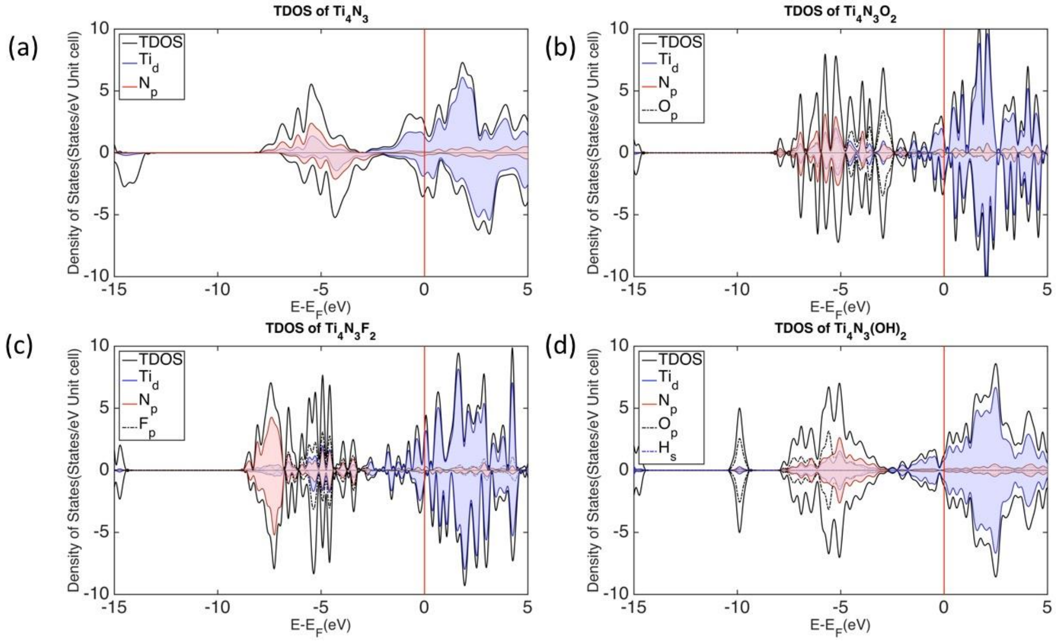

Figure 2-10 Spin-polarized partial density of states of Ti_4N_3 monolayers and surface terminated $Ti_4N_3T_x$. The Fermi levels are set to zero and are indicated by the red line.

2.4 Conclusion

With first-principles density functional method we investigated the electronic properties of the adsorption of Li, Na, K and Ca atoms on Ti_3C_2. Our results show a linear relationship between the effective ion radius, maximum adatom content, and capacities for alkali metals. Charge transfer determines the effective radius of ions, which plays a critical role during the metal-ion adsorption on the surface. Larger effective ionic radius enhances interaction between alkali atoms, thus lowering maximum adatom content and theoretical capacity of the alkali metals. Our calculated capacity values for Li, Na, K and Ca on Ti_3C_2 are 447.8, 351.8, 191.8, and 319.8 mAh/g, respectively. A simple expression to predict capacity by examining effective ionic radius is proposed here. Our results give insights for further experimental work in exploring and developing the potential of Ti_3C_2 for Li, Na, K, or Ca battery applications. It is noteworthy that Ti_3C_2 is only one member of the MXene family. We also simulated Ti_4N_3 nitride MXenes with terminations and determined the stability of surface functional groups. Bare, non-terminated Ti_4N_3 is calculated to have the highest density of states and good magnetic property, which may facilitate the realization of other energy applications. MXenes are promising electrode materials for energy storage applications.

Chapter 3 Defective Graphene and Graphene allotropes as High-capacity Anode Materials for Mg Ion Batteries

Reprint (adapted) with permission from **D. Er**, E. Detsi, H. Kumar, and V. B. Shenoy. *Defective Graphene and Graphene Allotropes as High Capacity Anode Materials for Mg-ion Batteries*. **ACS Energy Letters**, 1, 638-645 August 2016

Synopsis

Although rechargeable Mg ion batteries have recently received renewed interest as a promising alternative to Li ion batteries, the Mg metal used for anodes in state-of- the-art Mg ion batteries is not compatible with conventional battery electrolyte solvents. On the other hand, graphite electrode materials function well with common battery electrolyte solvents, but Mg intercalation into graphite is very difficult. In the case of two-dimensional (2D) carbon- based materials, pristine graphene, the most well-studied 2D material, is known to have no capacity for Li or Mg. Here we demonstrate the potential of defective 2D carbon-based structures to be used as high-capacity anode materials for Mg ion batteries. Adsorption of divalent Mg ions on defective graphene and graphene allotropes is predicted by first-principles density functional theory. Our results show enhanced Mg adsorption on both defective graphene and graphene allotropes. Moreover, we show that Mg storage capacity can be improved by increasing the defect concentration or changing the local arrangement of carbon rings. A Mg storage capacity as high as 1042 mAh/g can be achieved in graphene with 25% divacancy defects. These new insights, together with the fact that carbon-based materials are very compatible with a wide range of battery

electrolyte solvents, will pave the way for developing carbon-based anode materials for practical Mg ion batteries.

3.1 Introduction

The increasing demand for Li-ion batteries in new applications is associated with an ever-growing concern about the non-availability of raw Li resources. As discussed in the previous chapter, efforts have been made to utilize Na, K, Ca-ion batteries beyond LIBs. Another important candidate, namely Mg, has recently received renewed interest as promising alternative to Li-ion batteries. Current Mg metal used as anode in state-of-the-art Mg-ion batteries is not compatible with conventional battery electrolyte solvents. On the other hand, graphite electrode materials are very compatible with common battery electrolyte solvents, but Mg intercalation into graphite is very difficult. In the case of two-dimensional (2D) carbon-based materials, pristine graphene, the most well-studied 2D material, is known to have no capacity for Li or Mg storage. In this context, we are interested in realizing Mg ions by searching successful 2D carbon-based material candidates as battery anodes.

First, the enthusiasm for Mg-ion battery is justified by the fact that on the contrary to Li, Mg is non-dendritic and Mg metal is much safer than Li metal. However, the emergence of Mg-ion batteries is severely hampered by the absence of practical anode materials that can operate in common battery electrolyte solvents. While commercialized Li-ion batteries exploit the reversible insertion of Li between graphite layers used as anode, state-of-the-art Mg-ion batteries exploit on the other hand the reversible plating of Mg onto Mg metal surfaces used as anodes.[86] Unfortunately, exposure of Mg metal to conventional battery electrolyte solvents results in the formation of reduction products at the Mg metal/electrolyte interface, the so-called "blocking layer", [86] which impedes the diffusion of Mg ions, preventing in that way the plating Mg onto Mg metal surfaces used as anodes. Alternative anode materials for Mg storage that are compatible with conventional battery electrolyte solvents are therefore highly desirable.

2D materials are promising for electrode applications due to their large surface-to-mass ratio, open morphology, and unique physical properties.[66,87–90] Among the 2D materials, graphene has attracted much attention since its discovery in 2004; however, pristine graphene cannot be used as electrodes due to Li repulsion and clustering.[91,92] Recent experiments and theoretical studies suggest that enhanced Li storage capacities can be achieved in carbon structures locally modified by introduction of impurities and defects. For example, defective graphene (i.e. porous graphene system) offers a very high specific capacity for Li storage, exceeding 850 mAh/g with excellent reversibility.[93] Beyond Li, defective carbon systems can also provide a solution to MIBs. Datta *et al.*[56,94] have demonstrated that the increased amount of defects in graphene can enhance the charge transfer between ions and the host 2D sheets, and hence can boost Li, Na, and Ca storage capacities more than 1200, 1450, and 2900 mAh/g, respectively.

Defect structures beyond single vacancies can be introduced with the involvement of substantial rearrangements of the carbon lattice. Crespi suggested that graphene allotropes with zero net curvature could form two-dimensional crystals and predicted the relationship between accumulated defects concentration and rearrangements with the formation of graphene allotropes. [95] For example, a relationship between allotropes and defects was established by showing that pentaheptite and Haeckelite can be theoretically constructed using Stone-Wales (SW) defects.[96–99] In general, graphene allotropes can be created by using patterned defects.[98,100–102] In reality, this prediction has been demonstrated experimentally via a cross-coupling reaction in Graphdiyne with hexagons interconnected by linear carbon chains with sp and sp2 hybridization.[103] The synthesized Graphdiyne has demonstrated not only excellent semiconducting properties with a conductivity of 2.516×10^4 S/m but also a promising photocatalytic performance on TiO_2 substrates.[103,104] The great structural similarity between these defect-induced allotropes and graphene provides a promising opportunity for MIB applications (**Figure 3-1**). In particular, since carbon-based materials are compatible with a wide range of battery electrolyte solvents, defective graphene and graphene allotropes will be very attractive as alternative anode materials for practical Mg-ion batteries. Here we demonstrate the great potential of these 2D materials as high-capacity electrode materials for Mg-ion batteries. This is done by scrutinizing fundamental open questions such as: (a) What are the desired defect and allotrope structures for Mg storage applications? (b) Why will these carbon-based structures allow the storage of Mg ions? (c) How can the Mg storage capacity be improved? To answer these questions, we have carried out a first-principles calculation based on DFT to study the adsorption of divalent Mg ions on defective graphene and graphene allotropes. We have compared adsorption of Mg ions on synthesized defective graphene and predicted graphene allotropes, paving the way for designing high-performance graphene allotropes for Mg-ion battery electrodes. We have systematically predicted the Mg storage capacity of graphene with different concentrations of single vacancy (SV) and divacancy (DV) defects, and the storage capacity of other promising graphene allotropes.

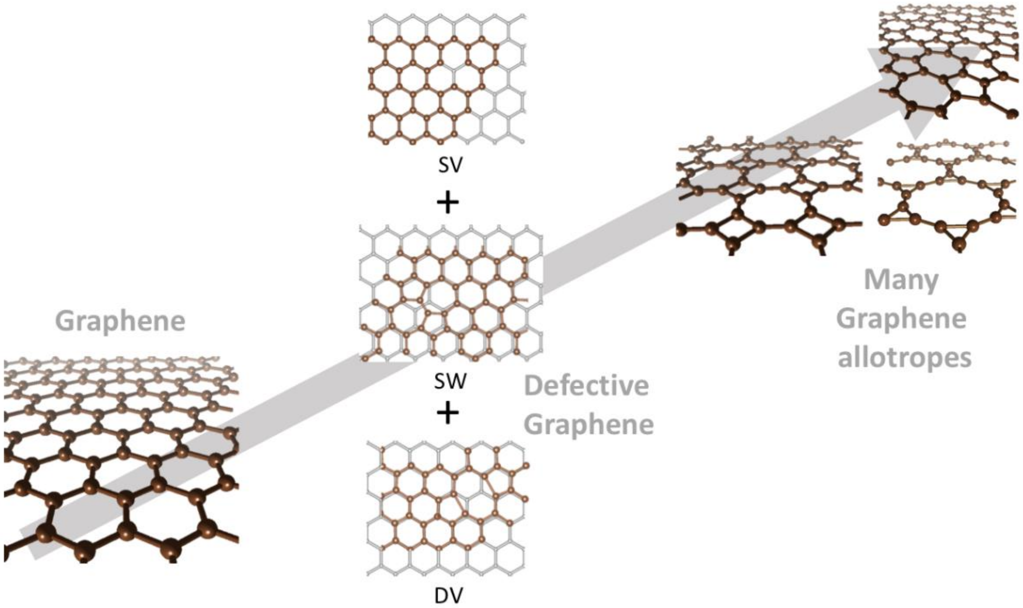

Figure 3-1 Graphene can construct different allotropes by introducing proper combination and manipulation of single vacancies, divacancies, and Stone-Wales defects. The rearrangement requires high energy. Overlay serves as eye-guidance to identify defects.

3.2 Method

All of our calculations were performed using VASP based on first-principles density functional theory (DFT) with the Perdew−Burke−Ernzerhof (PBE) type of generalized gradient approximation (GGA) for exchange and correlation functionals and the projector augmented wave pseudopotential (PAW) for electron−core interactions.[79–81] The ion−electron interactions in C and Mg are described using their valence electrons, $2s^2 2p^2$ and $3s^2$, respectively. An energy cutoff of 580 eV was used for the plane-wave basis expansion. The Brillouin zone of the unit cell and the 4 × 4 × 1 supercell were sampled with a Γ-centered k-point mesh of 12 × 12 × 1 and 3 × 3 × 1, respectively. The energy convergence limit was set to less than 5×10^{-6} eV/atom, while the force tolerance on each atom was less than 0.01 eV/Å in order to obtain fully relaxed structures. To avoid the interaction between periodic graphene allotrope layers along the normal direction, a vacuum separation larger than 20 Å was used. The OCV can be estimated similarly to that in **section 2.2**, where the only difference is that the calculated cohesive energy for *hcp* Mg is 1.519 eV/atom.

3.3 Results

3.3.1 Stability of allotropes from patterned defects

Prior to investigating Mg adsorption on defective graphene and graphene allotropes, we first discuss their relative stability in order to search for the most stable defective structures that could be promising as anode materials. The simplest defect in carbon networks is the carbon SV. Experimentally, the SV has been observed by TEM and STM,[99,105–107] showing a Jahn-Teller distortion of the first neighbors near the missing carbon atom. The creation of such defects is energetic costly with a formation energy about 7.63 eV,[108,109] which is intuitively reasonable because of the presence of under-coordinated carbon atoms. One way to stabilize the structure and minimize the effect of dangling bonds is to introduce the DV, where a C-C dimer is removed from pristine graphene and two dangling bonds are connected with each other with a lowered formation energy per atom (4.04 eV/atom) that of SV. Therefore, DV is more thermodynamically favorable than SV, and it has been experimentally demonstrated that low-concentration monovacancies created by electron irradiation quickly convert to divacancies.[99,110] When the concentration of defects (SV &

DV) increases, topological disorders become more energetically favorable due to the fact that it introduces no extra dangling bonds.[111] For instance, SW defect can be formed by the carbon bond rotation by 90° with respect to the midpoint of the C-C bond followed by local structure reconstruction so that four hexagons transform to two pentagons and two heptagons.[112] It is the simplest topological defect system with the lowest formation energy in all graphenic systems.[111] For the simplest SW(55-77) defect, it requires about 5 eV to create such defects in graphene.[108] Due to the nature of topological defects, the structure has the same amount of carbon atoms as pristine graphene with a different structural arrangement and no dangling bonds. Therefore, larger amount of SW defects can be introduced in carbon networks—even it is possible to have Haeckelite that is composed of 100% SW defects.[113]

In fact, a proper combination of defects and topological disorders can generate more energetically favorable structures and provide ways for constructing patterned complex graphene allotropes that are promising for battery applications.[96] For example, the rotation of one of the bonds in octagon in the V_2(5-8-5) defect leads to a lower energy complex of three pentagons and three heptagons V_2(555-777) followed by another step to an even lower energy complex of V_2(5555-6-7777).[114] Further evolvement spans larger region on the defective graphene and forms graphene allotropes, in which the reconstruction of vacancies and topological defects (known as nanoengineered structures) leads to lower equilibrium energy structures (**Figure 3-1**). Therefore, it is possible to construct graphene allotropes solely from rational manipulations of defects and polygons by nanoengineering. In this context, we are searching for stable graphene allotropes that are only composed of carbon polygons as promising anode materials. Many structures have been predicted and studied to date, such as Graphdiyne (synthesized in 2010), [103,115] graphynes,[97,102,116,117] pentahexoctite,[101] graphenylene,[118,119] and biphenylene.[120] Among these graphene allotropes, the C_{3-12} (**Figure 3-2i**) structure composed of triangles and dodecagons, and C_{4-8} (**Figure 3-2j**) structures composed of tetragons and octagons are of interest because of their relative high stability and moderate size of pores, which are beneficial for ion mobility and high-rate performance. The fully relaxed allotrope structures in supercell are shown in

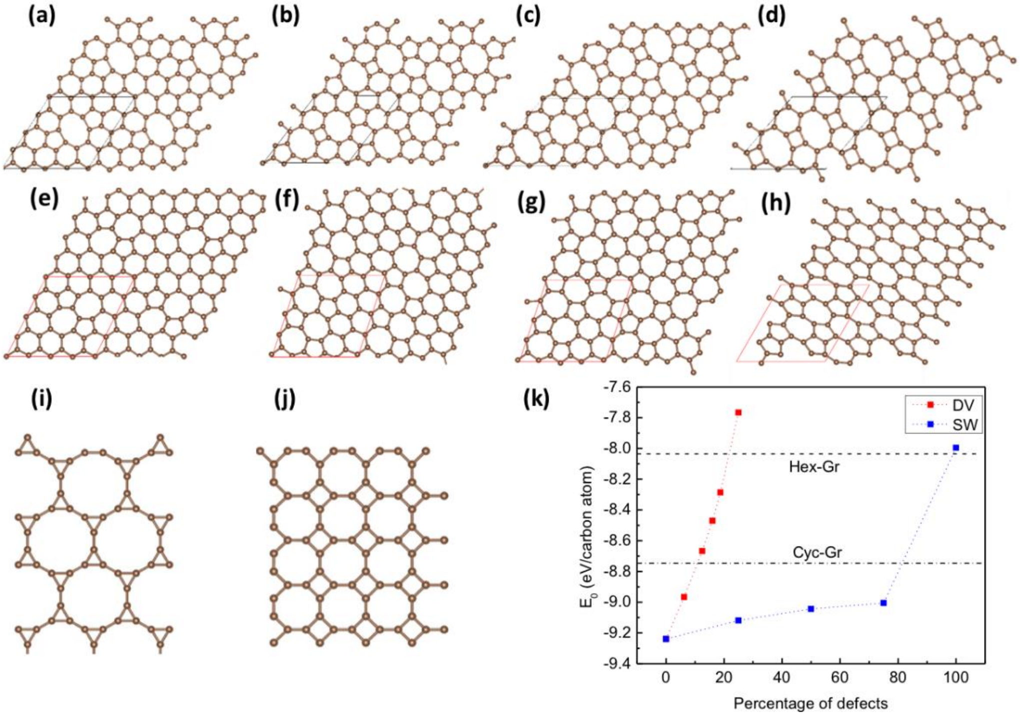

Figure 3-2 (upper row) Graphene with DV defects: **(a)** 6.25, **(b)** 12.50, **(c)** 18.75, and **(d)** 25%. (middle) Graphene with SW defects: **(e)** 25, **(f)** 50, **(g)** 75, and **(h)** 100%. Systems shown here are in a 2×2 supercell with highlighted unit cell. All structures are fully relaxed. (lower) Graphene allotrope structures of **(i)** cyclic network composed of C_{3-12} rings, and **(j)** octagonal network composed of C_{4-8} rings. **(k)** The equilibrium energy per carbon atom for different percentage of defects. Two horizontal guidelines represent cyclic and octagonal networks.

Figure 3-2. The lattice constant of graphene is 2.46 Å, while it expanses to 2.77 and 3.44Å for $C_{3\text{-}12}$ and $C_{4\text{-}8}$, respectively. **Figure 3-2 k** indicates that they are even more stable than the Haeckelite, which are composed of high-concentration DV or SW defects.

In this chapter, we compared DV with four different defects concentrations (6.25, 12.50, 18.75, and 25.00%; **Figure 3-2 a-d**) and SW also with four different defects concentrations (25, 50, 75, and 100%; **Figure 3-2 e-h**), concluding that the equilibrium energy per carbon atom increases with the amount of defects and that the SW defect is more favorable in high-concentrations regime.

3.3.2 Mg adsorption on defective graphene and graphene allotropes

We first consider the single adatom adsorption on monolayer defective graphene systems with the lowest defect density in order to identify adsorption sites. From previous study, we know that adatoms tend to cluster around the defective zone; therefore, we select the adatom adsorption location that has the maximum defective neighbor (MDN) in the lowest defect density structures, that is 6.25 % DV and 25% SW defect.[94] The bridge site (in the middle of a carbon−carbon bond) and the top site (right above a carbon atom) have been tested, and both of them are less energetically favorable than the hollow site, with an energy difference higher than 0.445 and 0.543 eV, respectively. Therefore, we consider the adsorption sites over defects in the following way: in the center of small rings (denoted by S) and in the center of large rings (denoted by L). For example, one may consider the pentagons in DV as S sites, while the octagons in DV as L sites (**Figure 3-2a**). Similarly, in the case of SW defects, pentagons and heptagons can be considered as S and L sites, respectively (**Figure 3-2e**). The potentials of Mg insertion at different sites are summarized in **Table 3-1**, in which we can see that both DV and SW defects have negative OCV values for the lowest defect concentrations (6.25 and 25%, for DV and SW, respectively). As discussed above for Eq. (2-5), these negative potential values indicate that Mg storage in DV and SW structures with the lowest concentrations is not favorable..[56] We note that the S site has a less negative potential than the L site, which suggests that S sites are potentially preferred for adsorption if the defect concentration increases.

Likewise, we first define high symmetric adsorption sites (S and L) on two promising graphene allotropes, namely $C_{3\text{-}12}$ and $C_{4\text{-}8}$. For example, the center of the triangles in C_{3-12} can be viewed as the S site, while the center of the dodecagons is the L site. Similarly, the S and L sites in $C_{4\text{-}8}$ can be defined as at the centers of quadrangles and octagons, respectively. As discussed in **section 3.1**, these two allotropes are metastable with higher energy than low-concentration SW & DV graphene, whereas the equilibrium energy per atom is comparable to that of high-concentration SW & DV graphene allotropes. For this reason, the adsorption of Mg on these allotropes is equivalent to that on defective structures with moderate defect concentrations. Therefore, the introduction of foreign ions may decrease the total energy of the system to the level that the Mg potential is positive. The Mg potentials of these two graphene allotropes ($C_{3\text{-}12}$ and $C_{4\text{-}8}$) are also summarized in **Table 3-1**. The OCVs are positive, on the contrary of the negative OCVs values reported above for DV and SW defective graphene with low defect concentrations. Referring again to Eq. (2-5), these positive OCV values mean that Mg absorption on S and L sites of C_{3-12} and C_{4-8} graphene allotropes is favorable. Although the Mg adsorption potential at the S site is slightly larger than that at the L site for these two graphene allotropes, as shown in

Table 3-1, the Mg adsorption potential on the S site is metastable and introduces large local curvatures to the allotropes. For this reason, the L site is selected for these graphene allotropes.

Table 3-1 OCV and charge transfer from Mg to possible sites in different defective graphene and graphene allotropes.

	OCV (eV)				Charge transfer (e)			
	DV	SW	C_{3-12}	C_{4-8}	DV	SW	C_{3-12}	C_{4-8}
S	-0.20	-0.29	0.24	0.42	0.62	0.95	1.10	0.94
L	-0.23	-0.40	0.20	0.35	0.82	1.12	1.53	1.04

To get further physical insight on the adsorption of Mg on both defective graphene and graphene allotropes, we calculated the amount of charge transfer between adatoms and 2D

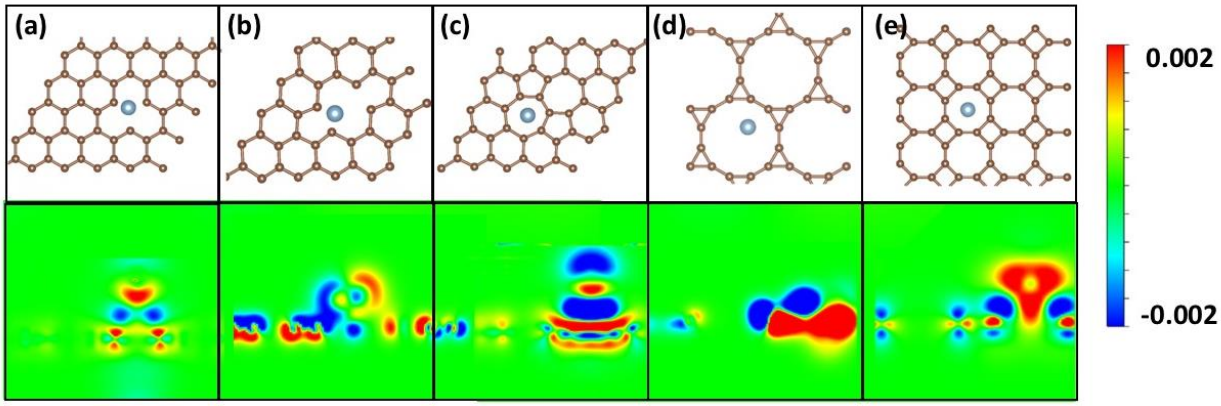

Figure 3-3 Adsorption and charge transfer of Mg on the most stable regions of graphene with single vacancy **(a)**, DV defective graphene **(b)**, and SW defective graphene **(c)**. C_{3-12} graphene allotropes **(d)**, and C_{4-8} graphene allotropes **(e)**. Red and blue colors indicate the electron accumulation and depletion, respectively. The isosurface level is set to 0.002 e/Bohr^3.

carbon sheets. **Figure 3-3** illustrates the bonding charge density flowing from adatoms to the nearest carbon atoms in different 2D carbon networks. The red (positive values) and blue (negative values) colors indicate the electron accumulation and depletion, respectively. To quantify the amount of charge transfer, we carried the Bader charge analysis[121] that determines the total electron charge of an atom in the enclosed Bader volume for different sites as shown in **Table 3-1**. The number of electrons transferred from Mg adatom to pristine graphene is 0.103, which corresponds to only 5.15% of the total charge of Mg ion. That number of electrons increases to 0.620 (i.e. 31.0 % of the total charge of Mg ion) and 0.951 (i.e. 47.5 % of the total charge of Mg ion) in DV and SW defective graphene with low defect concentrations, respectively. We note from the data in **Table 3-1** that for the DV and SW structures the L sites with lower OCV values (i.e., large negative OCVs) have higher levels of charge transferred to graphene than the S sites with relatively higher OCV values (i.e., less negative OCVs). On the contrary, the situation is different for C_{3-12} and C_{4-8} graphene allotropes; the L sites with higher OCVs values show higher levels of charge transfer than the S sites with relatively lower OCV values. The level of charge transfer in graphene allotropes reaches 1.530 (76.5% of the total charge of the Mg ion) and 1.040 (52.0% of the total charge of the Mg ion) for C_{3-12} and C_{4-8}, respectively. Larger charge transfer results in stronger electrostatic interactions between the adatom and the graphenic network, where a certain threshold of charge transfer exists (~0.89 |e| or 44.5% of the total charge of the Mg ion), beyond which OCVs become positive and start to favor Mg adsorption.

3.3.3 Enhanced Mg capacity on defective graphene and graphene allotropes

After identifying the favorable adsorption sites for a single Mg adatom on different carbon networks, we focused on studying the distribution of Mg adatoms with higher concentrations based on the initial positions. For each composition, we generated various configurations by randomly distributing the adatoms near high symmetry points. For each case, we considered 10 different possible initial positions and report the highest value of the OCV. We carried out DFT calculations for different concentrations of defects (DV and SW) and different graphene allotropes until we reached the maximum coverage of adatoms when the OCV changed its sign from positive to negative. **Figure 3-4** summarizes the OCV changes for different concentrations of SW defects during Mg adsorption. Similar to the observation that Mg cannot be absorbed on pristine graphene, low SW defect density does not favor adsorption of Mg anywhere on the graphene sheet. However, with an increased defect concentration to 100% (haeckelite), Mg ions start to bind onto the defective graphene sheets. In the case of 100% SW defects, the initial potential exceeds 1.6 V and decreases with the increasing coverage of adatoms gradually. The OCV drops to zero near the coverage of 65%, which corresponds to the maximum capacity. Likewise, for DV defects, the lowest concentration does not favor Mg adsorption, while it is possible in defective graphene with higher DV concentrations (12.5, 18.75, and 25.00%). From **Figure 3-4**, we conclude that in a graphene structure with 25% DVs the maximum coverage for the Mg adatom is about 70% of its theoretical value. All OCVs drop with increased Mg concentration monotonically. Moreover, the initial values of OCV increase with increased DV concentrations, which is reasonable because defective graphene with higher DV concentration can accommodate more Mg atoms (**Figure 3-4**). Therefore, the Mg capacity in a structure with high DV concentration should be higher than that with low DV concentrations. We further evaluated the rate performance of 25% DV defective graphene by calculating the diffusion barrier, a key factor that determines the rate of charging and

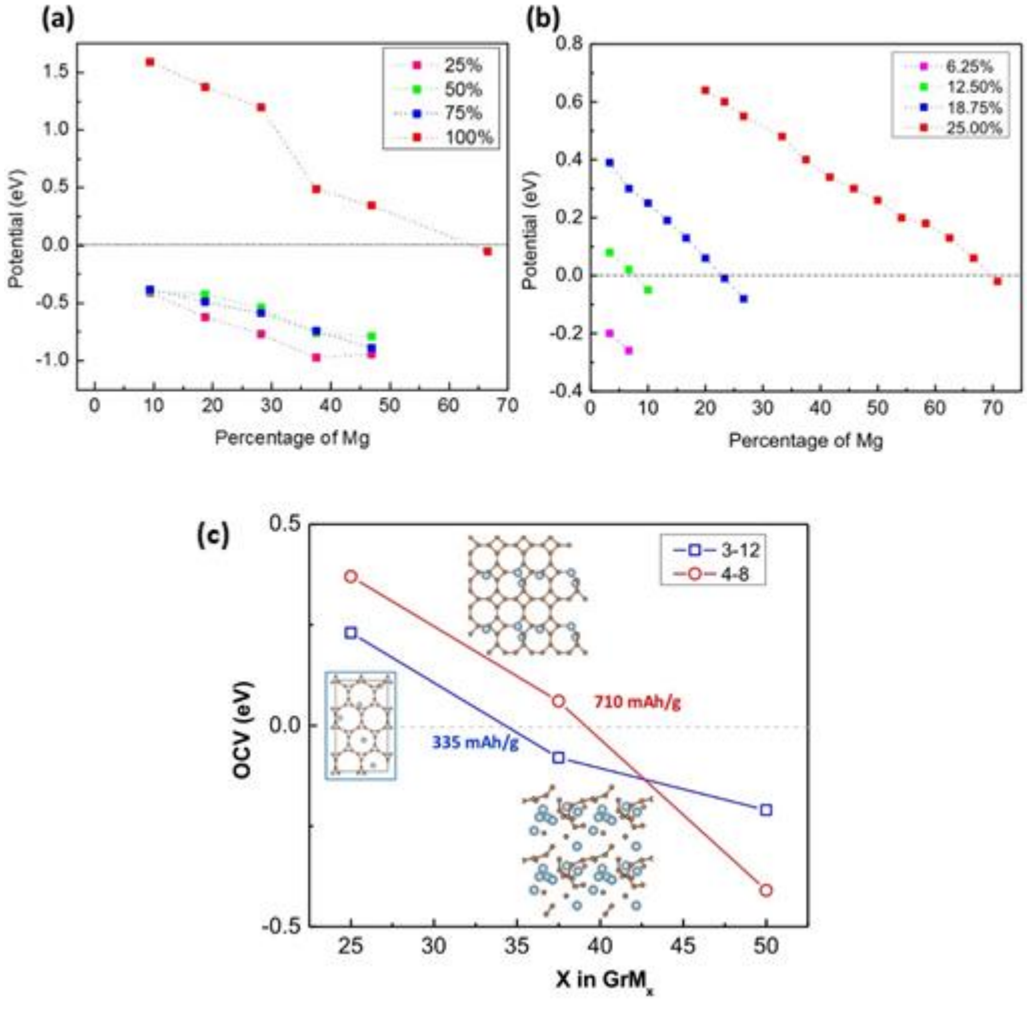

Figure 3-4 OCVs as a function of Mg adatom concentration on graphene with **(a)** SW and **(b)** DV defects, and on the cyclic (C_{3-12}) and octagonal (C_{4-8}) graphene allotropes **(c)**. The zero OCV corresponds to the maximum adatom content and capacity for Mg.

discharging. We used the nudged elastic band (NEB) method as implemented in the Vienna ab initio simulation package (VASP) code to generate diffusion pathways for Mg between two neighboring sites and identify the diffusion barrier along the minimum-energy path.[83] Our calculations show that the diffusion barrier for Mg migration is relatively small (0.1 eV) compared to that for other electrode materials (0.3− 1.0 eV) for MIBs.[90,122,123] Hence, 25% DV graphene is a promising candidate as a high-rate-performance anode material for Mg batteries.

In two representative graphene allotropes, namely, C_{3-12} and C_{4-8}, we observed a similar monotonically decreasing trend in OCVs, as shown in **Figure 3-4**. It should be noted that in graphene allotropes the composition is fixed; therefore, the defect concentration does not vary. In **Figure 3-5** we evaluated the maximum adatom content and hence the maximum capacities (C_M) for Mg on defective graphene and two graphene allotropes according to:

$$C_M = \frac{1}{M_{\text{tot}}}[x_{max} \times z \times F \times 10^3] \tag{3-1}$$

where z is the valence number of adatom (Mg=2), $x_{\max}$ is the maximum adatom content, M_{tot} is the sum of atomic masses of the corresponding carbon networks and Mg atoms, and F is the Faraday constant (26.81 Ah/mol). The factor 10^3 in Eq. 3-2 is associated with the conversion of C_M from Ah/g to mAh/g. For the highest DV density of 25%, the maximum Mg storage capacity is as high as 1042 mAh/g, which is very promising for Mg ion battery applications. A significantly enhanced Mg storage capacity of ∼960 mAh/g is also achieved on SW structures with 100% defect concentration, that is, the haeckelite structure. It is worth noting that, unlike ultralight Li element (m_{Li} = 6.9), the mass of Mg (m_{Mg} =

24.3) should not be neglected when evaluating the capacity of electrodes.[124,125] Two graphene allotropes show moderate capacities for Mg storage (**Figure 3-5**). As noted earlier, the main drawback of Mg metal anodes currently used in Mg ion batteries corresponds to their high reactivity with conventional battery electrolyte solvents, which results in the formation of a "blocking layer" at the Mg metal/electrolyte interface that impedes the diffusion of Mg ions in the material.[86] In contrast to Mg metal, carbon-based materials, including defective graphene and graphene allotropes, do not react with common battery electrolyte solvents. The high compatibility of carbon- based materials with standard electrolyte solvents combined with the high Mg storage capacities reported here in defective graphene and graphene allotropes shows much promise in the design of the next-generation cost-effective Mg ion battery electrodes.

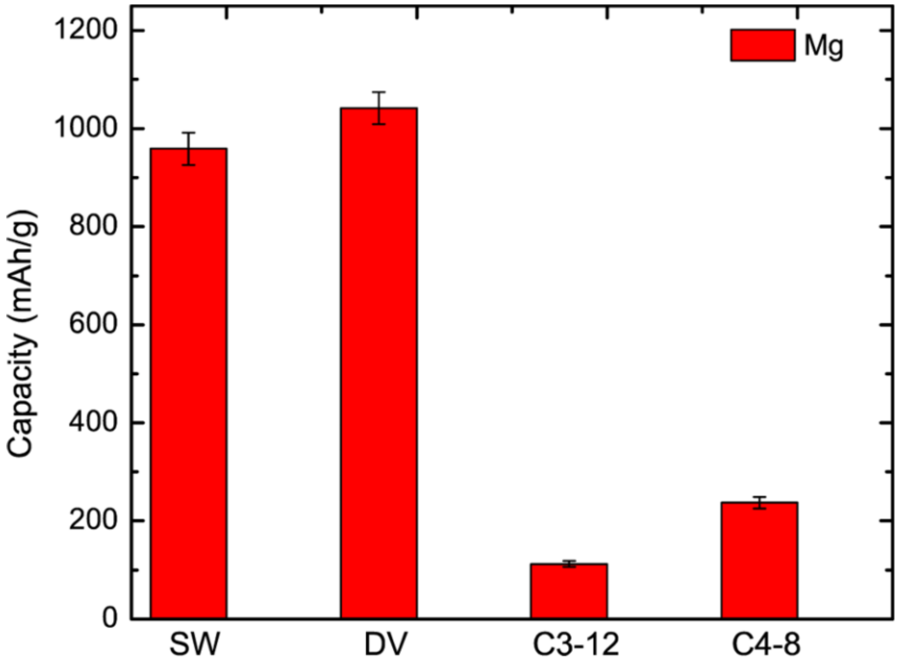

Figure 3-5 Maximum capacities for Mg absorbed onto different defective graphene and graphene allotropes. Error bars indicate the variation in capacity range based on the OCV changes.

3.4 Conclusion

In summary, first-principles calculations were performed to study Mg adsorption on various 2D carbon networks. The first set of material systems investigated consisted of DV and SW defective graphene structures with a wide range of defect concentrations, and the second set included two promising graphene allotropes, C_{3-12} and C_{4-8} composed of polygons. Although Mg cannot be stored in defect-free pristine graphene, our work shows that defective graphene and graphene allotropes are suitable for Mg storage; a high concentration of vacancies and topological defects in these structures significantly enhances their Mg storage capacities. Detailed analysis of both the Mg adsorption potential and the corresponding level of charge transfer in these structures shows that Mg adsorption is more favorable near the defect-rich regions. A Mg storage capacity of 1042 mAh/g was achieved in DV defective structures with a defect density of 25%. The two promising graphene allotropes provide moderate Mg capacity and possible solutions to high-rate performance MIBs. More importantly, our results provide physical insights into the mechanisms of enhancement of multivalent ion adsorption onto defective graphene and graphene allotropes. A straightforward application highlighted in this work is in the development of high-capacity anode materials for Mg ion batteries. We hope that this work can guide experimental work and draw more attentions to this topic in order to realize better multivalent electrochemical energy storage systems.

.

Chapter 4 Activating the 2D MoS_2 nanosheet catalysts: The role of electronic coupling between substrate and 2D MoS_2 nanosheets in electrocatalytic production of hydrogen

Reprinted (adapted) with permission from D. Voiry, R. Fullon, J. Yang, C. Silva, R. Kappera, I. Bozkurt, D. Kaplan, M. J. Lagos, P. E. Batson, G. Gupta, A. D. Mohite, L. Dong, **D. Er**, V. B. Shenoy, T. Asefa, and M. Chhowalla. *The Role of Electronic Coupling between Substrate and 2D MoS_2 Nanosheets on Electro-Catalytic Production of Hydrogen*. **Nature Materials**, 15, 1003–1009 June 2016

Synopsis

The excellent catalytic activity of metallic MoS_2 edges for the hydrogen evolution reaction (HER) has led to substantial efforts towards increasing the edge concentration. The 2H basal plane is less active for the HER because it is less conducting and therefore possesses less efficient charge transfer kinetics. Here we show that the activity of the 2H basal planes of monolayer MoS_2 nanosheets can be made comparable to state-of-the-art catalytic properties of metallic edges and the 1T phase by improving the electrical coupling between the substrate and the catalyst so that electron injection from the electrode and transport to the catalyst active site is facilitated. Phase-engineered low-resistance contacts on monolayer 2H-phase MoS_2 basal plane lead to higher efficiency of charge injection in the nanosheets so that its intrinsic activity towards the HER can be measured. We demonstrate that onset potentials and Tafel slopes of ∼−0.1 V and

~50 mV per decade can be achieved from 2H-phase catalysts where only the basal plane is exposed. We show that efficient charge injection and the presence of naturally occurring sulfur vacancies are responsible for the observed increase in catalytic activity of the 2H basal plane. Our results provide new insights into the role of contact resistance and charge transport on the performance of two-dimensional MoS_2 nanosheet catalysts for the HER.

4.1 Introduction

The development of catalysts from earth-abundant and inexpensive materials is essential for the implementation of clean energy technologies using hydrogen.[14,126–128] Transition metal dichalcogenides such as MoS_2 and WS_2 have emerged as promising catalysts for the hydrogen evolution reaction (HER) in acidic media.[129–131] Substantial work has been devoted to understanding and optimizing the catalytic properties of these materials.[38,40,132–136] Pioneering work by Jaramillo *et al.*[38] has shown that it is the metallic edges of ultrahigh-vacuum-grown MoS_2 nanoclusters that are catalytically active whereas the less conducting 2H basal plane remains relatively inactive. Numerous follow-up studies have demonstrated that increasing the concentration of exposed edges can lead to improvements in catalytic performance.[137–140] Recent work has suggested that enhancing the conductivity of the basal plane by phase transformation from the semiconducting 2H phase to the metallic 1T phase also leads to an improvement in performance.[40,134,141] In the case of 1T-phase MoS_2 and WS_2, the catalytic properties seem to be independent of the edges and primarily dependent on the concentration of the metallic phase.[21,40] Theoretical studies have suggested that, for the same catalyst, it is possible to improve the catalytic performance by enhancing the coupling between the substrate and the active material to decrease the energy of hydrogen adsorption.[142] In addition, the role of electrical coupling between the substrate and catalysts on the cathode and resulting charge transfer kinetics has also been reported to be important.[21,141,143,144] Thus, facilitating charge transfer through engineering better electrical contacts between the support and catalyst nanoparticles is an additional important variable.

4.2 **Method**

4.2.1 Experimental set-up

In electrocatalysis, the substrate supports the catalyst material and injects or collects charge carriers from the electrocatalyst. In this chapter, to estimate the contact resistance of individual catalyst nanosheets, the supporting substrate cannot be conducting. We used SiO_2 on Si wafers. The gold contacts deposited on the MoS_2 nanosheets are therefore the electrical contacts and thus act as conducting substrates. We demonstrate that the basal plane of the 2H phase can be as catalytically active as the edges or the 1T phase. A key parameter in increasing the catalytic activity of the 2H basal plane is the enhancement of the charge transfer from the substrate to the catalyst active sites by reducing the contact resistance and improving the conductivity of the catalyst. To demonstrate this, we have carried out a study to understand the role of edges, phases, doping and electrical coupling (or the contact resistance) on the catalytic properties by measuring the HER performance of individual monolayers of chemical vapor deposited (CVD) MoS_2. We have developed an experimental set-up to measure the catalytic activity of individual nanosheets of MoS_2, as shown in **Figure 4-1 a,b**. By using electron beam lithography patterning, we have been able to measure the catalytic properties of only the basal plane (while covering the edges,

Figure 4-1c) or only the edges (while covering the basal plane, **Figure 4-1d**). The devices in **Figure 4-1 c,d** are top-contacted, but bottom-contacted devices were also tested. The

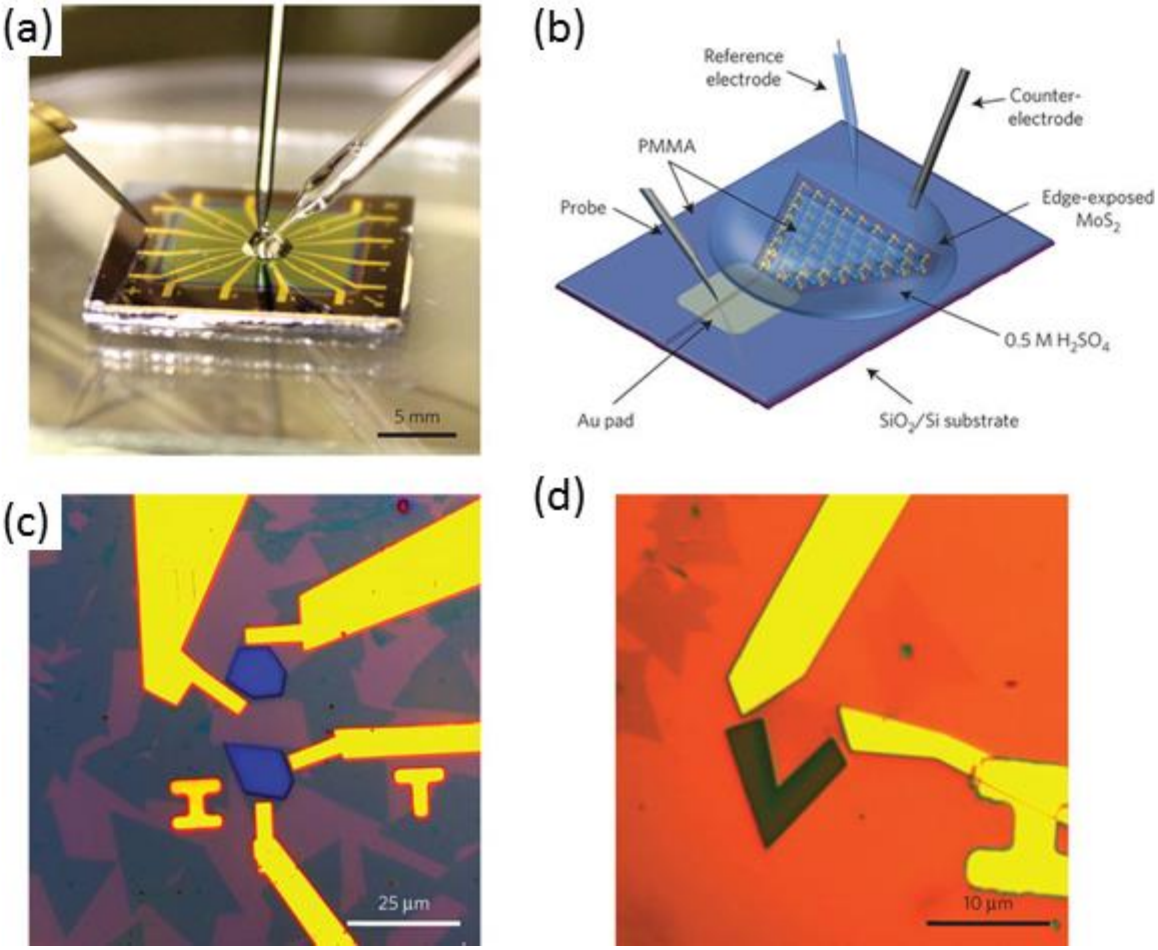

Figure 4-1 (a) Photograph of the electrochemical microcell. **(b)** Schematic of the set-up showing single layer of MoS_2 deposited on $SiO_2$and contacted by one gold electrode. Glassy carbon and Ag/AgCl electrodes are used as counter and reference electrode, respectively. The entire substrate is covered with poly(methylmethacrylate) PMMA, with the exception of a window on top of the edges of the MoS_2 nanosheet. Only the MoS_2 nanosheet is in contact with the electrolyte solution (0.5 M H_2SO_4). Edge-exposed and edge-covered cells can be fabricated and tested. (**c**, **d)** Optical microscope images of the different types of microcells: CVD-grown single-layer MoS_2 having their edge covered (**c**) or exposed (**d**). Such cells enable one to control precisely the quantity of MoS_2 sites exposed and thus an accurate estimation of the number of turnovers at each active site.

electrical properties of top- and bottom-contacted devices are similar, suggesting that the charge injection mechanism in both cases is the same. In addition, we have been able to engineer the phases to compare the catalytic performance of the metallic and semiconducting phases. The catalytic properties of the individual monolayer MoS_2 nanosheets were measured using a three-electrode configuration, with glassy carbon as the counter-electrode, Ag/AgCl electrode as the reference electrode, and one gold pad contacting the single-layer MoS_2 nanosheet as the working electrode. Everything except the MoS_2 was covered with cured poly(methylmethacrylate) (PMMA) resist to ensure that the measured activity was due to the MoS_2 only.

4.2.2 Computational details

The simulations are performed using the VASP code[79] with projector augmented wave pseudopotentials,[80] Perdew–Burke–Ernzerhof (PBE) generalized gradient approximations,[81] and a cutoff energy of 500 eV for plane-wave expansions. A Γ-centered k-point mesh of 12×12×1 and 4×4×1 in the first Brillouin zone is found to yield well-converged results for the MoS_2 unit cell and the supercell, respectively, during the structural relaxations. A vacuum space of 25 Å thick is used to prevent any interactions between the adjacent periodic images of the monolayer. For the calculations of 2×2 2H–MoS_2 supercells with additional electrons, a neutralizing background charge is provided in the VASP code, and the total energy is corrected to exclude the unphysical monopole/dipole interactions between the adjacent periodic images of the monolayer along the surface normal. The atomic positions of the unit cells are optimized until all the components of the forces on each atom are reduced to values below 0.02 eV/Å. The lattice parameters of pristine 2H– and 1T–MoS2 we obtain are both 3.122 Å. Different hydrogen absorption sites on the top of the MoS_2 supercells are investigated in our calculations, and the energetically favorable site is identified as the one on the top of the S atom.

The relative stability of the absorbed hydrogen atom on MoS_2 can be described from the change in Gibbs free energy ($\Delta G_H *$) before and after the absorption as

$$\Delta G_H * = \Delta E + \Delta E_{ZPE} - T\Delta S \tag{4-1}$$

where ΔE is the differential hydrogen adsorption energy, ΔE_{ZPE} is difference in the zero point energy between the absorbed hydrogen atom and hydrogen in the gas phase, T is the temperature, and ΔS is the entropy difference between the adsorbed hydrogen atom and hydrogen in the gas phase. ΔE is calculated as

$$\Delta E = E(Supercell + H) - E(Supercell) - \frac{1}{2}E(H_2) \tag{4-2}$$

where E(supercell+H), E(supercell), and $E(H_2)$ represent the energy of the MoS_2 supercell plus one hydrogen adsorbed, the energy of the MoS_2 supercell, and the energy of one hydrogen molecule in the gas phase. In Eq. (4-1), ΔE_{ZPE} and TΔS are almost the same for the different supercells and are much smaller compared to ΔE. As such, the change in ΔG at different carrier concentration is mostly due to the change in ΔE.

4.3 **Results**

The deposition of metals such as gold directly on top of ultrathin or monolayer semiconducting 2H-phase MoS_2 leads to Schottky contacts (energy barrier of ∼0.2 eV; refs 145–148) that are responsible for the observed high contact resistance.[145,149–152] Furthermore, it is not possible to vary the Schottky barrier height in MoS_2 by using metals of different work functions owing to the Fermi level pinning effect.[153] The contact resistance is also variable, so that values ranging from 1 to 10^6 kΩ mm are possible.[152] However, contact resistance values lower than 1 kΩ mm are difficult to achieve on 2H-phase MoS_2. In contrast, it is generally difficult to make high-resistance contacts on the 1T phase of MoS_2 (Refs 39,154). Thus, the range of contact resistances we obtain for the 1T phase is narrower (between 10^{-5} and 10^{-2} kΩ mm) than for the 2H phase (1–10^6 kΩ mm). The lower contact resistances in the 1T-phase devices are translated into superior HER catalytic performance.[21,40,141]

To differentiate between the contribution of the contacts and the internal resistance of the measurement system, impedance spectroscopy was performed on MoS_2 microcells with varying contact resistances. In electrochemistry, the contact resistance is often subtracted from the measured signal in order to eliminate its influence on the electrochemical performance of the material being tested. This assumes that the contact resistance does not play a significant role in determining the measured catalytic properties. However, we demonstrate that in the case of basal plane of MoS_2, existing catalytic sites are not active at high contact resistance values but can be activated by decreasing the contact resistance to facilitate charge injection. Here, the contact resistance is a variable that we can independently control in our devices, which allows us to investigate the role of charge injection on the catalytic performance. We have recently demonstrated that it is possible to locally engineer the contact resistance by phase engineering.[39,154] That is, locally transforming the 2H phase to the metallic 1T phase and depositing the metal electrode directly on top of the 1T phase allows the realization of low-resistance contacts that are strongly electrically coupled to the 2H phase. We have used this technique to successfully

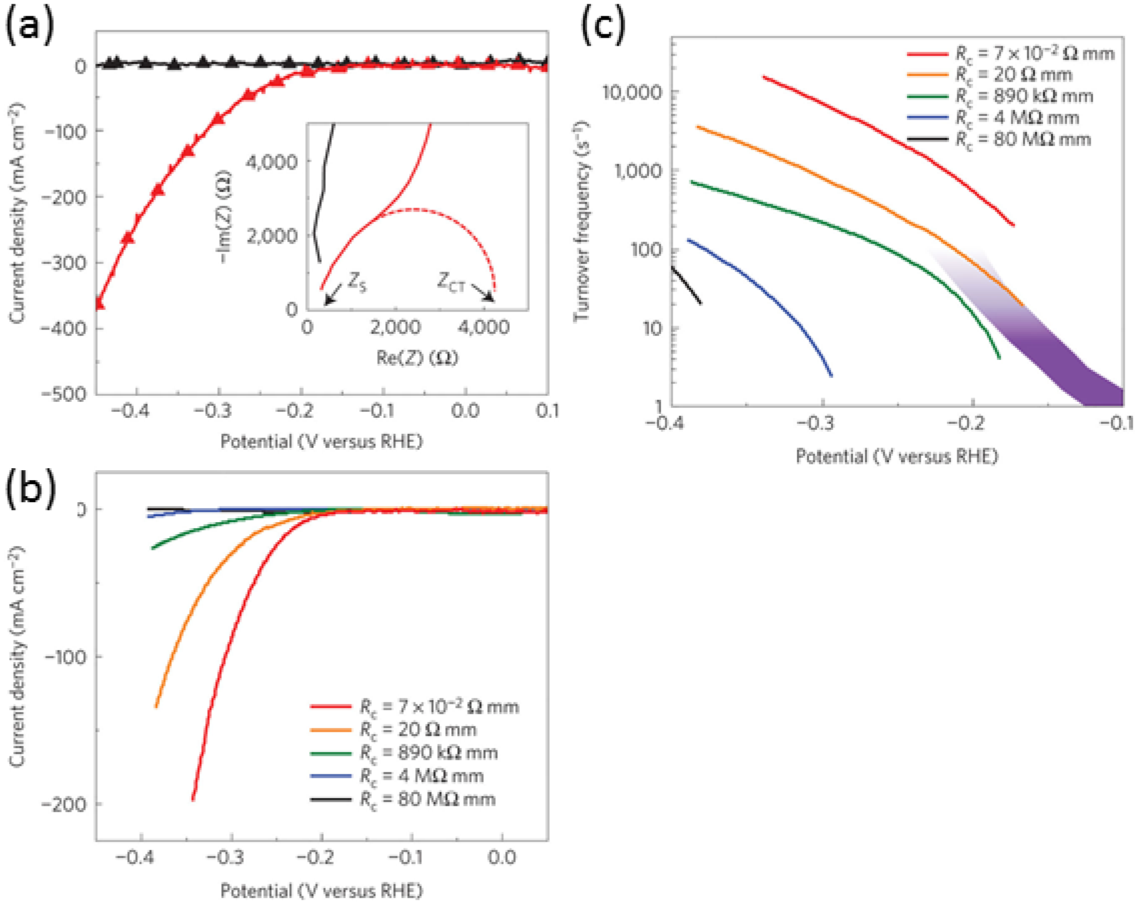

Figure 4-2 (a) Polarization curves measured from two MoS_2 microcells with (solid line) and without iR correction (triangles). Polarization curves from MoS2 microcells with low and high contact resistance are shown in red and black, respectively. Inset: corresponding Nyquist plots showing that the internal resistance (Z_S) ~ 300 Ω does not vary with the contact resistance. The charge transfer resistance (Z_{CT}) is strongly governed by the contact resistance. For the best contact resistance, Z_{CT} ~4,000 Ω can be measured. **(b)** Polarization curves obtained from MoS_2 devices with various contact resistances from 80 MΩ mm down to 7×10^{-2} Ω mm. The performance of the MoS_2 devices increases rapidly with decreasing contact resistance. **(c)**, Evolution of the turnover frequency (TOF) with the overpotential. The TOF values are calculated from the polarization curves presented in a. The quantity of active sites has been estimated assuming that the entire surface of MoS_2 (that is, surface and edge sites) is active. The TOF values are compared to the values obtained from metallic 2H-phase MoS_2 edges grown on gold from Ref 38 (purple region).

reduce the contact resistance in field-effect transistors. [39,154] Furthermore, we have shown that the interface between the patterned 1T phase and the 2H phase is atomically sharp. Typical Nyquist plots obtained from single MoS_2 nanosheets with high and low contact resistances are presented in **Figure 4-2a**. The internal resistance remains relatively small (Z_S~300 Ω) and does not depend on the contact resistance between the MoS_2 and the gold electrode (inset **Figure 4-2a**). The contribution of the internal resistance on the polarization curve remains low, and thus correction of the iR drop is negligible (**Figure 4-2a**). However, the influence of contact resistance can be observed from the marked decrease of the charge transfer resistance (Z_{CT}) in the Nyquist plots (inset **Figure 4-2a**), consistent with results from the literature.[21,141,143,144,155] For high contact resistance, the charge transfer resistance (Z_{CT}), which represents the efficiency of the electron transfer between the gold pads and the MoS_2 nanosheets, becomes virtually infinite. At low contact resistance, the Z_{CT} reduces significantly and reaches ~4,000 Ω, suggesting a large improvement in the efficiency of the electron transfer between gold and MoS_2 (inset **Figure 4-2a**).

The polarization curves of the current density for various contact resistances in 0.5 M H_2SO_4 are shown in **Figure 4-2b**. The measurements in **Figure 4-2b** are averages taken from the 2H and 1T phase, and from the basal plane and edges of numerous samples. It can be seen that the HER performance increases with a decrease in contact resistance, irrespective of whether the edges or basal plane are exposed. The current densities reported here are from flat MoS_2 electrodes, and therefore slightly lower than the high-surface-area mesoscopic electrodes reported in the literature.[139,141,155,156] Electrocatalysis from monolayer MoS_2 allows accurate measurement of the surface exposed to the electrolyte, which can be used to calculate the turnover frequency (TOF), an indicator of the activity of the catalytic sites. The TOF values reported in the literature remain virtually the same,[140] suggesting that the improvement of the electrodes is essentially coming from an increase in the number of active sites and not from an increase in the intrinsic activity of each site. The evolution of the TOF (in s^{-1}) with applied potential for several contact resistances is shown in **Figure 4-2c**. As expected, the TOF values increase with overpotential. For the low-contact-resistance devices, we obtain TOFs of $>100\ s^{-1}$ and $>1{,}000\ s^{-1}$ at overpotentials of 200 mV and 300 mV, respectively. These values compare favorably with other reports based on MoS_2 catalysts. For the lowest contact resistance, the activity of the MoS_2 nanosheets is higher than directly grown MoS_2 clusters on gold reported by Jaramillo *et al.*[38], as shown in **Figure 4-2c**.

The variation of the onset potential and the Tafel slopes with contact resistances are summarized in **Figure 4-3a,b**, respectively, while the current densities (at $\eta = 400$ mV) are shown in **Figure 4-3**. It can be seen that for low-resistance contacts, exceptionally low onset potential <0.15 V and Tafel slopes as low as ∼45 mV per decade can be obtained for the best electrodes (**Figure 4-3a, b**). **Figure 4-3b, c** also reveals that below a critical resistance value of ∼10–100 kΩ mm, the Tafel slope and current density essentially saturate at ∼60 mV per decade and 100 mA cm^{-2}. It can also be seen from **Figure 4-3b, c** that it is possible to obtain similar HER performance in the 2H phase where the edges are covered and therefore do not contribute to the reaction. This shows that the basal plane of the 2H phase, which has been previously thought to be less catalytically active, exhibits HER properties that are consistent with what has been reported in the literature for edges and the 1T phase[21,139–141] by improving the electrical coupling (or reducing the contact resistance) between the substrate and the catalyst.

It is possible to obtain low-resistance contacts in devices where the 2H basal plane is exposed to electrolyte. From **Figure 4-3**, it can be seen that for low-contact-resistance ($\sim 10^{-2}$ kΩ mm) devices where only the 2H-phase MoS_2 basal plane is exposed, the HER performance is indeed comparable to that of 1T-phase and edge-exposed devices. Thus, our results suggest that the catalytic activity of the basal plane and edges of CVD MoS_2, irrespective of the phases, is comparable. This is not surprising because the structures of the 1T and 2H phases of MoS_2 are comparable. However, in the case of 2H-phase MoS_2, the typically high contact resistance limits the Volmer reaction: $H_3O^+ + e^- \rightarrow H_{ads} + H_2O$, which requires efficient charge transfer. That is, if the catalyst material is not sufficiently conducting, then electron transport to the active sites is limited, preventing the Volmer reaction from proceeding. This is indeed demonstrated in **Figure 4-3b**, where the Tafel slope values range from ∼40 to 50 mV per decade for the lowest contact resistance and up to ∼120 mV per decade or higher for the highest values of contact resistance. Tafel slopes of ∼40 mV per decade suggest a Volmer–Heyrovsky mechanism at the surface of MoS_2

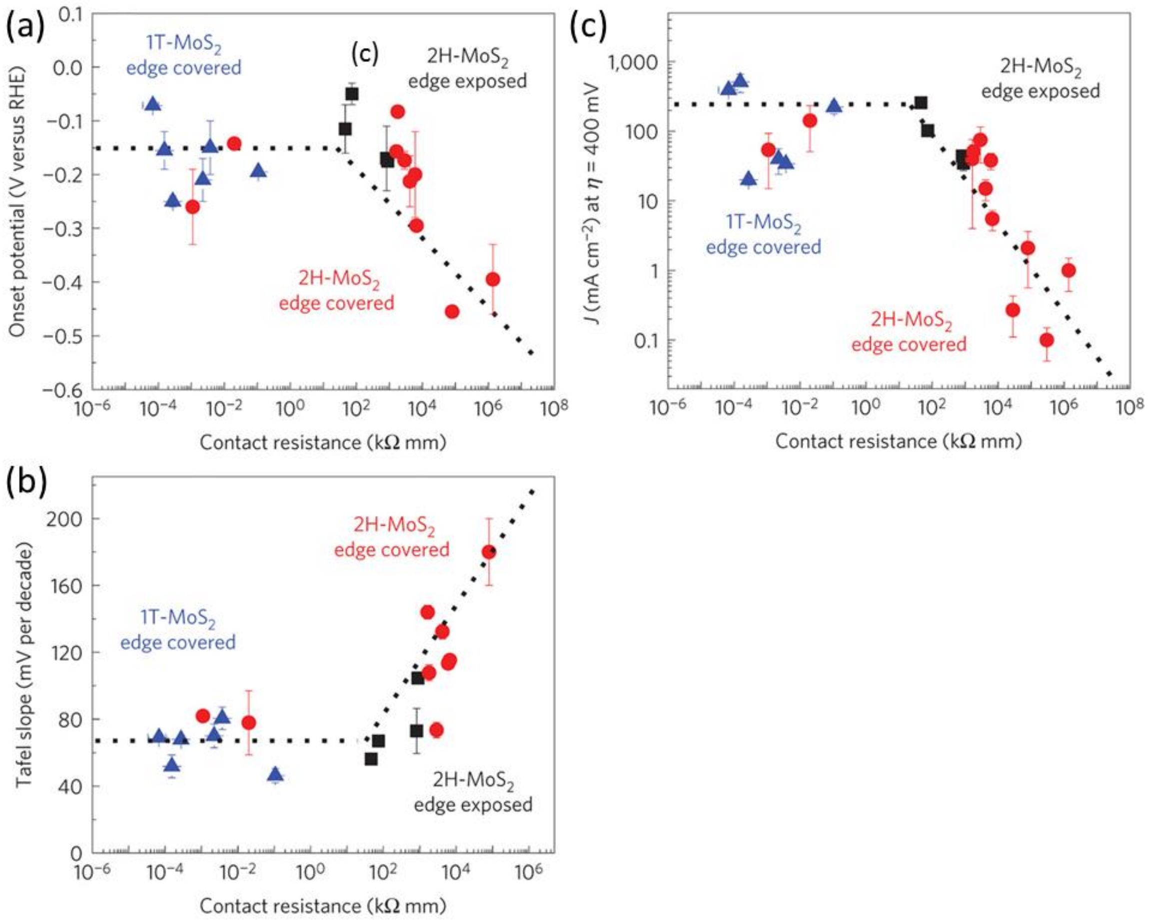

Figure 4-3 Variation of the onset potential **(a)**, Tafel slope values **(b)** and current density **(c)** measured at η = 400 mV with the contact resistance (R_c). The HER activity of the MoS_2 electrodes is progressively enhanced as the contact resistance decreases. For Rc < 10 kΩ mm, the MoS_2 activity stabilizes and current density of >100 mA cm^{-2} at η = 400 mV can be obtained from the MoS_2 basal planes. No significant differences between edge-exposed and edge-covered devices have been observed from the samples, suggesting that both the surface and the edges of the MoS_2 crystals are active.

with the hydrogen desorption reaction: H_{ads}+ H_3O^++ e^-→ H_2+ H_2O as the limiting step. [21,139–141] Our HER measurements on single MoS_2 nanosheets demonstrate that the mechanism for hydrogen evolution is markedly influenced by the efficiency of electron injection from the substrate to the catalyst and its transport to the active site. Tafel slopes of 120 mV per decade correspond to a mechanism where the hydrogen adsorption (Volmer reaction) is the limiting reaction. This is the case when the energy of hydrogen adsorption is high, making the process inefficient. This is expected here for the high contact resistance values because hydrogen adsorption cannot be favorable in the absence of electrons at the active sites owing to the poor electrical conductance of the catalyst (**Figure 4-3b**). On the other hand, improved electrical coupling enables the hydrogen to adsorb easily on MoS_2 and the reaction process through the Volmer–Heyrovsky mechanism, as observed in the present study and for metallic 1T-phase MoS_2 or MoS_2 grown on conducting reduced graphene oxide.[21,139–141]

The basal plane activity of 2H-phase MoS_2 observed in our work is in contrast with the literature.[38,132,139] The activity of 2H-phase MoS_2 basal planes is expected to be significantly lower than edges owing to the lower energy of hydrogen adsorption ($\Delta G_H *$) at the edge sites. To confirm the 2H-phase basal plane activity, we examined the HER activity from single-layer MoS_2 nanosheets on glassy carbon with contact resistance <100 kΩ mm. We found that the basal planes are indeed active towards the evolution of hydrogen, with an exchange current density of 7–16 μA cm^{-2} and a TOF at 0 V of 0.019–0.046 s^{-1}, which is comparable with the previous measurements from MoS_2 nanoclusters grown on gold. We attribute the catalytic activity of CVD MoS_2 nanosheets to sulfur vacancies. In a recent contribution, the Zheng and Norskov groups have shown that basal planes of 2H-phase MoS_2 can be activated by increasing the number of single S vacancies and the application of tensile strain on the nanosheets.[23] Defect densities as low as ~3% were predicted to lower $\Delta G_H *$ from 2 eV down to 0.2 eV. In the absence of strain, thermo-neutral H adsorption on the surface of 2H-phase MoS_2would require a density of S vacancies of ~14% (Ref. 23). Defects in CVD-grown MoS_2 have been reported by several groups,[157–159] and are known to induce pronounced modifications of the electronic and optoelectronic properties. Direct observations of these defects can be achieved through high-angle annular dark-field scanning electron microscopy (HAADF-STEM) owing to the contrast obtained by the presence and the nature of the atoms under the electron beam as shown in **Figure 4-4a,b** (Ref. [158,159]). STEM observations of the MoS_2 nanosheets reveal that defects are naturally present in the samples. Several types of defects have already been reported—such as single S vacancies, double S vacancies, Mo vacancies and Mo–S_x vacancies or antisite defects—and depend strongly on the synthesis methods[158,159]. Careful analysis of the MoS_2 basal plane (>500 nm^2) reveals that the large majority of the defects consist of single S vacancies with a density of the defects of up to ~9% (**Figure 4-4c**), which suggests that the basal plane may be activated by the presence of S vacancies. Assuming a density of defects of 9%, the TOF at 0 V from single-layer MoS_2 reaches 0.2–0.5 s^{-1}, in good agreement with the values reported by Li *et. al.*: 0.1–0.15 s^{-1}(Ref. 23).

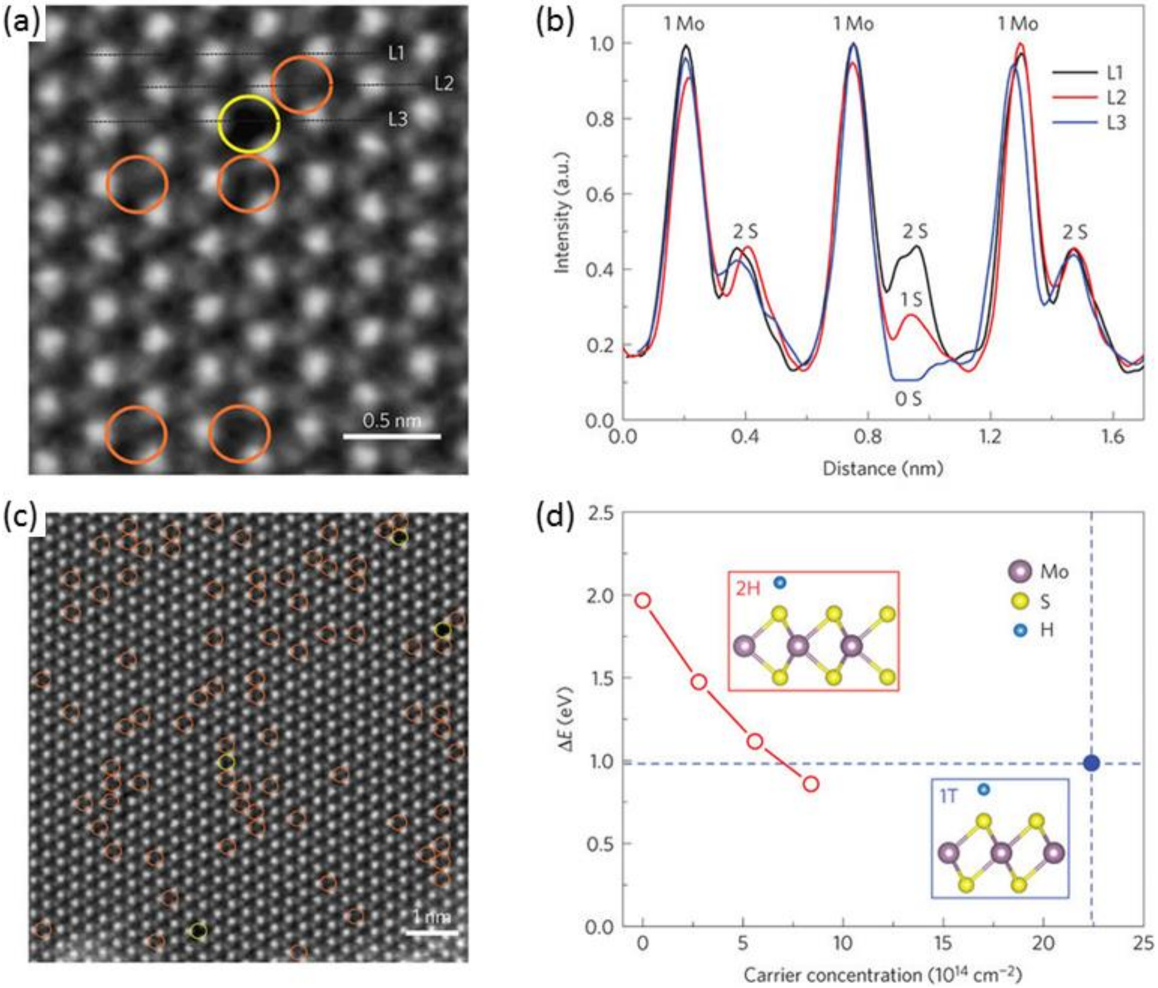

Figure 4-4 (a) STEM image of a single-layer CVD-grown MoS$_2$ nanosheet showing different types of defects: single sulfur vacancy (orange circles) and double sulfur vacancy (yellow circles). (**b)** Intensity profiles along lines L1–L3. Higher contrast is obtained from the Mo atoms compared to one sulfur atom (∼30% of the Mo intensity) and two sulfur atoms (∼45% of the Mo intensity). In absence of sulfur atoms (L3), the intensity decreases to <10%. **(c)**, STEM image of a large-area single-layer MoS$_2$nanosheet. The vast majority of the defects are formed by single sulfur vacancies. **(d)** The differential hydrogen adsorption energy (ΔE) in 2H-phase MoS$_2$ decreases significantly with an increased carrier concentration. When the carrier concentration approaches 7×10^{14} cm^{-2}, ΔE in 2H-phase MoS$_2$ is close to that in the 1T phase.

of MoS_2, probably located at the sulfur vacancies.

Dopants play two important roles in the HER. First, excess electrons lower the Schottky barrier at the contacts so that charge transfer kinetics between the conducting substrate and the MoS_2 nanosheets is substantially improved. This strategy has been widely used in the semiconductor industry to produce ohmic contacts for state-of-the-art electronics. Second, the presence of additional electrons in the MoS_2 lattice significantly decreases the energy of hydrogen adsorption, the first step in the HER, as shown by our density functional theory (DFT) calculations in **Figure 4-4d**. Sulfur vacancies in MoS_2 act as n-type dopants, increasing the density of states at the Fermi level. **Figure 4-4d** shows the variation of the energy of hydrogen adsorption (ΔE) on the 2H phase of the MoS_2 basal plane at doping carrier concentrations of 0, 2.8×10^{14} , 5.6×10^{14} and 8.4×10^{14} cm^{-2} and compared to the 1T phase. It can be seen that ΔE decreases quasi-linearly with the carrier (electron) concentration, suggesting that the ability for the 2H-phase basal planes to adsorb hydrogen improves for a higher concentration of dopants. Using a linear interpolation in **Figure 4-4d**, we estimate that ΔE for 2H-phase MoS_2 becomes lower than in the case of 1T-phase MoS_2 when the carrier concentration reaches 7.3×10^{14} cm^{-2}, consistent with carrier concentrations calculated for 9% S vacancies

4.4 Conclusion

Our work provides new insights into the role of electrical coupling between single-layer MoS_2 nanosheet catalysts and the substrate on the HER catalytic activity. The results show that the basal plane of the 2H-phase MoS_2, previously thought to be catalytically inactive, can exhibit excellent catalytic activity. That is, the basal plane of the MoS_2 surface contains active sites in the form of S vacancies but is rendered inactive for the HER because of the high contact resistance between the catalyst and the support. Our results show that lowering the contact resistance to facilitate charge injection from the substrate to the catalysts leads to realization of the intrinsic catalytic properties of the 2H basal plane. High contact resistance acts as a severe choke for electron injection to active sites, which limits catalytic activity, especially in the case of the 2H basal plane. For non-metal catalysts, contact resistance is an important variable because of the formation of non-ohmic contacts, which has been widely overlooked until now. Numerous studies have reported the catalytic performance of a wide range of MoS_2 catalysts, but very few explicitly mention the resistance between the catalyst and support. The contact resistance is an essential parameter that must be known to compare the relative performance of different types of MoS_2 catalysts for the HER. We believe these results will provide new directions for the design of large-area electrodes with low contact resistance that could ultimately exploit the full potential of MoS_2nanosheets for the evolution of hydrogen.

Chapter 5 Activating the 2D TMD family nanosheet catalysts by introducing Janus asymmetry

Synopsis

Significant efforts have been made in improving the hydrogen evolution reaction (HER) catalytic activity in transition metal dichalcogenides (TMDs), which are promising non-precious catalysts. However, previous attempts have exploited possible solutions to activate the inert basal plane, with little improvement. Among them, the most successful modification requires a careful manipulation of vacancy concentration and strain simultaneously. To fully realize the promise of TMD catalysts for HER in an easier and more effective way, a new means in tuning the HER catalytic activity is needed. Herein, we propose exploiting the inherent structural asymmetry in the recently synthesized family of Janus TMDs as a new means to stimulate HER activity. We report a density functional theory (DFT) study of various Janus TMD monolayers as HER catalysts, and identify the WSSe system as a promising candidate, where the basal plane can be activated without large applied tensile strains and in the absence of significant density of vacancies. We predict that it is possible to realize a strain-free Janus TMD-based catalyst that can readily provide promising intrinsic HER catalytic performance. The calculated density of states and electronic structures reveal that the introduction of in-gap states and a shift in the Fermi level in hydrogen adsorbed systems due to Janus asymmetry is the origin of enhanced HER activity. Our results should pave the way to design high-performance and easy-accessible TMD-based HER catalysts.

5.1 Introduction

Hydrogen is an increasingly important source of renewable energy, as global population and fossil fuel consumption continue to rise.[34–37] To maximize hydrogen production efficiency, alloy or noble metal catalysts such as platinum (Pt) are commonly used to facilitate the hydrogen evolution reaction (HER), by lowering overpotentials and accelerating reaction rates. In this context, it is pivotal to identify a low-cost and earth-abundant catalyst that can achieve performance comparable to that of Pt.[11–14,35] Among potential materials considered so far, the family of 2D TMDs has been extensively studied as a promising alternative catalyst for HER due to its unique crystal structures and electronic properties.[6,7,21–23] The overall activity of 2H-phase TMD catalyst mainly originates from the active edge sites rather than the inert basal plane. [38,132] Therefore, efforts have been made either to maximally expose edge sites using various nanostructures such as mesoporous films, nanoparticles, defect rich films, and vertical nanoflakes,[139,141,160,161] or to improve the intrinsic catalytic activity of edge sites using chemical doping, enhanced defect density, and enhanced coupling between substrates and monolayers.[21,22,133,142] However, the overall catalytic performance of TMD-based catalysts is limited by the relatively small fraction of edge sites compared to that of basal plane bulk sites. The key challenge is activating the TMD basal plane by increasing the number and catalytic activity of basal plane sites. Phase engineering has enabled enhanced electrocatalytic activity via a switch from the semiconducting 2H phase to the metallic 1T phase. [21,141] Without the introduction of a metastable 1T phase, Li et al. reported the first viable experimental method to activate the basal plane of 2H-phase MoS_2 by creating S-vacancies and applying tensile strains.[23] Specifically, using chemical vapor deposition (CVD) on a substrate with Au nanocones, capillarity-force induced strains were used to tune the hydrogen adsorption free energy (ΔG_H) to the optimum value in 2H-phase MoS_2 samples with S vacancies ranging from 9-19%. The strained 2H-phase MoS_2 monolayers with S vacancies achieved a similar catalytic activity (0.08 eV) to that of MoS_2 2H-phase edge sites (0.06 eV). However, this technique requires a precise control of both the strain and S vacancy concentration, which remains a significant experimental challenge.[23] To fully realize the potential of TMD catalysts, a new method that can easily and effectively tune the catalytic properties is needed.

Recently, strategies to synthesize a new family of so-called "Janus TMDs" have been reported by two independent groups.[43,44] MoSSe, one such Janus monolayer TMD, has been synthesized via two different synthetic pathways. Lu et al. reported a thermal selenization on a modified CVD-grown MoS_2 monolayer whose top-layer sulfur atoms are stripped off and replaced by H atoms, forming a structurally stable Janus MoSSe monolayer in which the Mo atoms are covalently bonded to underlying S and top layer Se atoms.[44] Another approach starts from the CVD as-grown $MoSe_2$ monolayers on a SiO_2/Si substrate, followed by a sulfurization of the top layer Se in a controlled substitutional reaction with vaporized sulfur.[43] Unlike the randomly alloyed MoSSe, both methods result in highly asymmetric Janus monolayers and provide a structure with an intrinsic strain and electric field within the monolayer, enabling an alternative way to tune the HER activity in TMD catalysts.[162]

Here, we report a theoretical study of Janus TMDs as catalysts for the HER. We computationally screened a set of possible Janus TMD structures to determine their hydrogen adsorption free energy (ΔG_H) and catalytic properties and identified WSSe with Se vacancies as a promising strain-free catalyst for the HER. We found that the HER activity of strain-free WSSe is similar to or better than that of current TMD-based catalysts, and does not require precise control of vacancy concentration or applied strain. We further investigated the origin of this enhanced HER activity by studying the electronic structure of Janus TMD monolayers.

5.2 Method

All our calculations were performed using the Vienna ab initio simulation package (VASP)[79] with the projector augmented wave (PAW)[80,163] pseudopotentials for core-electrons and the Perdew−Burke-Ernzerhof (PBE)[81] form of the generalized gradient approximation (GGA) for the exchange-correlation functional. A cutoff energy of 520 eV was applied for the plane wave expansion of valence electron wavefunctions. The unit cell structures of Janus monolayer TMDs were relaxed with a Γ-centered Monkhorst-Pack *k*-point mesh of $12\times12\times 1$ in the first Brillouin zone, while the total energy convergence was set to below 10^{-8} eV.[164] To avoid interactions between adjacent periodic images of the monolayers, we inserted a vacuum region of 16 Å along the plane normal direction. The atomic positions of all structures were optimized until all components of the forces on each atom are less than 0.01 eV/Å. To correctly optimize the chemisorption energies as well as van der Waals interactions, we used the Bayesian error estimation exchange-correlation functional with van der Waals interactions (BEEF-vdW)[165] as implemented in VASP. All other parameters remain the same as previous configurations in ion relaxations. We denote the Janus TMDs as MXY, where the M stands for a transition metal, and X and Y stand for two different chalcogen atoms, respectively. To simulate the effect of defects on the HER catalytic activity in Janus TMD (MXY) monolayers, we constructed 3×3×1 and 4×4×1 supercells with X- and Y-vacancies with a 4×4×1 and 3×3×1 *k*-point mesh, respectively. Our calculations indicate that these two types of single vacancies are energetically favorable sites for H adsorption.

In order to characterize the HER catalytic activity of Janus TMDs, we calculated the hydrogen adsorption free energy (ΔG_H).[37,166,167] The optimal value of ΔG_H is ~0 eV, where hydrogen is bonded neither too strongly ($\Delta G_H < 0$) to detach from the catalyst surface, nor too weakly ($\Delta G_H > 0$) to participate in subsequent reactions. ΔG_H is given by

$$\Delta G_H = \Delta E_H + \Delta E_{ZPE} - T\Delta S \qquad (5\text{-}1)$$

where ΔE_H, ΔE_{ZPE}, and $T\Delta S$ are the differential hydrogen adsorption energy, difference in zero-point energy between the adsorbed hydrogen and molecular hydrogen in the gas phase, and the entropy difference between adsorbed H and H_2 in the gas phase, respectively. Eq. (4-1) is composed of three parts. First, the differential hydrogen adsorption energy is calculated as

$$\Delta E_H = E_{\mathrm{Janus+H}} - E_{\mathrm{Janus}} - \frac{1}{2} E_{H_2} \qquad (5\text{-}2)$$

where $E_{\mathrm{Janus+H}}$, E_{Janus}, and E_{H_2} represent the total energy of a Janus TMD with one adsorbed H atom on the surface, the total energy of the Janus TMD, and the energy of a H_2 molecule, respectively. The second part is the difference in zero-point energy between the adsorbed and gas phase hydrogen, which can be calculated from the vibrational frequencies of the H atom at 0 K. Finally, the configurational entropy difference is calculated at 300 K between the adsorbed H and H_2 in gas phase. In our calculations, the configurational entropy of the adsorbed H state is small and can be neglected. Therefore, we assume $\Delta S = -{}^1\!/_2\,\Delta S(H_2) = -65.34$ J·mol^{-1}K^{-1} using the H_2 molecule entropy in gas phase at the standard condition (1 bar, 300K, pH =0).

5.3 **Results**

5.3.1 Structure models of Janus TMDs

Traditional TMD monolayers are typically represented as MX2, where the transition metal M(Mo, W) layer is sandwiched between two identical chalcogen atom layers X(S, Se, or Te).[20,168] By changing one layer of chalcogen atoms to a different one, the highly asymmetric Janus MXY is constructed. This substitutional method in constructing the Janus structure is consistent with the mechanism of recently reported experimental methods.[43,44] So far only one representative Janus TMD, MoSSe, has been reported; other Janus systems can potentially be synthesized using similar approaches. Therefore, to guide experimental efforts, we first performed a systematic DFT study to predict the structural properties of Janus TMDs, and summarized them in **Table 5-1**. In general, the value of the lattice parameter a in Janus TMD structures (XMY) lies between the ones of its parent structures, namely MX2 and MY2. Our predicted a of MoSSe is 3.251 Å, which is in good agreement with experimental and theoretical values.[44,169] The MX/MY bond length, as well as the thickness of the Janus monolayer, increases in Janus TMDs with heavier metal elements. However, the lattice constant of Janus monolayers with the same chalcogen elements remains almost the same regardless of the metal element, indicating chalcogen atoms play a critical role in determining the structural properties. By comparing the difference between lattice constants of the Janus TMD and its parent structures, we see that effective compressive and tensile strains occur simultaneously on the lighter and the heavier chalcogen sides, respectively.

Table 5-1 Structural properties of Janus TMDs.

	a using GGA (Å)	*a* using BEEF (Å)	Experiment value (Å)	MX bond length (Å)	MY bond length (Å)	Thickness (Å)
MoSSe	3.246	3.251	3.22[44],3.263[43]	2.418	2.536	3.231
MoSTe	3.359	3.364	N/A	2.435	2.724	3.379
MoSeTe	3.437	3.432	N/A	2.558	2.725	3.489
WSSe	3.246	3.248	N/A	2.421	2.538	3.242
WSTe	3.354	3.359	N/A	2.437	2.723	3.386
WSeTe	3.432	3.427	N/A	2.558	2.724	3.494

5.3.2 HER with defects and intrinsic strain

Defects and applied strain play an important role in the HER activity of TMD monolayers. Previous studies showed that the process of HER requires specific modifications of the TMD basal plane, which can be realized by applying a large amount of tensile strain to 1T-phase WS_2,[22] or by creating and straining S-vacancies simultaneously in the 2H-phase MoS_2.[23] For example, in order to reach $\Delta G_H \approx 0$ eV, a condition of 3.12% S-vacancy and 8% strain, or equivalently 12.5% S-vacancy and 1% strain, is required in 2H-phase MoS_2.[23]

Such large strain and defect concentrations are indispensable in activating the basal plane of 2H-phase MoS_2 because either mechanism alone is insufficient to adequately modify the total energy of the system. However, it is difficult to experimentally realize such extreme strain and defect concentrations. Our goal is to identify an optimal Janus structure that has the highest HER catalytic activity and requires the least amount of applied strain, i.e. an ideal defect density close to the intrinsic defect concentration in as-CVD grown samples, and a strain close to the intrinsic strain in the Janus TMD.

Before considering the HER activity of Janus TMDs, we first investigate the nature of defect structures. Both X and Y vacancies are energetically favorable at low concentrations (few percent). In our supercells, the defect concentration (%X/Y) is defined as the percentage of removed chalcogen atoms (# of X/Y vacancy / # of total X/Y atoms). Our supercells consist of either 9 M atoms and 18 X/Y atoms or 16 M atoms and 32 X/Y atoms on the surfaces. Therefore, an increment in the defect concentration of 2.43% can be achieved by varying the two types of supercells. In experiment, the defect concentration in as-grown CVD Janus structures is between 3.8%[44] and 5.5 %[43]. Likewise, in the basal plane of 2H MoS_2, the intrinsic carrier concentration is around 2.8×10^{14} cm^{-2}, or equivalently 4.9%.[22] Therefore, we simulate a reasonably low defect concentration of 3.12%. With an increased defect concentration, the formation of chalcogen vacancies becomes energetically less favorable due to the screening effect between vacancies. For the range of vacancy concentrations we considered, no noticeable structural disruption was observed in the relaxed defective Janus TMDs. Notably, the introduction of defects lowers ΔG_H. For example, ΔG_H reduces from ~1.82 eV in pristine WSSe Janus TMD to -32 meV in Janus

WSSe with 3.12% S-vacancy and to -15 meV with 3.12% Se-vacancy. This is in good agreement with previously reported trends in 2H-MoS_2, where the introduction of S-vacancies reduces ΔG_H from 2 eV to 0.18 eV.[23] The introduced chalcogen vacancy in MSSe provides a better HER catalytic activity than that in MSTe and MSeTe due to the more optimal amount of intrinsic lattice strain. Different values of ΔG_H have been observed in various strain-free Janus TMDs, and we plot ΔG_H for the most promising one, namely WSSe, and a less preferred one, MoSTe, in **Figure 5-1**c.

Next, we investigate the effect of strain on ΔG_H in Janus TMDs with preferred Se-vacancies. For any fixed vacancy concentration, a larger tensile strain leads to a more negative ΔG_H, similar to the effect previously reported for 2H basal planes[22] and edge sites.[132,142] (**Figure 5-1**c) For the MoSTe system, both S- and Te-vacancies respond similarly to applied strain. In a strain-free state, ΔG_H approaches –100 meV, while a 2% compressive strain results in better performance, with ΔG_H around -50-70 meV. Moreover, in order to meet our goal, we set a catalytic window of $\pm$ 25 meV as shown in the green region in **Figure 5-1**. It is worth noting that the ΔG_H for Se-vacancy in the WSSe Janus structure can achieve a value (15 meV) that is very close to thermal neutrality, which is much better than that at 2H edge sites (60 meV[132,142]) or activated basal plane sites[23]. Compared to previously reported conventional TMD systems that require significant modification with either large strain (8%) or large vacancy concentration (12.5%), or both[23], our Janus WSSe system can achieve a similar or even better catalytic activity without such extreme conditions. Moreover, in a $\pm$ 0.5% strain range our WSSe Janus

TMDs displayed a robustly high catalytic activity on both sides with low defect concentration, which enables a strain-free as-grown catalyst system.

We attribute this improved HER catalytic activity to the intrinsic lattice strain within the Janus structure. The MSSe Janus structure has an intrinsic strain of ~4% that optimally alters the strain energy level and facilitates the H adsorption process, which is equivalent to applying external uniaxial strains. In MSTe and MSeTe Janus TMDs, a larger intrinsic strain (7-11%) results in a more negative ΔG_H and hence a very strong binding of H onto the Janus surface. Therefore, in this work only the MSSe Janus structures are discussed.

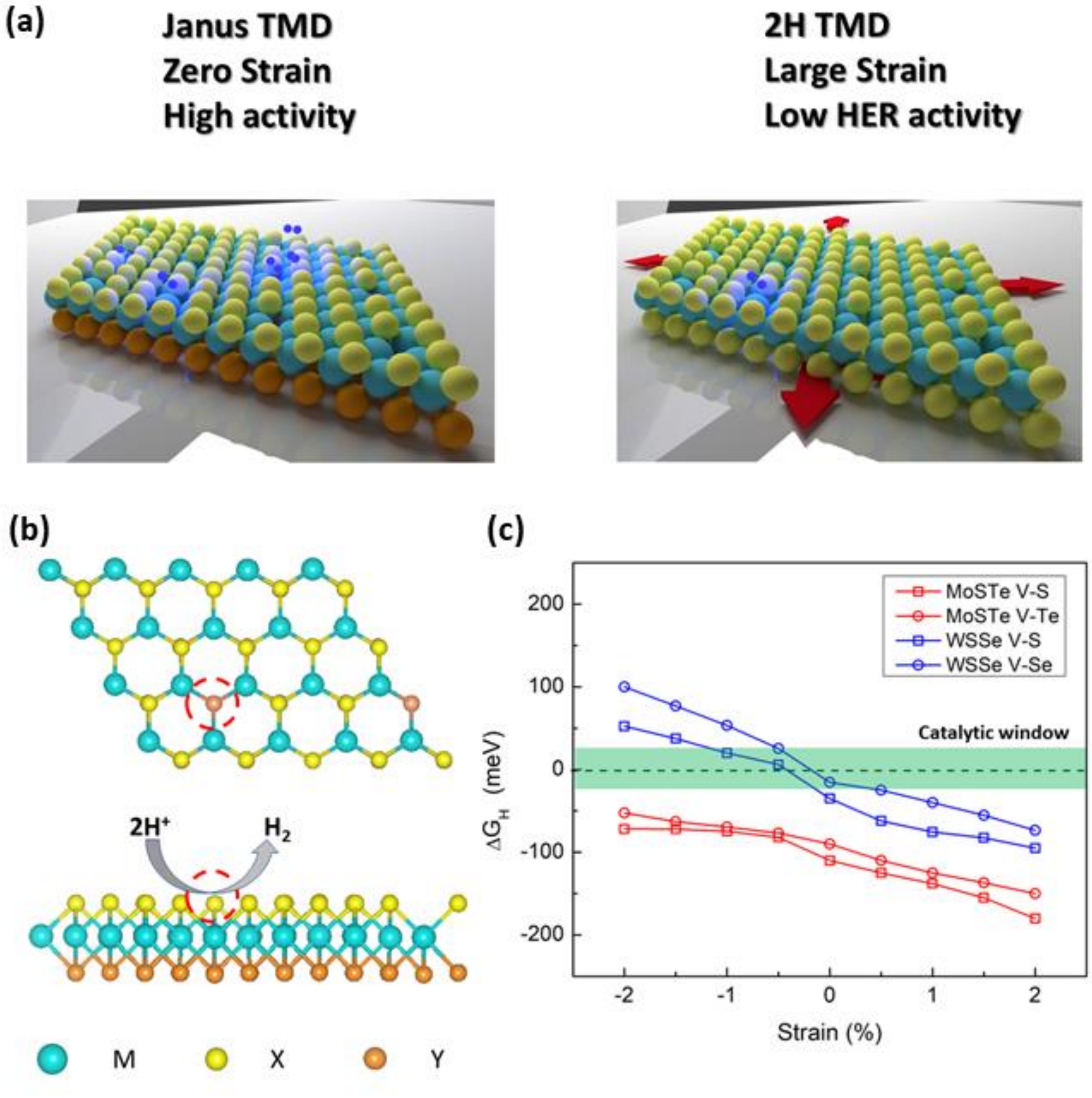

Figure 5-1 (a) Schematics of the strain-free HER reaction on Janus TMDs. **(b)** The surface vacancy structure of Janus TMDs showing X and Y vacancies. **(c)** ΔG_H versus applied strain for different Janus TMDs with vacancies. The catalytic window is highlighted in green.

5.3.3 Electronic structure of Janus TMD monolayers

To gain deeper insight into H adsorption on various surfaces, we performed electronic structure calculations. **Figure 5-2** depicts the computed total density of states (TDOS) and projected density of states (PDOS) of pristine and defective Janus TMDs, showing the change in electronic structure during H adsorption in the vicinity of defects. As noted previously, we focus on MSSe Janus structures due to their preferred intrinsic strains. First, by comparing the first two rows in **Figure 5-2**, we conclude that new gap states consisting mostly of metal *d* orbitals appear after the introduction of vacancies. The sharper in-gap peak in the WSSe Janus TMDs suggests a higher density of states than that in the MoSSe Janus TMDs. Second, the Fermi level shifts up with the H adsorption. In pristine MoSSe the H adatom shifts the Fermi level by 1.32 eV, while in pristine WSSe the H adatom shifts the Fermi level by 0.88 eV. In both cases the H 1*s* orbital overlaps with the TDOS immediately below the conduction band minimum (CBM), indicating an unstable adsorption state in pristine Janus TMDs because of the lack of available states on the Janus TMD surface. Meanwhile, the introduced states associated with the formation of the chalcogen vacancies provide a possibility for hybridization between the H 1*s* orbital and metal 3*d* (4*d*) orbitals. The adsorption of H on WSSe with Se-vacancies shifts the Fermi level by 0.42 eV, aligning it with the position of degenerate d_{xz} and d_{yz} orbitals. The in-gap peak is partially filled at the Fermi level, resulting in an increased number of states at the Fermi level. More importantly, the H *1s* orbital hybridizes with the Janus WSSe Se-

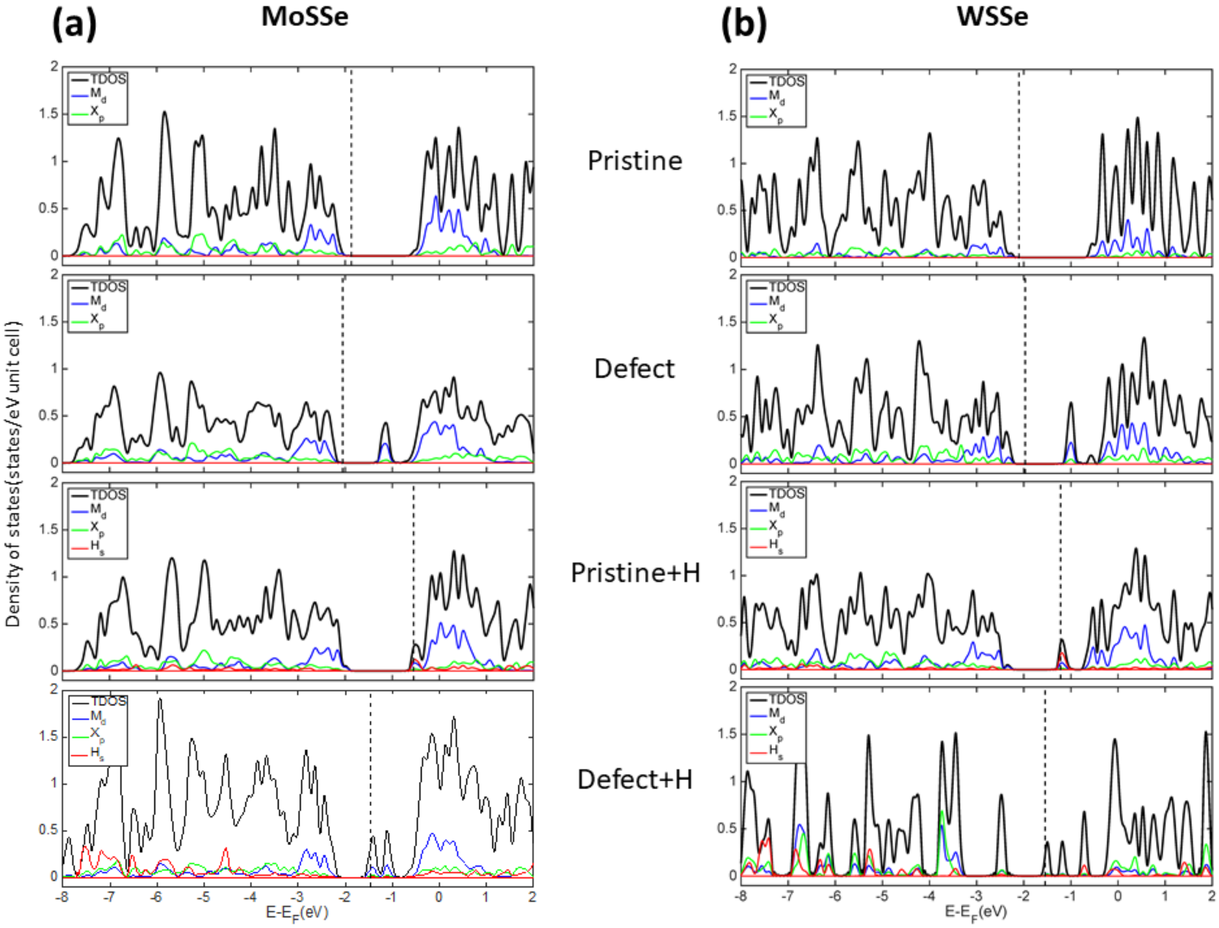

Figure 5-2 Total DOS and projected density of states (PDOS) of two representative Janus TMDs, **(a)** MoSSe and **(b)** WSSe. The four rows indicate pristine and defective structures without a hydrogen adatom, and pristine and defective structures with a hydrogen adatom, respectively. New states associated with the formation of vacancies are located within the band gap.

vacancies both below and above the Fermi level, forming a stable bonding-antibonding adsorption state. Therefore, the WSSe with vacancies is preferred for H adsorption.

In order to further elucidate the nature of the promising HER catalytic activity at vacancy sites, we calculated the band structure in WSSe Janus monolayers. **Figure 5-3** shows the band structures of pristine WSSe, WSSe with Se-vacancy, and WSSe with Se-vacancy and adsorbed H adatom. When Se-vacancies are introduced, three new bands (**Figure 5-3**b, blue curves) composed of d_{z^2}, d_{xz}, and d_{yz} states appear in the gap near the Fermi level. These new bands, which are freed up due to the breaking of W-Se/W-S bonds, provide empty orbitals for H adsorption. The d_{z^2} orbital is located slightly above the valence band maximum (VBM) in pristine WSSe, while two degenerate d_{xz}, d_{yz} orbitals are located above the Fermi level. When H is adsorbed, the d_{z^2} orbital shifts up to the Fermi level, and the H *1s* electron partially fills this state, forming a stable H adsorption for the Volmer process. We attribute this enhanced HER catalytic activity to the change of the crystal field due to the Janus asymmetry. **Figure 5-4** schematically shows the change in crystal field, where the structural imbalance in MXY monolayers breaks the reflection symmetry along the out-

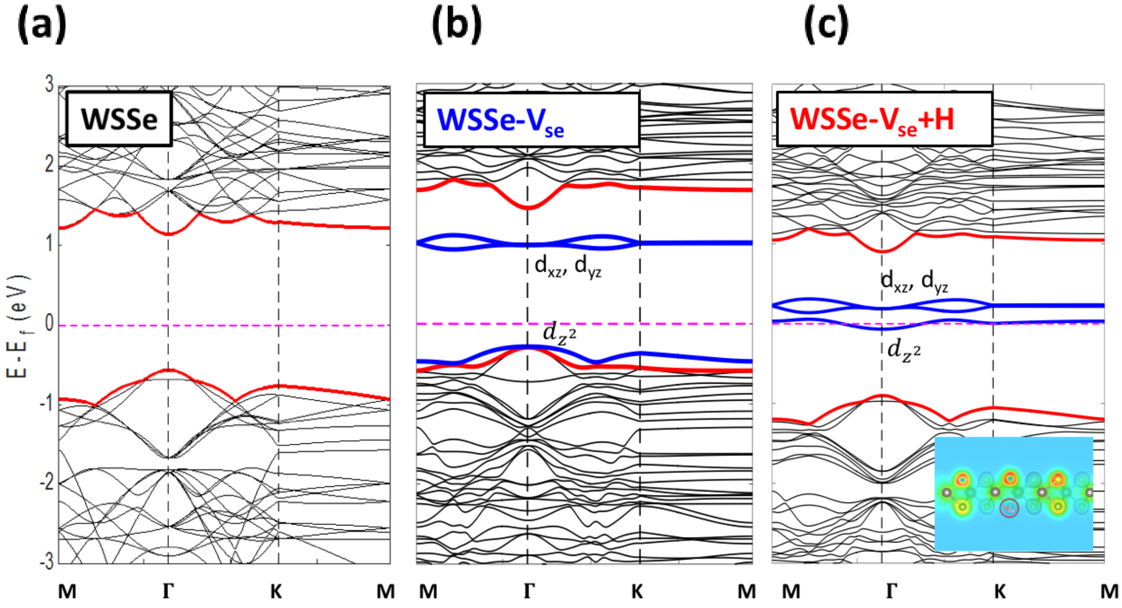

Figure 5-3 Effects of Se vacancy on the electronic structure of Janus WSSe. **(a)** Band structure of pristine WSSe. **(b)** Band structure with the introduction of the Se vacancy. Three new bands (highlighted in blue) appear in the gap. **(c)** Band structure after H adsorption. The states introduced hybridize with the H orbital near the Fermi level. The inset illustrates the charge density difference near the vacancy.

of-plane direction. Moreover, the Jahn-Teller distortion of the crystal field increases the energy of orbitals with a z component, especially d_{z^2}, which pushes those bands closer to the Fermi level. The difference in electronegativities of X and Y atoms, together with the difference in thicknesses of Janus monolayers due to their different metal atoms, gives rise to different charge distributions and hence an intrinsic electric field along the vertical direction. We identify this intrinsic electric field as an alternative to the applied strain used to engineer ΔG_H in previous studies.[23] The WSSe Janus monolayer best exemplifies the modification to the band structure due to the intrinsic electric field inside the monolayer. These results provide a possible mechanism to explain the enhanced HER catalytic activity in Janus TMD monolayers.

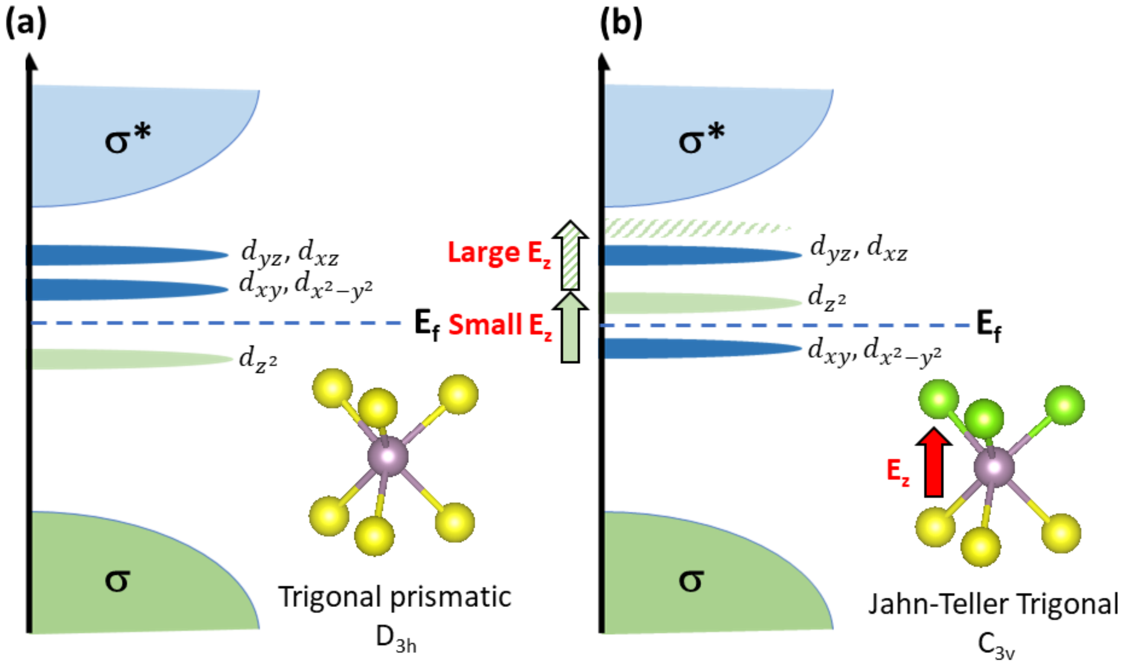

Figure 5-4 Schematic illustrations of the crystal field and band alignment of Janus TMDs. **(a)** Conventional 2H TMD with trigonal prismatic structure, and **(b)** Janus structure which breaks the mirror symmetry along the vertical direction.

5.3.4 HER

To evaluate the HER catalytic activity and compare with conventional HER catalysts, we calculated the polarization curve (*i* - E) of a representative WSSe Janus TMD with two types of vacancies within the catalytic window as shown in **Figure 5-5**. Two descriptors, namely the current density per geometry area at a certain potential, and the required potential to achieve a 10 mA cm^{-2} current density (E_0), have been adopted for quantifying the HER activity. We compared these results with other materials that catalyze the HER, based on activity per active site. Pt (1.5×10^{15} sites/cm^2) shows the highest current density for HER activity, while non-reactive Au shows almost zero HER activity in this electrocatalytic window. In between lies the pristine 2H-phase MoS_2 and Janus WSSe monolayers, where the order of HER activities of these TMDs are WSSe with Se-vacancy (-158 meV) > WSSe with S-vacancy (-174 meV) > pristine WSSe (-264 meV) > pristine WS_2/WSe_2. This trend holds across all Janus TMDs, showing that the presence of single S-, Se-, and Te-vacancies significantly improves the binding between H and Janus TMD monolayers, and hence changes the inert basal plane to be catalytically active for HER. It is worth noting that our systems are in a strain-free condition, which eliminates the complex control of vacancy concentration and strain in previous studies.[23]

To shed light on the catalytic activity of Janus TMDs, we have added our data to an updated volcano curve as shown in **Figure 5-5b**. The volcano plot indicates the exchange current density as a function of calculated Gibbs free energy of adsorbed H, where the peak of the volcano is the preferred catalytic region. The HER performance of our Janus WSSe system surpasses that of current MoS_2 TMD nanostructures and other metals. It suggests that Janus TMD systems with vacancies hold promise as a new type of HER catalyst.

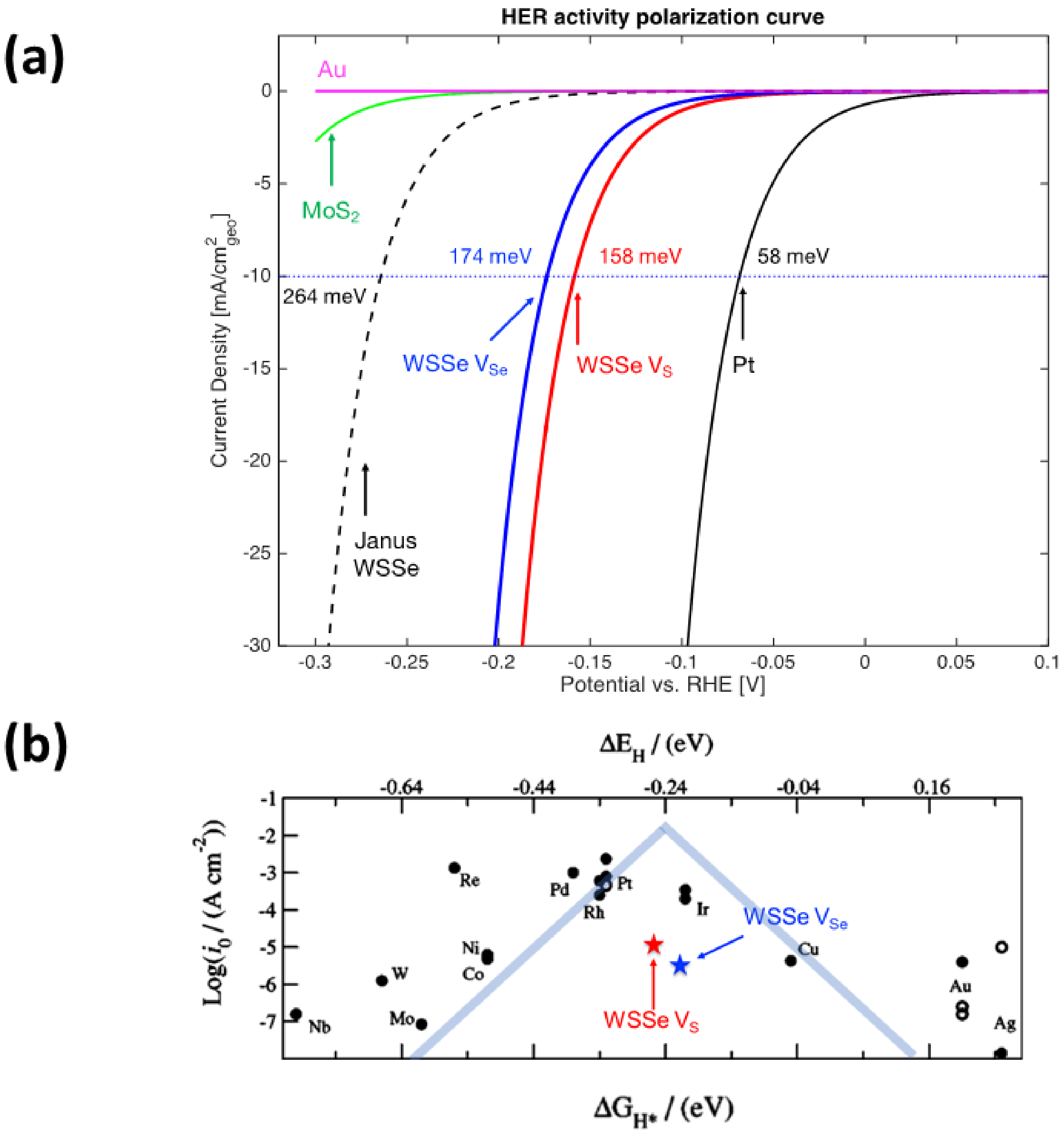

Figure 5-5 HER activity of the S and Se vacancy sites in Janus WSSe. **(a)** The predicted current density of Janus TMDs versus other HER catalysts. **(b)** The HER volcano curve including Janus WSSe.

5.4 **Conclusion**

In summary, we have theoretically predicted that 2D Janus TMD monolayers are promising catalysts for the HER using first-principles density functional theory calculations. Our results show the effect of intrinsic strain due to the Janus structure, and the role of vacancies in activating the inert basal plane. An optimal hydrogen adsorption free energy (ΔG_H) close to thermo neutrality has been discovered in the WSSe system, where high HER catalytic activity can be achieved in a strain-free condition with the presence of S/Se-vacancies at their intrinsic concentration. With the Janus asymmetry, WSSe monolayers with Se-vacancy can achieve a ΔG_H of -15 meV with 0% strain, which eliminates the need for complex strain-engineering techniques used in activating conventional 2H-phase TMD catalysts. Moreover, we attribute the enhanced HER catalytic activity to the introduction of Janus asymmetry that brings intrinsic strain and internal electric field. Our results provide a new paradigm in tuning HER activity in TMD systems, and demonstrate a means of activating the basal plane without the need of complex materials design.

Chapter 6 Overview of multiscale modeling methods in understanding Mechano-Electro-Chemical coupling in 2D materials

Reprinted (adapted) with permission from H. Kumar, **D. Er**, L. Dong, J. Li, and V. B. Shenoy. *Elastic Deformations in 2D van der waals Heterostructures and their Impact on Optoelectronic Properties: Predictions from a Multiscale Computational Approach*. **Scientific Reports**, 5:10872 June 2015

6.1 Introduction

The size of 2D materials are typically between tens of nanometers to even hundreds of micrometers, where it is in between the mesoscale and nanoscale pictures. Challenge lies in given the properties of individual method form atomistic approaches (valid over 1-10 nm length scale), how can the overall electrical, mechanical, chemical properties of large 2D and 3D structures (span scales from 1 µm to 1 mm) be predicted including properties that are key to the success of energy applications. One approach to overcome the above difficulties is to employ a multiscale method using DFT informed parameters to compute key descriptor in larger scale models.

We have used the DFT method in many scenarios. In this multiscale method, starting with a set of non-empirical DFT calculations, we characterize the features required in larger scale modeling. The parameters such as energies of structures, strain response, electronic structure, and mechanical behavior in relative small length scale can be computed using first principles methods. We choose differential functionals and approximations according to the question itself. With the parameters, we plug them into a continuum model that can address questions in a much larger length scale. The advantage of this method is the ability to handle coupling between different physical, mechanical, chemical phenomena across length scale. For example, the strain dependence of electric coupling between stacked 2D layers become readily solved once the strain and structural alignment predicted from DFT is known.

Moreover, beyond a purely 2D monolayer picture, the assembly in the 3rd dimension, particularly the stacking of homogeneous and heterogeneous layers offers another rich line of investigation. This problem requires a larger length scale in the third dimension where only proper multiscale methods can capture the physics. In order to predict the stacking sequence, physical properties, and material response to applied strain/electrical/chemical potential fields, one has to evaluate the interlayer interactions/forces in the stacks with enough accuracy. Empirical pairwise potentials are often inadequate for this task, as they lack transferability and neglect essential many-body effects in such interactions. Recently developed nonlocal parameter-free functionals such as DFT-D2 offer a much higher accuracy approach to evaluating these interactions. [See **Appendix**] Use these functionals in our multiscale modeling will enable an efficient and accurate prediction of stacked 2D materials with unique properties.

6.2 General Framework of multiscale modeling

In this section, we develop a general framework to estimate the Mechano-Electro-Chemical coupling in 2D materials using a multiscale modeling approach. Our DFT informed multiscale approach involves the following steps as shown in **Figure 6-1**.

(1) Determine the DFT level properties of material, including the stability, interaction energy, elastic constants, electronic constants, defect formation energies, etc.

(2) Based on the above parameters, derive a continuum level description of interested properties using methods such as energy method, growth model with flux, and continuum mechanics.

(3) Verify the model with experimental values.

(4) Use the model to predict other multiscale properties of materials.

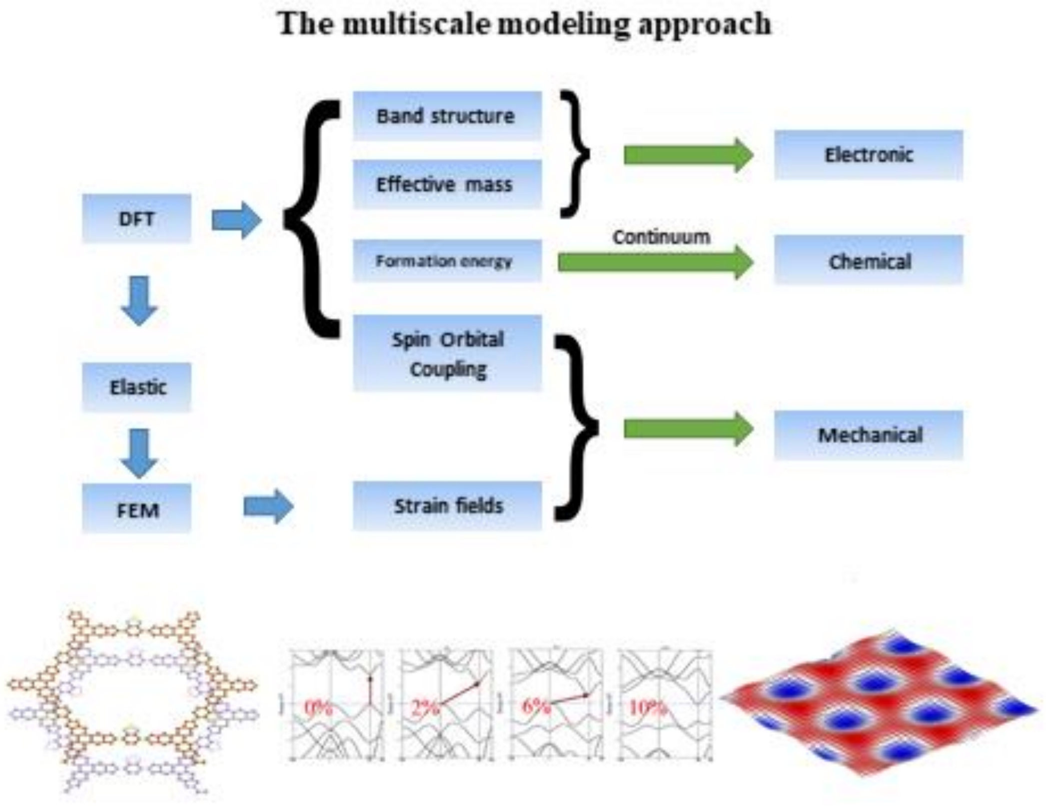

Figure 6-1 Multiscale approach to compute the Mechano-Electro-Chemical coupling in 2D materials. DFT simulations accurately predicts the basic material properties, providing parameters for later continuum level modeling. FEM and continuum mechanics methods are therefore connected with DFT material properties.

6.3 The first example: compute the elastic deformations in Moiré patterned 2D heterostructures

To validate our multiscale approach, we first compute the elastic deformation problem in a 2D heterostructure with arbitrary misorientation angles between layers. 2D materials such as graphene, h-BN, and TMDs have received renewed interest in stacked/heterostructure configurations. However, lattice mismatch and interactions between different layers can give rise to deformation, both in-plane and out-of-plane, that causes change in electronic properties. These deformations are not easy to simulate because current theoretical approaches such as DFT are limited in their predictive power due to the large mismatch between the length scales of deformations (10-100 nm). This problem is a rich avenue to verify our multiscale method since experimental data such as the morphology of Moiré pattern are widely available. Therefore, we estimate the deformations in heterostructure bilayers with arbitrary misorientation angle using a multiscale approach, i.e. continuum finite-deformation simulations informed by ab-initio calculations. To demonstrate the validity of our method, DFT-informed continuum models have been used to study a specific material system, namely graphene on h-BN, for which empirical potentials are available. The deformations predicted by our multiscale approach agrees excellently with the one from all-atom MD simulations.

6.3.1 Computational detail

Our DFT informed continuum approach involves the following steps (as described in **Figure 6-2**) for the case of monolayer of material A (in the present case, graphene) on top of a “substrate” B (in this case, h-BN).

(1) Determine the interaction energy of the unit cell of layer A as a function of its position relative to the unit cell of the substrate, layer B.

(2) Based on the above interaction energy, derive a continuum description of the spatial variation (on the scale of the Moiré unit cell) of the interactions energy between the layer A and the substrate by inverse Fourier transformation.

(3) Obtain in-plane and out-of-plane forces acting on layer A from the spatial variation of the interlayer interaction energy.

(4) Use the forces in a non-linear elastic plate model to predict in-plane and out-of-plane deformations in layer A.

Spatial variation of interaction energy of the unit cell of layer A as a function of position over the layer B unit cell can be written as (Step 1):

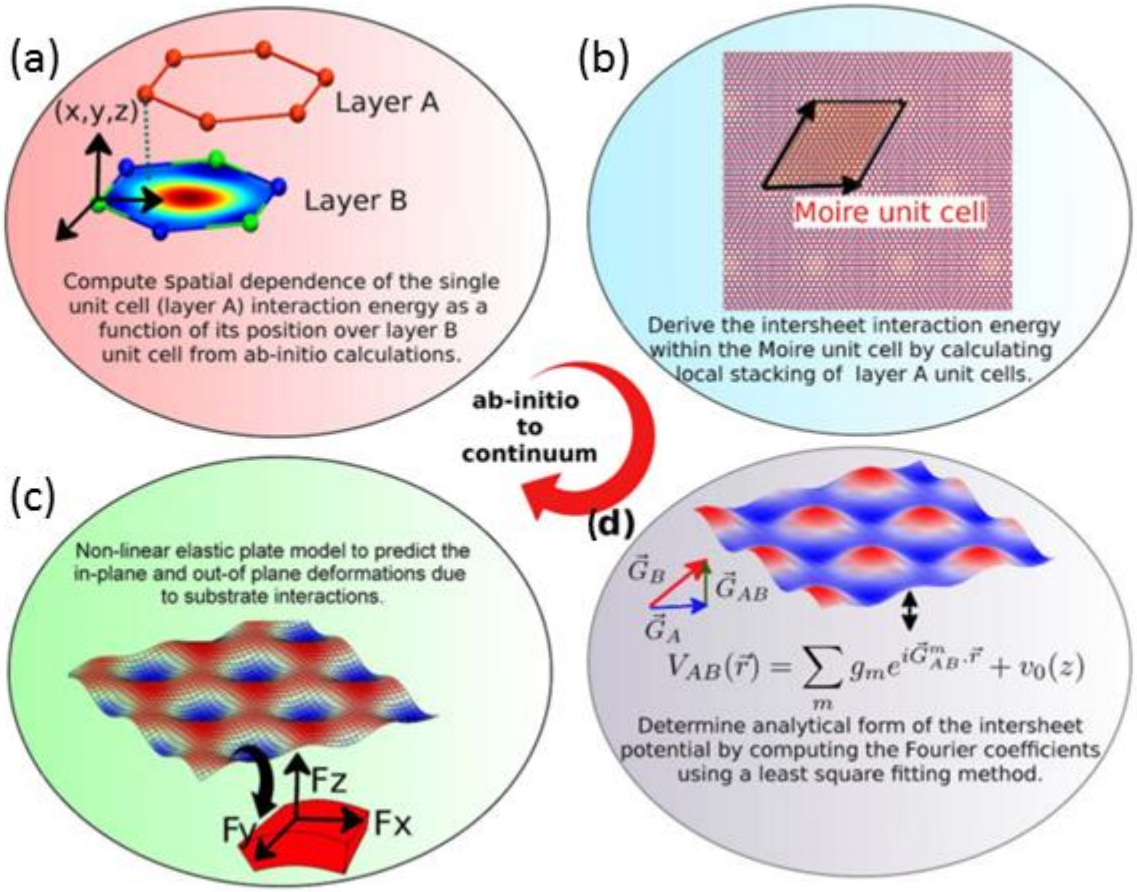

Figure 6-2 Illustration of the simulation steps. **(a)** Interaction energy of the layer A unit cell as a function of its position over the layer B unit cell computed from the ab-initio calculations. **(b)** Interaction energy of layer A within a Moiré unit cell is determined by calculating the local stacking configuration of each unit cells in layer A relative to layer B. **(c)** Numerical values of the energy (from b) are used to determine the Fourier coefficients using an inverse Fourier transform. **(d)** Interaction energy is used to compute the in- plane and out-of-plane forces and hence displacements fields in the bilayer using a large deformation elastic plate model.

$$V_B(x,y,z) = \sum_{m,n\neq 0} u_{mn}(z) e^{i\vec{G}_{Bmn}\cdot\vec{x}} + u_0(z) \tag{6-1}$$

where, $\vec{G}_{Bmn}$ are the 2-dimensional reciprocal lattice vectors for the B-lattice. Unknown Fourier coefficients u_{mn} and $u_0(z)$ can be computed by calculating the energy of bilayer unit cell in different stacking configurations using density functional theory. For a substrate with triangular lattice symmetry, it is sufficient to consider reciprocal lattice vectors only within the first Brillouin zone. Using this information, **Eq. (6-1)** can be written as (Step 1):

$$\begin{aligned} V_B(x,y,z) &= 2u_1(z)\cos(\phi(z) - G_1 y) \\ &\quad + 4u_1(z)\cos\left(\frac{G_1 y}{2} + \phi(z)\right)\cos\left(\frac{\sqrt{3}G_1 x}{2}\right) \\ &\quad + u_0(z) \end{aligned} \tag{6-2}$$

where $u_0(z)$ is the average energy of the unit cell, $u_1(z)$ is the magnitude of the energy modulations and $\phi(z)$ gives the energy difference between AB and BA stacked configurations and G_1 is the magnitude of the reciprocal vector for substrate primitive unit cell. For equilibrium separation z_0 = 3.4 Å, this gives $u_0(z)$ = –69.2 meV, $u_1(z)$ = 2.26 meV and φ = –50.4° according to DFT results.

Based on this functional form of the interaction energy of the primitive cells, spatial variation of the interaction energy of the two layers within a Moiré cell can be computed by calculating the local stacking of each unit cell in layer A relative to the unit cell in layer B. The spatial variation of the interaction energy between two layers (see **Figure 6-2**) V_{AB} can be written in terms of Moiré reciprocal lattice vectors $\vec{G}_{AB}^{mn}$ (Step 2)

$$V_{AB}(x,y,z) = \sum_{m,n} g_{mn}(z) e^{i\vec{G}_{AB}^{mn}\cdot\vec{x}} + u_0(z) \tag{6-3}$$

Next, we relate the reciprocal lattice vectors of the Moiré cell to the lattice mismatch and the relative rotation of the two layers. For the case of graphene on hBN (with the same lattice symmetry), the lattice mismatch is defined through the $\alpha_{\mathrm{BN}} = \alpha_{\mathrm{c}}$ (1+ δ) and lattice misorientation angle is denoted by θ. With symmetry at hand, we expand **Eq.(6-3)** around the equilibrium separation z_0 between the layers.

$$\begin{aligned} V_{AB}(x,y,z) = \sum_{m=0,5} [g_m(z_0) + g'_m(z_0)(z - z_0)] e^{i\vec{G}_m\cdot\vec{x}} \\ + u_0(z) + \frac{1}{2} u''_0(z_0)(z - z_0)^2 \end{aligned} \tag{6-4}$$

noting that the first derivative u'_0 is zero at z_0. Here, Fourier coefficient $g_m(z_0)$ is the magnitude of the energy modulation within Moiré unit cell, $g'_m(z_0)$ is the change in magnitude of energy modulation and $u''_0(z_0)$ acts as an effective "spring constant" between two layers. Derivatives of this energy give the components of the forces acting on the top layer due to the substrate (Step 3):

$$F_{A,B}^{x,y}(x,y,z) = -\sum_{m=0,5} [g_m(z_0) + g'_m(z_0)(z - z_0)] e^{i\vec{G}_m\cdot\vec{x}} \cdot iG_m^{x,y} \tag{6-5}$$

$$F_{A,B}^{z}(x,y,z) = -\sum_{m=0,5} g'_m(z_0) e^{i\vec{G}_m\cdot\vec{x}} - u''_0(z_0)(z - z_0) \tag{6-6}$$

And finally the deformation of the two sheets can be computed using the von-Karman non-linear plat theory,[170] because the length scales over which the magnitudes of the forces vary are large(~14 nm) compared to atomic scales. Then the out-of-plane deformation, w, is determined (Step 4):

$$\frac{Eh^3}{12(1-\sigma^2)}\Delta^2 w - h\frac{\partial}{\partial x_\beta}\left(\sigma_{\alpha\beta}\frac{\partial w}{\partial x_\alpha}\right) = F_{AB}^z, \frac{\partial \sigma_{\alpha\beta}}{\partial x_\beta} = F_{AB}^\alpha \quad (6\text{-}7)$$

where h is the thickness of the plate, α, β denote the in-plane and out-of-plane components. the Young's modulus E and thickness h of graphene are estimated by equating the effective 2D modulus Eh = Ep = 2000 eV/nm^2 and flexural rigidity to the bending modulus $\frac{Eh^3}{12(1-\sigma^2)}$ = 1eV. Then these parameters are adequate for FEM simulations.[171]

6.3.2 Comparison to experimental data

To demonstrate the validity of our multiscale method, we focus on the formation of Moiré pattern. Recent experiments have measured[172] the magnitudes of the out-of-plane displacements to be approximately ~0.3 Å, which is similar to the magnitude of the out-of-

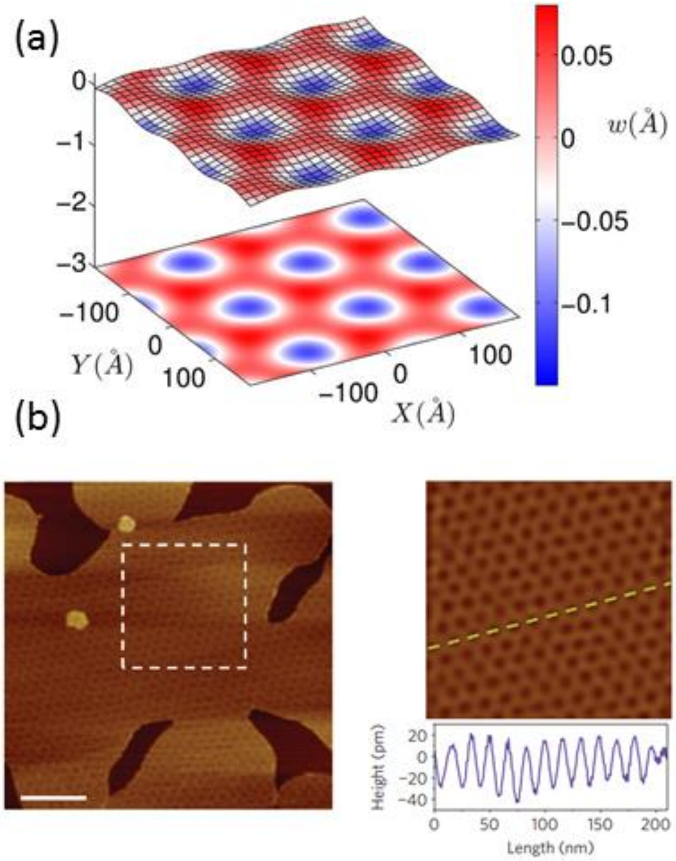

Figure 6-3 (a) Out-of-plane displacement (w) in the graphene monolayer due to interactions with the h-BN substrate for the perfectly aligned layers ($\theta = 0$) using our multiscale approach. We observe Moiré patterns with similar magnitudes as in experiments as shown in panel (b). **(b)** High-pass-filtered inverse fast Fourier transform of the Moiré pattern in the dashed square. Scale bar 100 nm. Reprinted from Ref. 174 with permission.

plane displacement observed using our multiscale approach (0.23 Å) as shown in **Figure 6-3**. For a graphene sheet perfectly aligned with the h-BN substrate, considering the lattice mismatch of 1.8%, the periodicity of Moiré pattern is ~14nm which is consistent with the length of the Moiré pattern observed in different experimental studies.[173,174]

6.4 Conclusions

In this chapter, we show the general framework of our multiscale modeling approach that connects nanoscale and micrometer scale, expanding the predictive power of current simulation methods. The application of multiscale methods potentially should be able to address the Mechano-Electro-Chemical coupling problem occurred in 2D materials. To demonstrate the validity of our approach, we compute the elastic deformations in 2D heterostructure materials with a Moiré pattern, showing an excellent agreement between our approach and experimental data. In the next two chapters, more examples using this multiscale modeling approach will be discussed in understanding and tuning 2D materials for energy applications.

Chapter 7 Mechanisms for engineering highly anisotropic conductivity in a layered covalent-organic framework

Reprinted (adapted) with permission from **D. Er**, L. Dong, and V. B. Shenoy. *Mechanisms for Engineering Highly Anisotropic Conductivity in a Layered Covalent Organic Framework*. **Journal of Physical Chemistry C**, 120(1): 174-178 December 2015

Synopsis

Two-dimensional (2D) covalent-organic framework (COF) materials provide a promising solution to the lightweight, durable, and flexible electronic applications such as organic photovoltaics and organic light-emitting diodes. In this paper we report a theoretical study based on density functional theory calculations on a recently synthesized covalent- organic framework that has been experimentally demonstrated to possess excellent carrier mobility and photoconductivity along the vertical direction. Our calculations reveal the dependence of the carrier mobility on the number of layers and the stacking order, and show that the conduction is achieved by electron hopping between adjacent layers along the vertical pathways that are composed of aligned donor or acceptor groups. We find that the direct band gap in a monolayer shifts to an indirect band gap in bulk (multiple layers), with decreased carrier effective masses along the vertical direction. The vertical interlayer interaction further enhances the in-plane charge transfer from the donor to the acceptor parts, and hence the probability of electron hopping between adjacent layers. Our results not only explain conductivity enhancement mechanism in COFs, but also provide guidelines in designing highly conductive 2D polymer optoelectronic devices.

7.1 Introduction

Two-dimensional polymers (2DPs) are promising for flexible electronic applications such as organic photovoltaic and organic light emitting diodes (OLEDs).[175–177] Since their discovery,[178] these materials have attracted a great amount of research interest due to their excellent mechanical properties, thermal stability, relative ease of large scale production, and transparency to visible light.[179–185] However, the viability of 2DPs in practical electronic devices is hindered by one problem, namely, how to achieve a high conductivity while maintaining a proper bandgap.[186] In fact, such a conflict exists in various kinds of 2D electronic materials.[187,188] For example, graphene can offer surprisingly high conductivity via its in-plane π-conjugated orbitals;[16,92,186,187,189] however, the absence of a band gap in graphene remains as huge obstacle for most electronic applications. [190,191] On the other hand, many two-dimensional polymers can offer required band gap for electronic and optoelectronic applications.[192,193] For instance, many 2DPs provide a band gap in the range of 1.7-4.0 eV[192–194] that is suitable for photovoltaic applications according to the Shockley–Queisser limit.[195] Their carrier mobility, however, is very low due to the flat band gap structure.[190,196] Therefore, a manipulation of both band gap and carrier mobility should be considered simultaneously to realize conductive 2D polymers.

The manipulation calls for complete understanding of both microscopic and macroscopic properties of 2DPs layered materials. One key question is to understand and modify the electronic conductivity by changing planar structures of polymers and also the stacking sequence and number of layers, which requires a multiscale simulation approach. To answer this question, one possible way to realize a conductive 2D polymer is to design a ordered donor and acceptor structure.[175,197,198] Recently, Feng *et al.* have synthesized a covalent organic framework (COF) that has a unique vertically stacked multi-layer structure with the donor (D) and acceptor (A) functional groups segregated in the basal plane.[199] The D (and A) groups of different layers, however, stack along the vertical direction in a face-to-face manner, leading to a relatively high mobility (0.04 and 0.01 cm^2 $V^{-1}s^{-1}$ for electron and hole mobilities respectively) along the vertical direction under Xenon light excitations.[199] This discovery renewed interests in conducting polymers. Dogru *et al.* improved the 2DP mobility by modifying the COF structure and proposed a model system for better control over the electronic properties.[200]

In this chapter we report a theoretical study using density functional theory (DFT) calculations on the electronic properties of a COF structure, which is composed of triphenylene donors at the vertices and benzothiadiazole acceptors on edges. Such a COF is referred to as DA-COF in the rest of this chapter. Its anisotropic electronic properties such as the band structure and carrier effective masses are investigated with emphasis on their dependence on the number of layers. Our results suggest that the experimentally observed high conductivity in this layered DA-COF is a result of the enhanced intra-layer charge transfer upon increased interlayer interactions, which significantly changes the electronic band structure. The direct band gap in monolayer shifts to an indirect band gap in bulk (multiple layers), with a decreased effective mass for carriers along the vertical direction. The vertical interlayer interaction further enhances the in-plane charge transfer from the D to A parts, and hence the probability of electron hopping between adjacent layers. Our study provides useful information for designing 2DPs with anisotropic transport property, which is desired in optoelectronic applications.

7.2 Method

Our DFT calculations were performed using the Vienna Ab Initio Simulation Package (VASP)[78,79,201,202] with the Perdew-Burke-Ernzerhof (PBE) type of generalized gradient approximation (GGA) for exchange and correlation functionals [81] and the projector augmented wave pseudopotentials (PAW)[80] for electron-core interactions. An energy cutoff of 400 eV was used for plane wave basis expansion with a 12×12×1 Monkhorst-Pack K-points sampling. The atomic positions in the COF multilayers were relaxed so that the force on each atom is less than 0.001 eV/Å and the energy of the structure is converged to less than 5×10^{-6} eV/atom. The long range van der Waals interlayer interactions are treated by the dispersion correction with the Tkatchenko-Scheffler (TS) method[203], wherein the conventional DFT energy is supplemented with a pairwise interatomic vdW potential from non-empirical mean-field electronic structure calculations. A vacuum layer of more than 16 Å was placed perpendicular to the monolayers and bilayers in order to eliminate the interaction between periodic images.

7.3 Results and Discussions

7.3.1 Structural models of the DA-COF

DA-COF is a typical hexagonal mesoporous COF which consists of three-fold triphenylene vertices and two-fold benzothiadiazole edges linked by a boronate ester.[178,199] Within the monolayer, all atoms are co-planar as shown in **Figure 7-1**. The relaxed structure was found to have a lattice parameter $|\boldsymbol{a_1}| = |\boldsymbol{a_2}| = a = 30.02$ Å where $\boldsymbol{a}_1$ and $\boldsymbol{a}_2$ are the in-plane lattice vectors, consistent with previous results.[199] Within the unit cell, an alternating and segregated self-ordering donor-acceptor structure is constructed, where triphenylene and benzothiadiazole serve as donor (D) and acceptor (A) respectively. The self-assembled 2D polymers are composed of COF layers stacked by van der Waals interactions rather than covalent bonds and therefore may adopt various stacking sequences, which play an important role in their electronic properties. Two basic stacking sequences AA and AB are possible in the vertically stacked layered structure. In terms of the AA stacking, monolayers form a face-to-face columnar structure with A-on-A and D-on-D as shown in **Figure 7-1b**. On the other hand, a unit cell of AB stacking is obtained by offsetting the second layer with respect to the first layer by $(\frac{1}{2}\boldsymbol{a}_1, \frac{1}{2}\boldsymbol{a}_2)$ in the basal plane. The calculated total energy per AB-stacked unit cell is 0.750 eV and 0.737 eV higher than the corresponding values of the AA stacking for bilayer and bulk DA-COF, respectively. Therefore, AA stacking is energetically preferred than AB, which agrees well with previous experimental and simulation results.[199,204]

The AA stacking provides a macroscopic separation of the acceptor columns and the donor columns with broad interfaces, which enables an ambipolar transportation of electrons and holes, and hence a large vertical conductivity along the stacking axis.[199] It is worth pointing out that although some stacking structures with a zigzag shift from the AA stacking can have an even lower total energy[199] as shown in **Figure 7-2**, the conduction channel of columnar D or A parts, which is harmful for the carrier transport. In order to better understand the relationship between different stacking configurations and the conductivity (which again is the structure-property relationship), we first performed the energy calculation for AB, AA, and eclipsed AA stackings. The AB stacking has a much higher energy compared to the other two stacking sequences, and are therefore excluded from the discussion below. The energy difference between AA and eclipsed AA stackings are shown in **Figure 7-2**. The potential energy surface (or gamma surface), which indicates an energy minimum when the top layer is shifted with respect to the bottom layer for about 2.1 Å along **a1** and **a2**, respectively. This agrees well with previous publications.[199] Considering that the energy difference between the AA stacked unit cell and that of the shifted AA

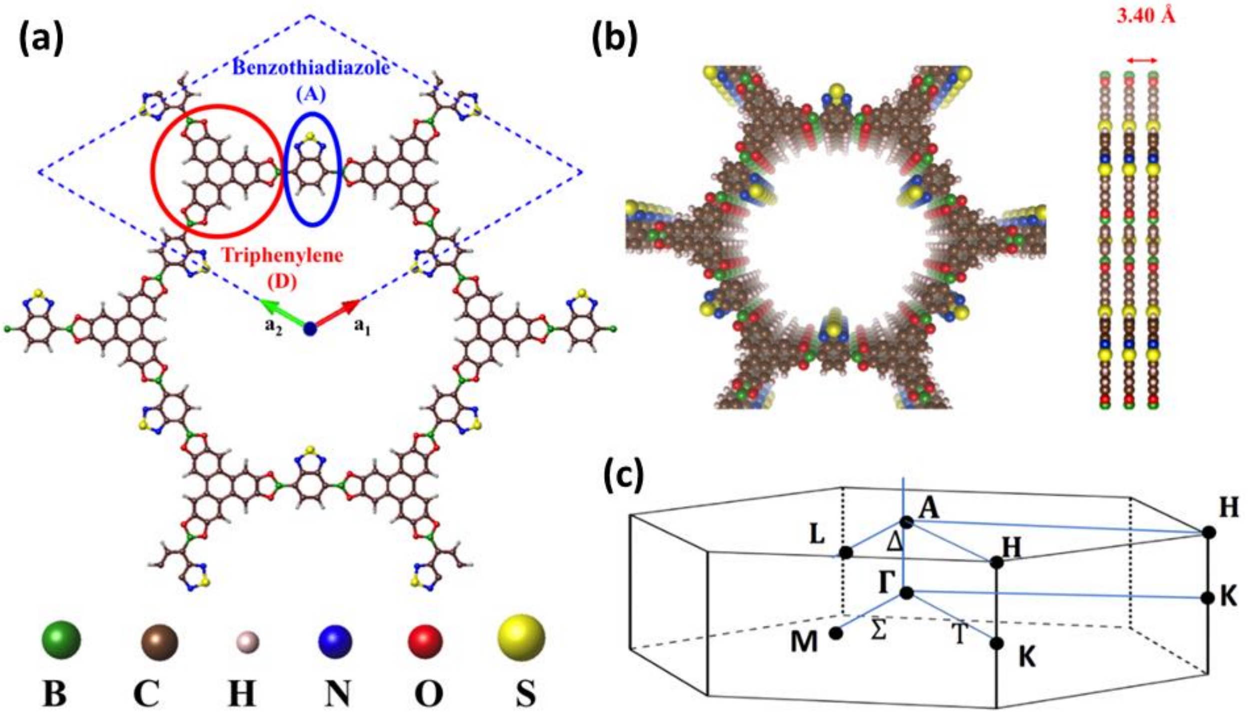

Figure 7-1 (a) Schematic depiction of the DA-COF hexagonal unit cell, **(b)** Schematics of vertically stacked face-to-face DA-COF with top and side views, and **(c)** reciprocal space BZ with notations for hexagonal symmetry.

stacking is less than 20 meV,[204] in this chapter we focus on the AA stacked structures because it has more desirable conduction channels orthogonal to the COF basal plane. Within this columnar structure, interlayer distance varies as a function of the number of stacked layers due to changes in the strength of the vdW interactions. The lattice parameters are kept as $a = 30.02$ Å, and the calculated interlayer distance in a bilayer (3.57 Å) is larger than that in the bulk (3.40 Å).

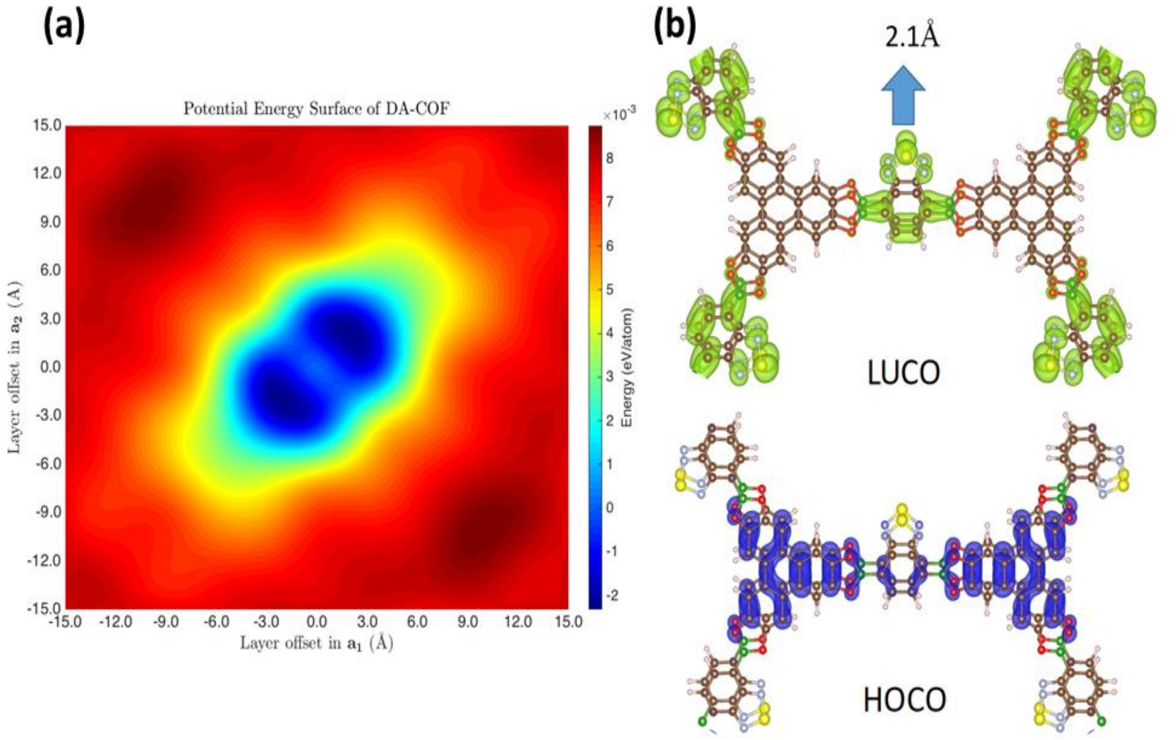

Figure 7-2 (a) Potential energy surface of different stacking shifts along $\mathbf{a}_1$ and $\mathbf{a}_2$ direction with respect to a fixed monolayer. Two local minima can be found as shown in figure of this gamma surface.[266] This plot provides a basic understanding of stacking modes problem in this DA-COF. **(b)** HOCO-LUCO plot of eclipsed AA stacking with 2.1 Å offset, which has the minimum energy. Less π –overlap between adjacent 2D layers has been observed.

7.3.2 Band structure

Optoelectronic properties of semiconductors are determined by their electronic band structure, wherein the conduction and valence band edges are essential to the photoluminescence spectrum and the device efficiency. The 2D monolayer displays a direct band gap with both the lowest unoccupied crystal orbital (LUCO) and the highest occupied crystal orbital (HOCO) located at the Γ point in the reciprocal space. This band gap, contrary to the vanishing band gap in graphene[16], offers possibilities for photoluminescent and photoelectric applications that are in agreement with Shockley-Queisser limit[195], and can offer a higher quantum efficiency without the involvement of phonons. However, the in-plane carrier mobility of the monolayer is very low because of the relatively flat LUCO and HOCO band edges shown in **Figure 7-3a**, which indicate that these orbitals are highly localized. From the charge densities of LUCO and HOCO in **Figure 7-3b**, and **c**, respectively, it is easy to identify that HOCO is primarily localized at the triphenylene donors, while LUCO resides on benzothiadiazole acceptors.

On the contrary, the separation between HOCO and LUCO charge densities, i.e., between electrons and holes, provides the foundation for a large columnar (out-of-plane) conductivity. As the number of stacked layers increases, HOCO and LUCO of adjacent layers start to overlap, allowing electron hopping from one layer to another. The band gap of AA-stacked multilayers keeps decreasing as the number of stacking layers increases. The band gap reduces from 1.73 eV in monolayer to 1.23 eV in bilayer, and eventually to 0.25 eV in bulk, respectively. Furthermore, the *direct* band gap in the monolayer shifts to an *indirect* band gap in bulk. The LUCO edge in bulk DA-COF locates at the A point while the HOCO edge is at the Γ point (**Figure 7-4**), yielding relatively high carrier mobility along the out-of-plane direction. The in-plane carrier mobility in bulk DA-COF, however, remains unchanged from the monolayer case. Therefore, a highly anisotropic conductivity is expected as the number of stacking layers increases.

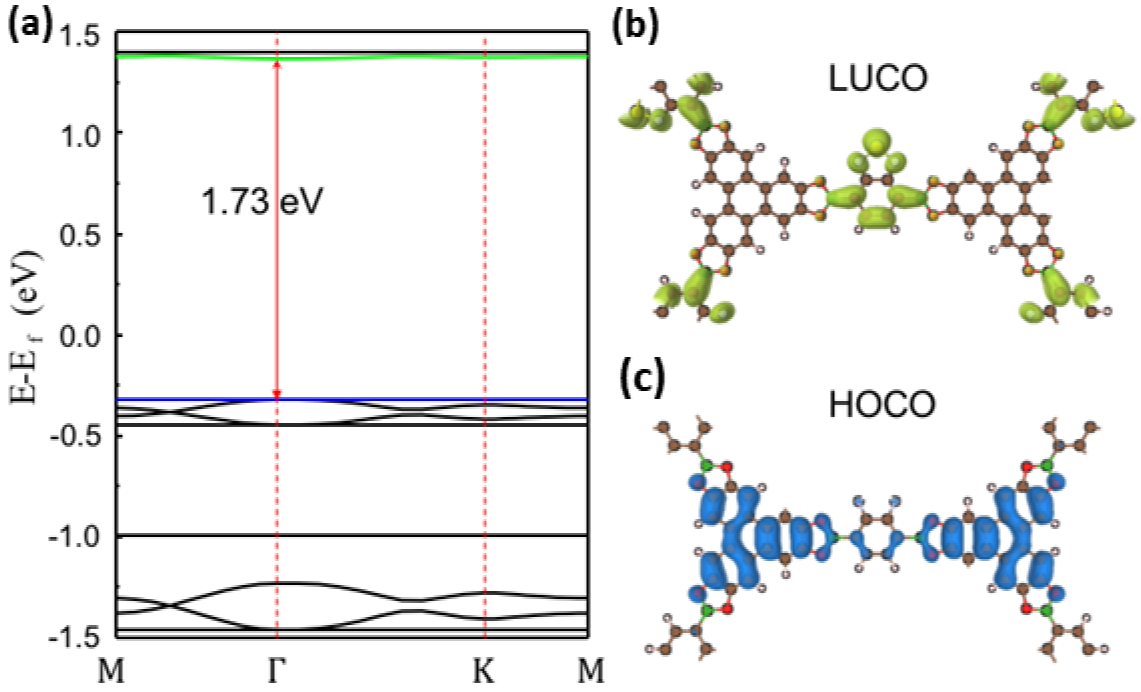

Figure 7-3 (a) Band structure of monolayer COF displays a direct HOCO-LUCO gap of 1.73 eV at the Γ point. Flat band structures of gap states indicate highly localized orbitals. **(b)** the LUCO state is located majorly on acceptors, while **(c)** the HOCO state is largely located on donors.

7.3.3 Effective mass and anisotropic mobility

In order to quantify the enhanced anisotropic conductivity, carrier effective mass of electrons (m_e^*) at the conduction band minimum and of holes (m_h^*) at valence band maximum can been calculated from the band structure using

$$m^* = \frac{\hbar^2}{\partial^2 E(k)/\partial k^2} \tag{1}$$

where E(k), k, and $\hbar$ correspond to energy, the reciprocal space vector, and reduced Plank constant, respectively. The calculated effective mass of electrons and holes are listed in **Table 7-1** in the units of free electron mass (m_e) for monolayer and bulk DA-COF. Effective mass of electrons and holes are reduced systematically, particularly along the vertical direction when periodicity starts to form with an increased stacking number of monolayers. The quantum confinement changes the band structure hence the effective mass (m*) of carriers; on the other hand, it provides higher possibility of carrier hopping along z direction. Effective mass of electrons and holes are comparable in magnitude, which

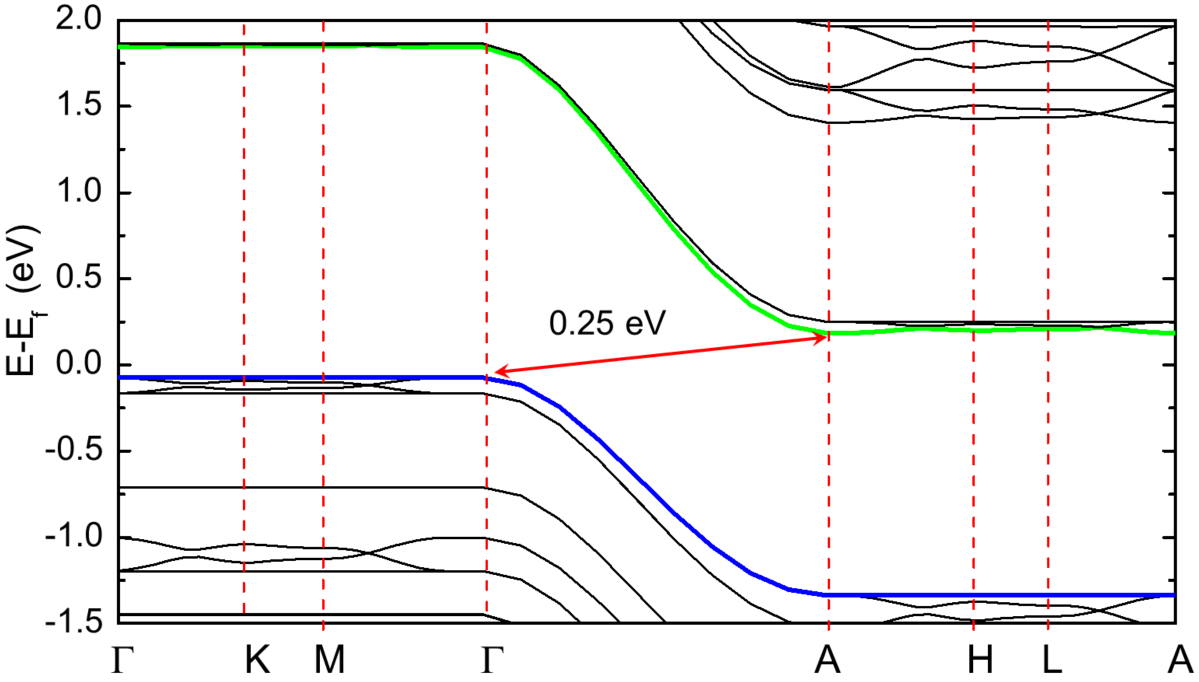

Figure 7-4 Band structure of vertically stacked DA-COF polymer in the bulk form. A highly curved band structure indicates an indirect band gap from Γ to A point in bulk with a decreased band gap value (0.25 eV) than that in the monolayer (1.73 eV).

indicates two channels of conduction are possible. Electrons have smaller effective mass than holes, which is in agreement with experiments.[199] A large anisotropy of conduction for both electrons and holes have been indicated from **Table 7-1**, because of the carrier effective mass along the stacking direction is one order of magnitude larger than that within the 2D basal plane. Note that the effective mass of carriers here is comparable and even smaller to that in traditional high performance semiconductor materials such as Si or GaAs, where promises in electronic devices applications are possible. It is also worth pointing out that the lowest energy eclipse is relatively moderate with the top layer shifted about 2.1 Å along $\mathbf{a}_1$ and $\mathbf{a}_2$ directions with respect to the bottom layer. In such a structure, the conduction is still mainly along the vertical direction as the carrier effective masses in this direction is significantly smaller than the in-plane ones. Also the increased effective mass of carriers along *z* direction indicates the eclipsed AA stacking is not beneficial for vertical conductivity.

Table 7-1 Effective mass of carriers in DA-COF with comparison to traditional semiconductors.

	Monolayer (in-plane)	Monolayer (vertical)	Bulk AA (in-plane)	Bulk AA (vertical)	Eclipsed-AA(Γ-X)	Eclipsed-AA	Si	GaAs
Electron $\boldsymbol{M_e^*/m_e}$	0.523	N/A	0.683	0.025	1.240	0.070	0.2	0.067
Holes $\boldsymbol{M_h^*/m_e}$	21.225	N/A	7.701	0.024	4.342	0.086	0.16	0.082

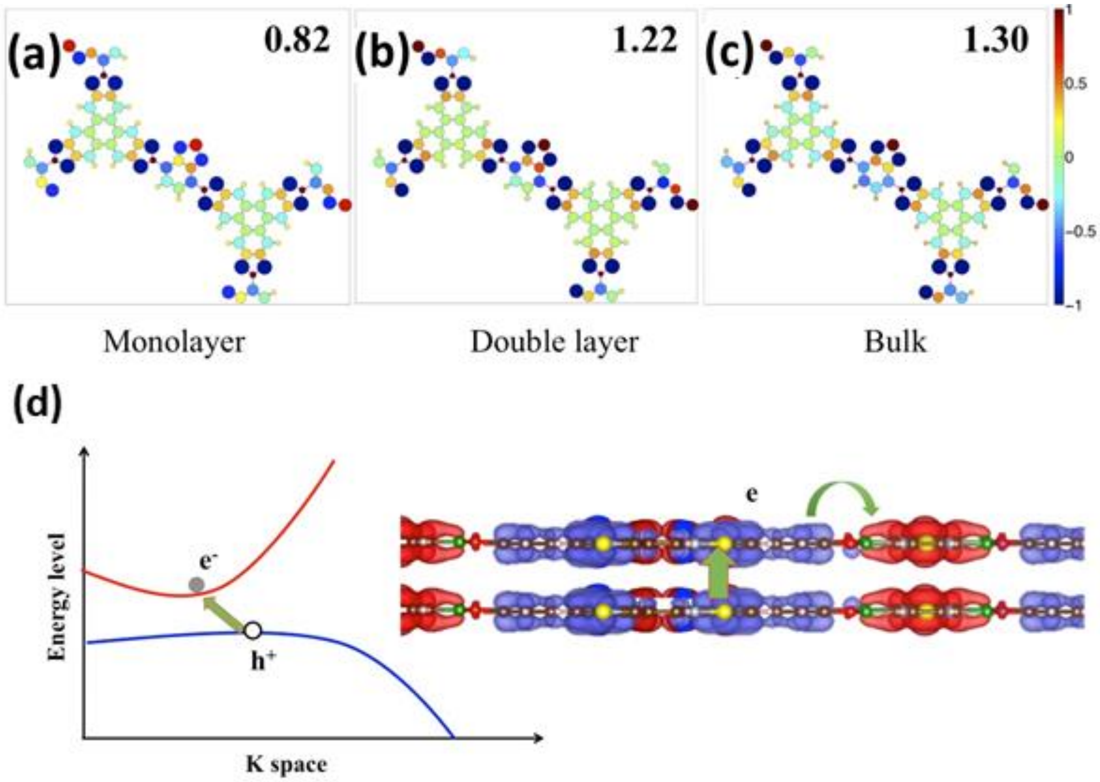

Figure 7-5 Schematics of charge transfer map showing charge accumulation and depletion regions. The amount of charge transfer between D-A increases, respectively, from **(a)** 0.82 e in monolayer to **(b)** 1.22 e in bilayer, and eventually to **(c)** 1.30 e in the bulk case. Dot sizes indicate the amount of charge localized on each atom and the color code illustrates the amount of transferred charge. **(d)** Schematic depiction of interlayer hopping in DA-COF, where electrons (e-) and holes (h^+) locate at D and A parts, respectively. The excitation leads to hopping of carriers along vertical direction.

7.3.4 Charge transfer

To gain a deeper understanding in the mechanism of the enhanced conductivity along *z* direction in stacked 2D polymers, we employed the Bader charge analysis[121] to reveal that the enhanced vertical conductivity of carriers can be partially explained by charge transfer between the D and A parts. Within the basal plane, the D and A parts are well separated and the D part transfers electrons to the A part via the B-O bridges as shown in **Figure 7-5**. Red and blue colors indicate regions of electron accumulation and depletion, respectively, while the size of each dot proportionally depicts the amount of charge localized on each atom. The amount of charge transferred from D to A is a qualitative indicator of the strength of D-A interaction within the 2D plane, for which a stronger interaction results in a larger amount of transferred charge. The transferred charge in monolayer, bilayer and bulk DA-COF is approximately 0.82 $|e|$, 1.22 |e|, 1.30 |e|, respectively, showing that the vertical interaction between the layers further enhances the in-plane charge transfer and therefore the probability of electron hopping between adjacent layers.

7.4 **Conclusions**

We performed a theoretical study on a newly synthesized 2D COF structure with large anisotropic conductivity due to the segregated columnar arrangement of donor and acceptor groups. Our results show that HOCO and LUCO are located at the D and A groups, respectively, enabling a highly anisotropic conductivity. The calculated effective mass along the vertical direction is much smaller than that in the basal plane, which is beneficial for vertical carrier transport. The enhanced out-of-plane conductivity from monolayer to bulk is accompanied by a stronger charge transfer between D and A. Our result can be generalized to a broad 2D COF family, in which various applications can be realized in $\pi - \pi$ stacked multilayer structures according to the numerous combination of aromatic building blocks.

.

Chapter 8 A model to determine the chemical expansion in non-stoichiometric oxides based on the elastic force dipole

Reprinted (adapted) with permission from **D. Er**, J. Li, M. Cargnello, P. Fornasiero, R. J. Gorte, and V. B. Shenoy. *A Model to Determine the Chemical Expansion in Non-stoichiometric Oxides Based on the Elastic Force Dipole*. **Journal of the Electrochemical Society**, 161 (11): F3060-F3064 September 2014

Synopsis

In this chapter a novel continuum model informed by density functional theory (DFT) simulations is presented and used to predict the chemical expansion observed in non-stoichiometric oxides. We introduce an elastic dipole tensor that describes the long-range elastic fields created upon formation of oxygen vacancies. We show that this tensor, which can be accurately determined through first-principle DFT calculations, can be used to predict the chemical expansion of ceria and in general other non-stoichiometric oxides. Compared to previous work where expansivity was obtained with empirical potentials, our work provides an efficient way of computing it directly by DFT calculations. Furthermore, we discuss how the elastic dipole tensor can predict the O_2 partial pressure vs O/Ce ratios in strained systems and show that CeO_2 can be reduced more easily in the presence of tensile strains. More generally, the elastic dipoles can be used in continuum models to predict the distribution of vacancies near nanocrystal surfaces, grain boundaries and extended defects such as dislocations and hence provide information on how these structures and defects influence the overall reducibility of the material.

8.1 Introduction

Non-stoichiometric oxides are widely used in high temperature energy applications, such as automotive catalysis, solid oxide fuel cells (SOFCs), oxygen permeation membranes, and gas conversion/reformation catalysis.[205–208] Among all these oxides, cerium oxide (ceria), either in the pure phase or mixed or doped with other transition metals and lanthanides, is among the most studied non-stoichiometric oxides and has attracted widespread industrial interest. Ceria, typically in the form of a mixed oxide with zirconia, has been included in automotive emission-control catalysts for many years[205,209–211] and has applications in solid oxide fuel cells (SOFCs), water-gas-shift [212,213] and hydrocarbon-reforming catalysis,[214] and hydrocarbon oxidation catalysis[215]. The reversible transition of ceria between Ce(IV) and Ce(III) oxidation states enables the storage and release of oxygen, providing many possibilities for practical applications. For example, in automotive three-way catalysts, ceria (as a solid solution with zirconium) acts to buffer the exhaust composition through its oxygen-storage capacity (OSC). In this and other catalytic applications, the catalytic performance depends on the oxygen non-stoichiometry.[205] Therefore, controlling reversible oxygen stoichiometry in ceria is pivotal.

In addition to oxygen stoichiometry changes due to environment, temperature, and oxygen partial pressure (P_{O_2}), which result in changes in electrical properties and phase stability, significant mechanical stresses are also induced from changes in the lattice parameter due to the presence of impurities such as defects, also referred to as *chemical expansion.*[216–221] For example, an increase in the effective thermal expansion coefficient due to oxygen loss upon heating in air has been observed in a Pr-doped ceria ($Pr_{0.1}Ce_{0.9}O_{2-\delta}$) SOFC cathode

[222]. Chemical expansion has been shown to lead to cracking of cerium oxide membranes under the large oxygen partial pressure (P_{O_2}) gradients found in SOFC operation.[223,224] Moreover, the increase in lattice constant is reported to decrease the elastic modulus,[225] which must be consider for safe operation of electrochemical devices. Chemical expansion is also involved in the large change of strain in ceria thin films at low temperature as the result of oxygen vacancy rearrangement,[226–228] as well as a conductivity change in highly strained heterostructure thin films.[224]

While the chemical expansion associated with electro-chemomechanical properties has been confirmed by many experimental measurements, the origin is not yet well understood.[217,218,229,230] In the past, there have been several attempts at developing numerical models of the phase diagrams and composition of CeO_2 for a wide range of conditions.[231–233] More recently, Yildiz *et al.* have studied chemical expansion by advancing a model which considers the effects of cation radius changes and the formation of an oxygen vacancy using Molecular Dynamics (MD) simulations.[216] It is well known that MD simulations are less accurate than DFT calculations for predicting defect energies in non-stoichiometric oxides.[234] However, calculating chemical expansion with DFT calculations can be a time consuming task, since larger and larger unit cells have to be considered with decreasing concentration of the defects.

In this chapter we report a new continuum model, informed by DFT simulations, to predict the chemical expansion. Unlike empirical methods, an elastic dipole tensor is here precisely calculated by DFT calculations. The elastic dipole tensor can link chemical expansion and oxygen-vacancy concentrations of using a continuum method. By introducing a chemical-expansion coefficient, which reflects the combination of the two competing effects, a simple expression can be obtained for describing non-stoichiometry with a dipole tensor term. This method, which is in excellent agreement with recent experimental data, allows for the calculation of chemical expansion and the prediction of defect properties such as non-stoichiometric deviation during reduction of ceria and other non-stoichiometric oxides. It is worth pointing out that our study of strained ceria provides information which may be extended to oxidation thermodynamics more generally. The dipole tensor also allows for calculation of the formation energy of defects in the presence of complex strain fields that can arise at surfaces, grain boundaries and extended defects.[235]

8.2 **Method**

8.2.1 The *ab initio* calculation

Ab initio density functional theory simulations are used to calculate the chemical expansion of bulk ceria with one oxygen vacancy in a unit cell whose size is large enough that finite size effects are not significant. Generally, the chemical expansion is defined as

$$\epsilon_c = \frac{a - a_0}{a_0} \tag{8-1}$$

where a is the lattice parameter for $Ce^{4+}_{1-2\delta}Ce^{3+}_{2\delta}O_{2-\delta}$, and a_0 is the lattice parameter for stoichiometric ceria ($\delta = 0$). A test through size dependent convergence studies suggests that a (2 × 2 × 2) cell is large enough to eliminate the finite size effect. In the case of one oxygen vacancy ($\delta = 0.03125$) in a (2 × 2 × 2) cell ($Ce_{32}O_{63}$), the calculated ϵ_c is 0.0030. **Figure 8-1** shows the position of the ions and the charge distribution around the oxygen vacancy as obtained from DFT calculations. Calculations of the charge density difference[236] (CDD) have been performed in order to determine the charge transfer upon the formation of an oxygen vacancy. In non-defective, fully oxidized ceria (CeO_2), the oxygen atoms assume a tetrahedral coordination each surrounded by four Ce atoms. With the formation of an oxygen vacancy, the local charge redistribution between Ce and O results in local expansion of the lattice. The localization of the two extra electrons in the Ce 4f band leads to charge transfer, as shown in **Figure 8-1b**. Given the small stoichiometry deviation, charge balance can be written using Kröger-Vink notation as follows:

$$2[\mathrm{V}_{\mathrm{O}}^{\cdot\cdot}] = [\mathrm{Ce}_{\mathrm{Ce}}^{\prime}] \tag{8-2}$$

where $\mathrm{Ce}_{\mathrm{Ce}}^{\prime}$ is a Ce(III) species located at Ce(IV) site with one negative charge, and $\mathrm{V}_{\mathrm{O}}^{\cdot\cdot}$ is an oxygen vacancy with double positive charge. On the one hand, the formation of positively charged oxygen vacancies and negatively charged $\mathrm{Ce}_{\mathrm{Ce}}^{\prime}$ leads to a lattice contraction due to electrostatic interactions, which results in a net local contraction of the lattice around the vacancy. On the other hand, the localization of the two extra electrons into Ce 4f orbitals (Ce^{4+} to Ce^{3+}) leads to an increase in cationic radius from 0.97 to 1.143 Å (using Shannon ionic radii[237]) and consequent lattice expansion. The result of these two opposite effects is chemical expansion in non-stoichiometric ceria. According to our model (**Figure 8-1**), the cations are shift away from the oxygen vacancy by approximately 0.10 Å, whereas the anions shift by approximately 0.16 Å in the direction of the oxygen vacancy. This conclusion is in accordance with recent experimental and computational observations.[216,238,239]

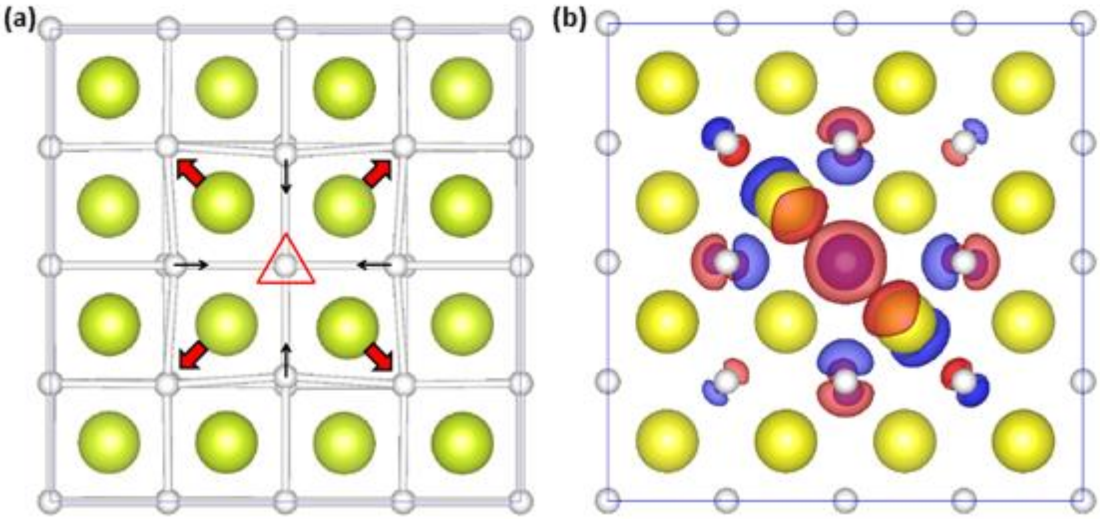

Figure 8-1 Green-yellow spheres represent cerium, white small balls represent oxygen, and the red triangle shows the oxygen vacancy. **(a)** Local relaxation patterns near the oxygen vacancy, and **(b)** CDD charge transfer with the formation of oxygen vacancy, two tetravalent Ce cites are reduced to trivalent Ce sites.

8.2.2 Modeling Chemical Expansion with the Elastic Dipole Tensor

In the presence of long-range elastic interactions we introduce a continuum model with elastic force dipole tensor to understand the chemical expansion. Point defects introduce both short- and long-range lattice distortions. Short-range distortions are considered those affecting the immediate periphery of the created oxygen vacancy, whereas long-range ones affect the overall dimensions of the crystal. Long-range changes (both in terms of volume and shape) are conventionally characterized by the elastic dipole tensor,[240] G_{ij},which can be fully determined by an examination of stress-strain effects around a defect. To ensure that there are no far-fields moments in equilibrium, the dipole tensor has to be symmetric. To show that the oxygen vacancy can indeed be modeled as an elastic force dipole, we derive the elastic fields it generates based on energy arguments. The total energy of a defect can be represented by the elastic strain energy in the bulk due to its strain field ϵ_{kl} and its self energy. Assuming an elastic media of infinite extent an oxygen vacancy, when the system is subjected to strain, the total energy can be given by

$$f = \int G_{ij} \frac{\partial u_i}{\partial x_j} \delta(x) dv + \frac{1}{2} \int C_{ijkl} \epsilon_{ij} \epsilon_{kl} \, dv \tag{8-3}$$

with u_i, f, G_{ij}, C_{ijkl},and ϵ_{ij} representing the displacement field, the total energy, the elastic dipole tensor, the elastic stiffness tensor, and the strain tensor, respectively. Note that the first term is the product of the dipole tensor and strain, which corresponds to the elastic energy of the dipole. The variation of f with respect to u has to vanish in equilibrium:

$$\frac{\delta f}{\delta u} = G_{ij} \frac{\partial \delta(x)}{\partial x_j} + C_{ijkl} \frac{\partial^2 u_k}{\partial x_l \partial x_j} = 0. \tag{8-4}$$

Rearranging Equation (8-4), we can obtain F_i, which is the body force applied to the system concentrated at the origin where the dipole is located.

$$F_i = -C_{ijkl} \frac{\partial^2 u_k}{\partial x_l \partial x_j} = G_{ij} \frac{\partial \delta(x)}{\partial x_j} \tag{8-5}$$

Using the Green's function, $\mathcal{g}_{ij}(x, x')$, which provides the displacement in the i-th direction at x due to a unit point force acting at x' in the j-th direction, we can obtain the expression for the displacement field:

$$u_i(x) = \int \mathcal{g}_{ip}(x) F_p \, dv = \int \mathcal{g}_{ip}(x) \, G_{pj} \frac{\partial \delta(x)}{\partial x_j} \, dv \tag{8-6}$$

Integrating equation (8-6), we obtain the expression of displacement field in the presence of an oxygen vacancy

$$u_i(x) = -\frac{\partial \mathcal{g}_{ip}(x - x')}{\partial x_j} |_{x = x'} \, G_{pj}, \tag{8-7}$$

that precisely corresponds to the field created by a dipole confirming the validity of expression for the total energy given in Equation (8-3). Next, we use this expression to compute the energy of the vacancy in the presence of an external strain.

With the elastic dipole tensor defined, we now proceed to compute the lattice constant of a crystal with a given concentration of vacancies. We assume that an oxygen vacancy concentration is, $\frac{\delta}{V_c}$, where δ and V_c is the non-stoichiometric deviation and volume of supercell, respectively. The goal is to find the overall strain of the cell that will lead to minimization of the overall energy change,

$$\Delta f = \frac{\delta}{V_c} \widehat{G}_{ij} \epsilon_{ij} + \frac{1}{2} C_{ijkl} \epsilon_{ij} \epsilon_{kl} \tag{8-8}$$

where $\widehat{G}_{ij}$ is the elastic dipole tensor per unit volume. The first term here again is the product of the applied strain and the dipole density, which gives the energy that the dipole can gain due to lattice expansion, while the second term gives the energy cost associated with deformation of the bulk crystal. A competition between these two effects determines the chemical expansion. Again, the derivative of energy with respect to the strain gives the chemical expansion

$$\mathrm{\epsilon_c} = -\frac{\delta\,\mathbf{tr}(\mathbf{C}^{-1}\widehat{\mathbf{G}})}{3\mathrm{V_c}} \tag{8-9}$$

Consequently, the chemical expansion coefficient a_c is defined as,

$$a_c = \frac{\epsilon_c}{\delta} = -\frac{\mathbf{tr}(\mathbf{C}^{-1}\widehat{\mathbf{G}})}{3\mathrm{V_c}} \tag{8-10}$$

Therefore, by knowing the elastic dipole tensor $\widehat{G}_{ij}$, chemical expansion and chemical expansion coefficient can be determined without the need for computing the optimum lattice constants at each concentration.

8.3 **Result**

8.3.1 Oxygen Vacancy Formation Energy and Elastic Dipole Tensor

In the previous section, the continuum model of elastic dipole tensor was discussed which emphasizes the elastic dipole tensor per unit volume as the key factor. In this section we present the results from DFT simulations and compare our results with other's experimental and theoretical data. The essential parameter for this model, the elastic dipole tensor, $\widehat{\boldsymbol{G}}_{ij}$, was determined using the formation energy under different strain states. Generally, the full tensor of $\widehat{\boldsymbol{G}}_{ij}$ should be calculated by applying different strain states. However, for ceria, the cubic symmetry ($(\epsilon_c)_{ij} = 0, i \neq j$) requires only the measurement of the mean diagonal component of ϵ_c. In our calculations, we introduced strains in CeO_2 by changing the lattice constants and by relaxing all the internal coordinates. Several strain states, such as tensile strain, shear strain, and hydrostatic strain, were applied to the supercell. The oxygen formation energy per unit volume is defined as:

$$E^f_{V_0}(\epsilon) = E(CeO_{2-\delta}, \epsilon) - E(CeO_2, \epsilon) - \sum_i n_i \mu_O \tag{8-11}$$

where $E(CeO_{2-\delta}, \epsilon)$ is the energy of non-stoichiometric ceria under strain, while $E(CeO_2, \epsilon)$ is the energy of pristine ceria under the same strain, n_i denotes the number of oxygen atoms removed from the supercell and μ_O is the chemical potential of oxygen. The change of formation energy only comes from the presence of oxygen vacancy under strain. Therefore, first order Taylor expansion of $E^{f}_{V_0}(\epsilon)$ to ϵ gives the relation:

$$E^{f}_{V_O}(\epsilon_{ij}) = E_0 + \widehat{G}_{ij}\epsilon_{ij} \tag{8-12}$$

The derivative gives the elastic dipole tensor (neglecting higher order terms),

$$\widehat{G}_{ij} = \frac{dE^{f}_{V_O}(\epsilon_{ij})}{d\epsilon_{ij}} \tag{8-13}$$

According to Equation (8-11)-(8-13), the formation energy variation with strain is shown in **Figure 8-2**. Due to the cubic symmetry of ceria, the mean diagonal component of $\boldsymbol{\widehat{G}}_{kk}$ is sufficient to determine the ϵ_c. Therefore the orientations of off-diagonal components

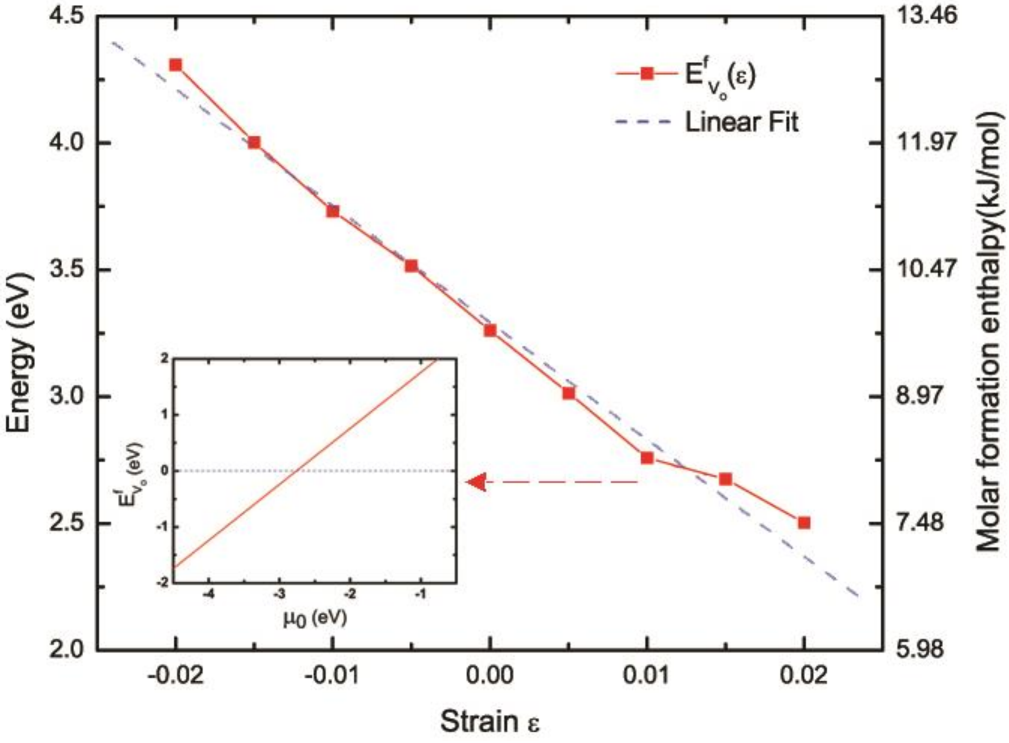

Figure 8-2 Formation energy of an oxygen vacancy varies with strain applied in the supercell (hydrostatic). The derivative gives the trace of averaged elastic dipole tensor $\widehat{G}_{ij}$. The inset shows the formation energy for 1% tensile strain as a function of the oxygen chemical potential.

vanish and leave only the diagonal components for the elastic dipole tensor. The calculated elastic dipole tensor is obtained by linear fitting from **Figure 8-2**,

$$\hat{G}_{ij} = \begin{pmatrix} -15.43 & 0 & 0 \\ 0 & -15.43 & 0 \\ 0 & 0 & -15.43 \end{pmatrix} eV \tag{8-14}$$

According to experimental data of elastic tensor for ceria,[241,242] C_{11}, C_{12}, C_{44} and the bulk modulus **B** with values 403.0 GPa, 105.0 GPa, 60.0 GPa, and 204.0 GPa, respectively, a_c is calculated as 0.0975. This result agrees well with the experimental data of non-stoichiometric chemical expansion obtained by several researchers,[216,243–245] which further

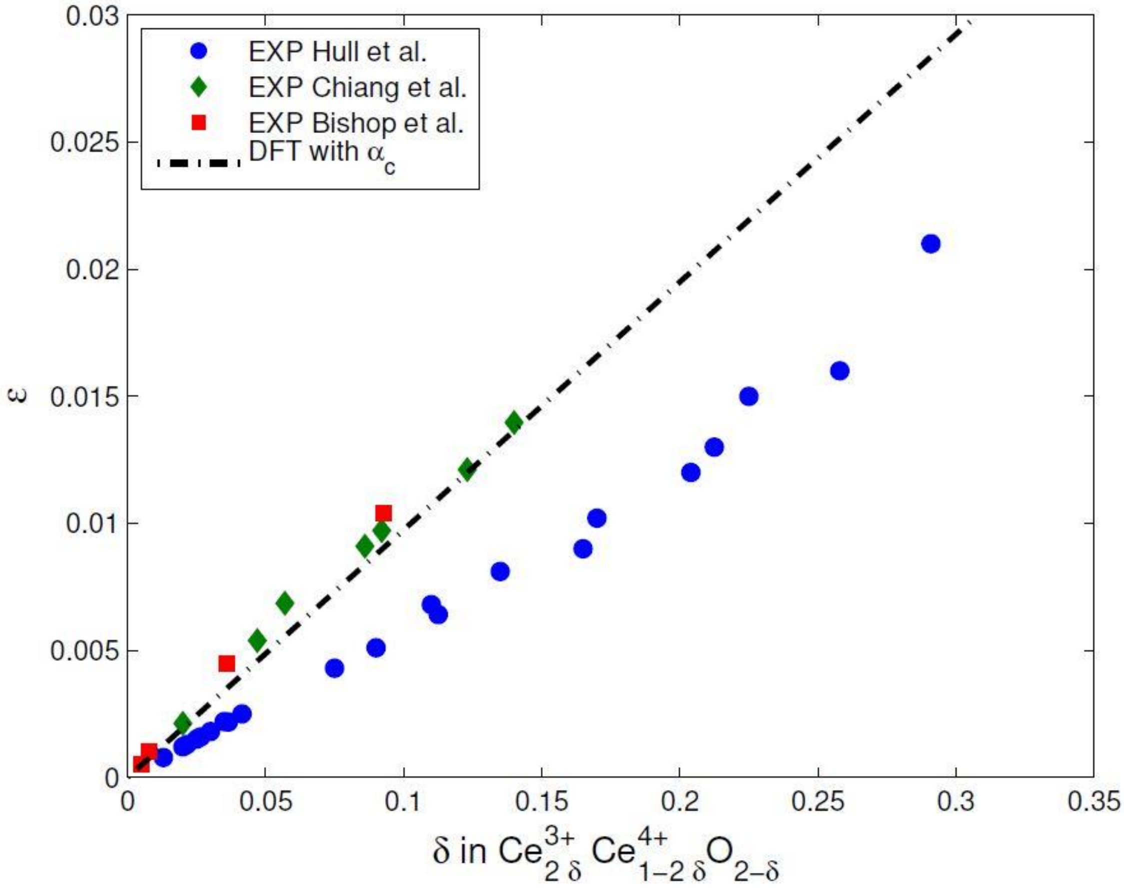

Figure 8-3 Chemical expansion of ceria with the predicted value from the model using DFT calculations and experimental values. Data from Ref. [243–245].

validates our model. The predicted chemical expansion of $\mathrm{Ce}^{4+}_{1-2\delta}\mathrm{Ce}^{3+}_{2\delta}\mathrm{O}_{2-\delta}$ as a function of δ, is plotted in **Figure 8-3**, with comparison to experimental values from several authors.

8.3.2 The Reducibility of Ceria

Knowing the elastic dipole tensor, the oxygen formation energy, and the predicted chemical expansion, we now investigate the role of strain on reducibility of ceria. According to the Kröger-Vink notation, when reduced from CeO_2 to $\mathrm{CeO}_{2-\delta}$, Ce^{3+} ions form on Ce^{4+} lattice sites. It is generally agreed that these electron polarons in low P_{O_2} ceria-based oxides are compensated by positively charged oxygen vacancies under reducing conditions. Kofstad and Hed,[246] Kevane,[247] and Blumenthal *et al.*[248] had discussed whether these substitutional negative defects were balanced by Ce interstitial, $\mathrm{Ce}_i^{\cdot\cdot\cdot\cdot}$ or by oxide ion vacancy, $\mathrm{V}_{\mathrm{O}}^{\cdot\cdot}$. Later experimental works have confirmed that the dominant cations in $\mathrm{CeO}_{2-\delta}$ are oxygen vacancies. Faber *et al.*[249] examined the electron density distribution using X-ray diffraction (XRD), and concluded that Ce interstitials are less than 0.1 % of the total defects in $CeO_{1.91}$. Also the *Le Chatelier* principle suggests that the $\mathrm{V}_{\mathrm{O}}^{\cdot\cdot}$ dominates at low oxygen concentrations. Therefore, in this work, we assume that the dominant anion is $\mathrm{Ce}'_{\mathrm{Ce}}$ and the dominant cation is $\mathrm{V}_{\mathrm{O}}^{\cdot\cdot}$. Using Kröger-Vink notation, the thermal reduction of CeO_2 can be written as:

$$2\mathrm{Ce}_{\mathrm{Ce}}^{\mathrm{X}} + \mathrm{O}_{\mathrm{O}}^{\mathrm{X}} \rightarrow \mathrm{V}_{\mathrm{O}}^{\cdot\cdot} + 2\mathrm{Ce}'_{\mathrm{Ce}} + \frac{1}{2}\mathrm{O}_2\ (\mathrm{g}) \tag{8-15}$$

With decreasing oxygen partial pressure (P_{O_2}) or increasing temperature, oxygen vacancies form with charge compensation through two electrons, localized on trivalent cerium cations ($\mathrm{Ce}'_{\mathrm{Ce}}$), forming polarons. An Arrhenius type equation at equilibrium relating the oxygen partial pressure to the non-stoichiometric composition according to the law of mass action and Gibbs free energy can be written as,

$$\delta = 4^{-\frac{1}{3}} P_{O_2}^{-\frac{1}{6}} e^{\frac{\Delta H_f(\epsilon)}{3k_B T}} e^{\frac{\Delta S}{3K_B}} = A P_{O_2}^{-\frac{1}{6}} e^{\frac{\Delta H_f(\epsilon)}{3k_B T}} \tag{8-16}$$

Here the formation energy of oxygen vacancy incorporates the applied strain introduced to the non-stoichiometric ceria. The configurational entropy change with strain is negligible compared to the enthalpy change. With an entropy ΔS of this reaction, 62.3 J K^{-1} mol^{-1}, taken from Ref 229,250, the coefficient *A* is determined.

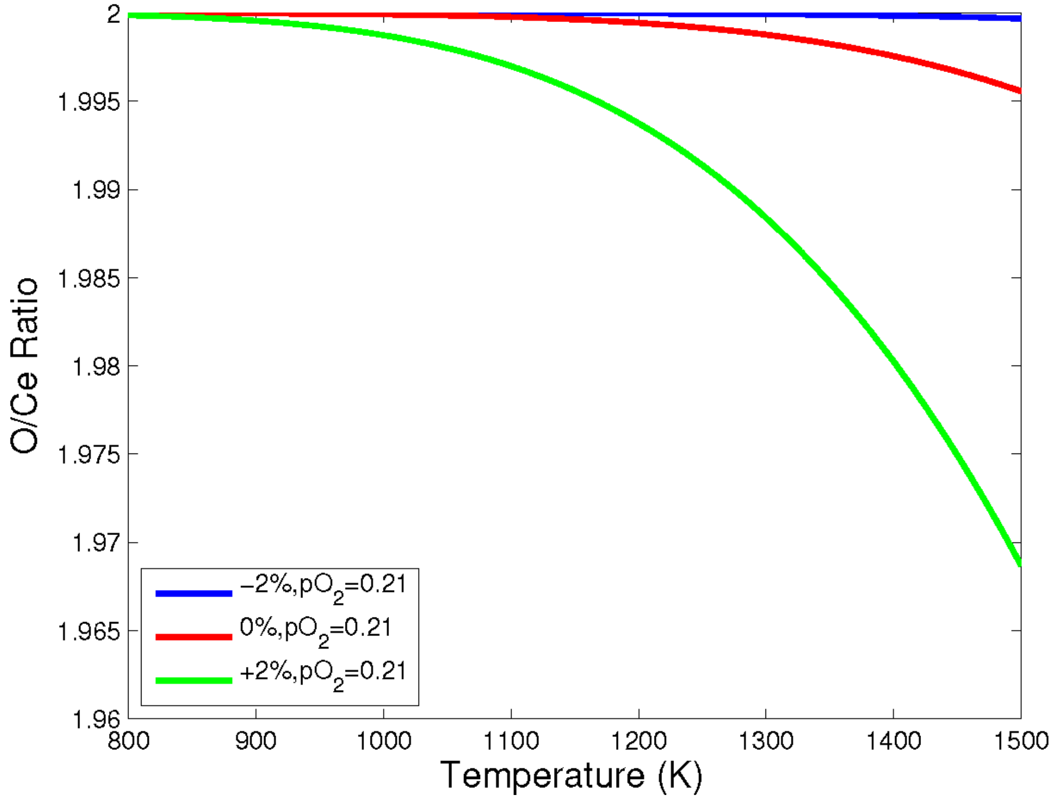

Figure 8-4 Reducibility of strained ceria expressed in terms of the O/Ce ratio. The temperature-dependent stoichiometry of Ce$O_{2-\delta}$ in air is modeled with the presence of strain in air at 2% compressive strain, 2% tensile strain, and 0% strain states with oxygen partial pressures (P_{O_2}) corresponding to 0.21.

In **Figure 8-4** we show the calculated non-stoichiometry as a function of temperature for 2% tensile strain, 2% compressive strain, and 0% strain with oxygen partial pressure (P_{O_2}) corresponding to atmospheric pressure. The presence of tensile strain can significantly increase the reducibility of ceria at a certain temperature while that of compressive strain acts in the opposite manner. The reducibility is expressed as the ratio of oxygen to metal vs the oxygen partial pressure, which is also shown in **Figure 8-5**. The experimental data lies between zero strain and 1% compressive strain. The presence of tensile strain significantly shifts the reducibility curve to a higher oxygen partial pressure (P_{O_2}) region. According to **Figure 8-2**, tensile strain lowers the formation energy of oxygen vacancy, which will lead to an easier reduction of ceria. Figure 5 also suggests that the non-stoichiometric sample is potentially under a compressive strain (less than 1%), which is consistent with the formation energy curve in **Figure 8-2**. In the experimental measurements, the samples were made up of large agglomerates of smaller crystallites. It likely that expansion of the individual crystallites upon reduction may have caused compressive strain in the sample. Moreover, the geometric and size effects in nanosized ceria can induce stress, which results in the change of the amount of oxygen vacancy. Our result may provide new perspectives to the previous understanding of the observed formation of reduced Ce(III) species in nanocrystalline CeO_2 with size dependence.[251,252] It should be noted that our model relies on the assumption that the oxygen vacancies are the dominant polarons in the regime where the small oxygen stoichiometric deviation cannot lead to phase transformation. It is worth pointing out that the dominant cations and anions may change due to the partial pressure of oxygen, therefore adjustment may be applied to this model for O_2-rich environment. Further, Mamontov *et al.* showed that nanocrystalline powders have a different defect profile, which could be a topic for future work.[253]

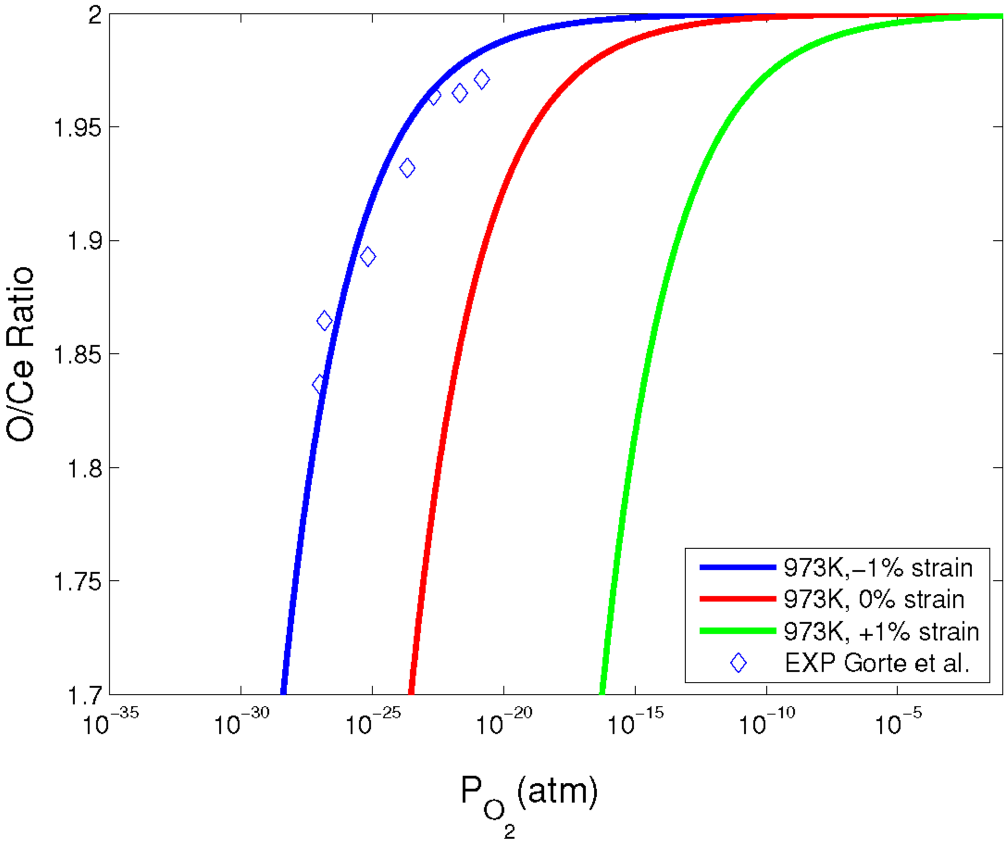

Figure 8-5 Non-stoichiometry of Ce$O_{2-\delta}$ at 1% compressive strain, 1% tensile strain, and 0% strain states at 973K versus oxygen partial pressure (P_{O_2}) compared to experiment data from Ref [267].

8.4 Conclusion

A continuum model informed by DFT simulations was developed to predict the chemical expansion in ceria as model system of non-stoichiometric oxides. The chemical expansion can be described by an elastic dipole tensor which is obtained by first principles calculations. The predicted chemical expansion agreed well with other simulations and experimental data, which demonstrates the validity of our approach. Finally, the calculated strain dependence of oxygen vacancy formation energy and the elastic dipole tensor can also predict reducibility of strained ceria. We predict that ceria can be reduced more easily in the presence of tensile strain. Our model provides a new understanding of electro-chemomechanical coupling for ceria as well as other nonstoichiometric materials.

Chapter 9 Concluding Remarks

This thesis was mainly focused on examining the possibility of using 2D materials in improving current energy applications, in particular, battery electrodes and hydrogen evolution reaction (HER) catalysts, and to elucidate the mechanisms and guiding principles in tuning 2D materials using combinatorial simulation techniques from different length scales.

First, we showed promising 2D material solutions to the electrodes in batteries beyond lithium that can possibly host many metal ions and enable high capacity and rate performances. In **Chapter 2**, we showed that MXenes can host Li, Na, K, Ca ions with a high capacity and a low diffusion barrier, enabling high-capacity electrode and high power density applications. The origin of such improvements is understood by carefully study the structural and electronic properties. Moreover, we introduced the first successful synthesis method of nitride MXenes, expanding the MXene library. In **Chapter 3** we showed that defective graphene and graphene allotropes provide a promising solution in Mg ion batteries with a capacity as high as 1042 mAh/g. These two chapters showed the possibility of improving the current battery performance by using 2D materials.

Next, we presented a new TMD family of 2D materials as an alternative to the current HER catalysts. In **Chapter 4**, we demonstrated that the previous-believed non-reactive 2H basal plane of MoS_2 monolayers can be activated by improving the electrical coupling between the substrate and the catalyst. Moreover, we identified the charge injection and the presence of naturally occurring vacancies are responsible to the observed increase in catalytic activity of the 2H basal plane. Based on this understanding, we demonstrated that the inherent structural asymmetry in the recently synthesized family of Janus TMDs can be a new means to stimulate HER activity in **Chapter 5**. The Janus WSSe system has been identified as a promising candidate, where the basal plane can be activated without large applied tensile strains and in the absence of significant density of vacancies. The enhanced HER catalytic activity is intrinsic and tunable, and we attribute it to the introduction of in-gap states and a shift in the Fermi level in hydrogen adsorbed systems due to Janus asymmetry. These two chapters provide a means to tune 2D TMD materials as a HER catalyst.

Finally, we generalized the method of DFT-informed multiscale modeling to several applications. The good agreement between experimental results and our predictions in the Moiré pattern in Graphene/h-BN heterostructures validated our multiscale method in **Chapter 6**. In **Chapter 7** we performed a theoretical study to understand the carrier mobility and photoconductivity on the structural and stacking sequence of a COF using DFT simulations. Our model not only explained conductivity enhancement mechanisms, but also provided guidelines in designing highly conductive 2D polymer optoelectronic devices. We then extended our multiscale method to determining the chemical expansion in non-stoichiometric oxides in **Chapter 8**. An elastic dipole tensor that describes the long-range elastic fields created upon formation of oxygen vacancies has been introduced to bridge different length scales. Our work provides an efficient way in computing chemo-mechanical coupling in oxides by introducing the elastic dipole.

In a broader context, 2D materials are emerging fast with surprising applications due to their unique mechanical, chemical, electronic, optical, and magnetic properties. This thesis adds some new understandings to current 2D materials not only by showing promising applications using current realized 2D materials but also inspiring experimentalists to search for new 2D material systems with novel structures, properties, and applications. Owing to the increase in the capacity of high-performance computing in the recent years, the computational simulations and multiscale models developed in this thesis can be better integrated into future exploration of materials in energy applications.

APPENDIX

A1. **First principles density functional theory methods**

Many simulation methods are semi-empirical before the development of first principles. They are quite successful in describing questions that have larger length and time scale. For example, the interparticle forces are typically formulated by analytical functions, known as potentials or force fields, which are capable reproducing experimental data or very accurate calculation results in research fields such as thermodynamics, crystal structures, defects, dislocations, and transport. They are very accurate in relative large scale (through in ~nm and ~ps frame); however, questions emerged in smaller quantum scale level call for more accurate solutions that can capture the physics with electronic interactions. In 2D materials, whose thickness is single or several atomic layers, a method originated from solving the quantum mechanics equations are preferred. Thanks to the dramatically developed computational power and density functional theory in the last half century, the first principles approach, or *ab initio*, are available nowadays. The key in quantum mechanically understand a system is solving the wave functions, ψ_n, and the corresponding eigenvalues, E_n.

A.1.1 Density functional theory

The difficulty in connecting quantum mechanics Schrödinger equations and real materials lies in: 1) in solids, electrons and nuclei form a large many-body system, in which the precise solution of the Schrödinger equation analytically or numerically without proper simplifications is not possible; 2) first principles approaches are accurate but very computationally expansive; 3) interactions between orbitals, electrons, and particles like lights are nonrival from the basic quantum mechanics. Therefore, first-principles especially density functional theory has been developed. The basic assumption that decouples electrons and nuclei due to their huge mass difference is the Born-Oppenheimer approximation

$$\hat{\mathcal{H}} = -\frac{1}{2}\sum_{i}\nabla_{\mathrm{i}}^{2} - \sum_{I}\sum_{i}\frac{Z_I}{|\boldsymbol{R}_I - \boldsymbol{r}_i|} + \frac{1}{2}\sum_{i}\sum_{j\neq i}\frac{1}{|\boldsymbol{r}_i - \boldsymbol{r}_j|} \tag{0-1}$$

where Z_I, $\boldsymbol{R}_I$, and $\boldsymbol{r}_i$ stands for the nuclear charge, nuclei positions, and electron positions. Because of the masses difference $m_I \gg m_i$, nuclei are considered fixed. This approximation enables a manageable solution to the $\psi_{\mathrm{n}}(\boldsymbol{r}_1, \boldsymbol{r}_2 \ldots \boldsymbol{r}_N)$, which is a complex function that depends on materials.

In 1965, Kohn and Sham pioneered in developing the density functional theory to accurately and effectively calculate the energy of many-electron systems.[46,47] The basic idea is that the ground state energy and the corresponding electron density $n(\boldsymbol{r})$ of a many-body system can be determined by solving an effective *one-electron* Schrödinger equation.

$$\hat{\mathcal{H}}_{eff}\psi_{i\sigma} = \varepsilon_{i\sigma}\psi_{i\sigma} \tag{0-2}$$

where i and σ labels are orbital and spin states due to the fact that electrons are fermion particles and the exchange of orbital and spin states results in Pauli repulsion.[254] The effective Hamiltonian can be expressed as

$$\hat{\mathcal{H}}_{eff} = -\frac{1}{2}\nabla^2 + V_{ext}(\boldsymbol{r}) + \int\frac{n(\boldsymbol{r}')}{|\boldsymbol{r} - \boldsymbol{r}'|}d\boldsymbol{r}' + V_{xc}(\boldsymbol{r}) \tag{0-3}$$

and

$$n(\boldsymbol{r}) = \sum_{i\sigma}|\psi_{i\sigma}(\boldsymbol{r})|^2 \tag{0-4}$$

where $V_{ext}(\boldsymbol{r})$ denotes the external field that the electron feels and $V_{xc}(\boldsymbol{r})$ is the exchange-correlation potential defined as $V_{xc}(\boldsymbol{r}) = \delta E_{xc}(\boldsymbol{r})/\delta\, n(\boldsymbol{r})$. Although this term constitutes a small fraction of the total energy, it is indeed the quantum mechanical version of the interaction energy that describing the boding between atoms and molecules. Therefore it is pivotal to find an accurate description of the E_{xc}, which is unknown and needs for approximations.

A.1.2 Exchange-correlation functionals

The simplest version in describing the E_{xc} is the local and semilocal functionals. The local density approximation (LDA) is the following:

$$E_{xc}^{app}[n(\boldsymbol{r})] = \int \mathcal{E}_{xc}^{app}(\boldsymbol{r})n(\boldsymbol{r})d\boldsymbol{r} \tag{0-5}$$

A uniformly distributed electron gas with density $n(\boldsymbol{r})$ is used to approximate the uniform part, known as local spin density (LSD). While in order to deal with the nonuniformity part in real materials, a semilocal approximation with the gradient of electron density $\nabla n(\boldsymbol{r})$ is applied.

$$E_{xc}^{GGA}[n(\boldsymbol{r})] = \int \left[\, \mathcal{E}_{xc}^{unif}(\boldsymbol{r}) + H(\nabla n(\boldsymbol{r}))\right] n(\boldsymbol{r})d\boldsymbol{r} \tag{0-6}$$

The generalized gradient approximation (GGA)[81] together with LDA works really well for equilibrium crystal systems that have slowly varying electron densities. However, these functionals cannot capture the long-range electronic correlations or dispersions. Therefore, some hybrid exchange functionals have been developed. These potentials consist of nonlocal Hartree-Fock (HF) term, local exchange energy, and semilocal correlations. The proportion of each term is determined empirically. Popular ones include: HSE[255] (25%

HF,75% PBE), B3LYP[256] (20% HF, 80% GGA+LDA), PBE0[257], meta GGA[258]. They are successful in dealing with strongly correlated systems such as transition metals containing *d* and *f* orbitals.

Another improvement has to be made on top of hybrid functionals in describing the long-range interactions such as dispersion forces and van der Waals (vdW) forces. The most straightforward way is to add the attractive energy term similar to the $1/r^6$ Lennard-Jones potential.

$$E_{disp} = -\sum_{i,j} \frac{C_{ij}}{r_{ij}^6} \tag{0-7}$$

This approximation is named DFT-D method. Refined versions such as DFT-D2,[259] DFT-D3,[260] DFT-TS[203] (which accounts for vdW) are indispensable tools in studying the role of interlayer interactions in 2D materials. Finally the exchange-correlation energy can be expressed as the summation of local, semilocal, and non-local terms.

$$E_{xc} = E_c^{LDA} + E_x^{GGA} + E_c^{nl} \tag{0-8}$$

A.1.3 Implementation in VASP

Many softwares are available for the implementation of DFT. In this thesis, all calculations are performed using the Vienna Ab Initio Simulation Package (VASP).[261] The workflow is shown in **Figure A-1a**. A typical VASP input requires the following input files: INCAR, KPOINTS, POSCAR, and POTCAR. The central input file is the INCAR file, where all parameters controlling what to do and how to do inside the software. A typical INCAR file is shown in **Figure A-1b.**

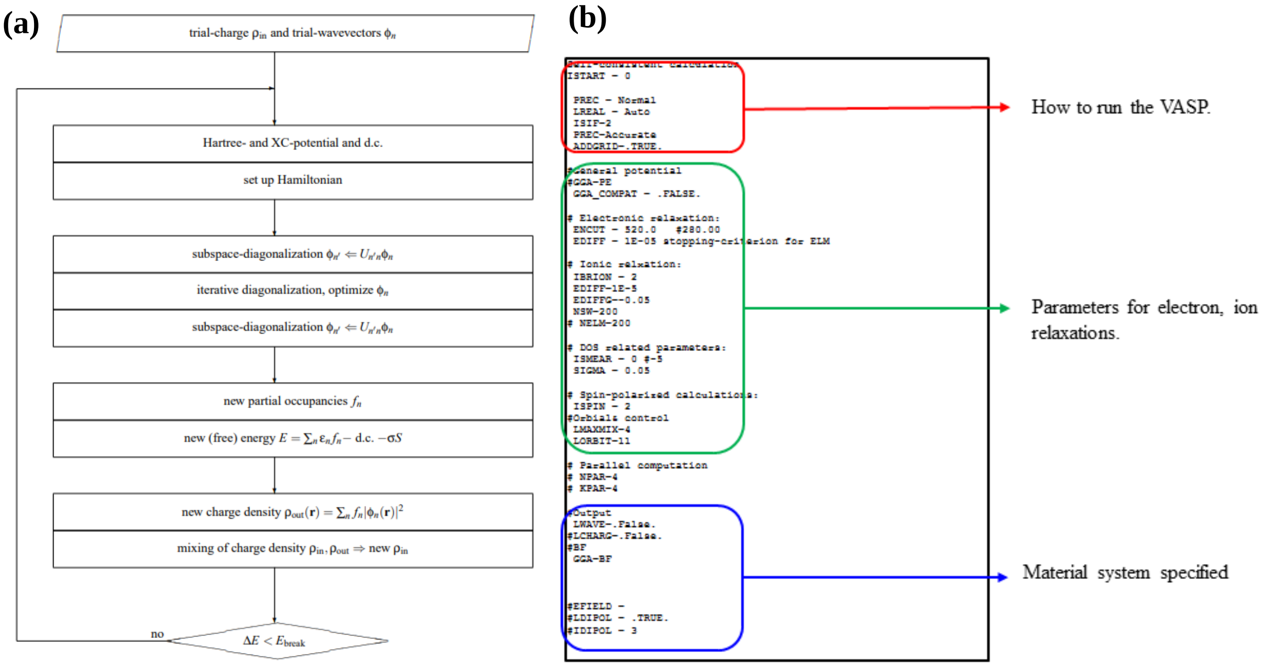

```
Self-consistent calculation
ISTART = 0

 PREC = Normal
 LREAL = Auto
 ISIF=2
 PREC=Accurate
 ADDGRID=.TRUE.

#General potential
#GGA=PE
 GGA_COMPAT = .FALSE.

# Electronic relaxation:
 ENCUT = 520.0   #280.00
 EDIFF = 1E-05 stopping-criterion for ELM

# Ionic relxation:
 IBRION = 2
 EDIFF=1E-5
 EDIFFG=-0.05
 NSW=200
# NELM=200

# DOS related parameters:
 ISMEAR = 0 #-5
 SIGMA = 0.05

# Spin-polarized calculations:
 ISPIN = 2
#Orbials control
 LMAXMIX=4
 LORBIT=11

# Parallel computation
# NPAR=4
# KPAR=4

#Output
 LWAVE=.False.
#LCHARG=.False.
#BF
 GGA=BF



#EFIELD =
#LDIPOL = .TRUE.
#IDIPOL = 3
```

Figure A-1 (a) Work flow of VASP calculation of KS-ground-state. **(b)** A typical INCAR file.

A2. **Experimental details of MXene synthesis**

A.2.1 Carbide Ti_3C_2 MXene

Powder of Ti_3AlC_2 was prepared by ball-milling Ti_2AlC (> 92 wt%, 3-ONE-2, Voorhees, NJ) and TiC (99%, Johnson Matthey Electronic, NY) powders in a 1:1 molar ratio for 24 h using zirconia balls. The mixture was heated to 1350 ° C for 2 h under argon, Ar. The resulting loosely held compact was crushed using a mortar and pestle. Roughly 10 g of powders are then immersed in ≈ 100 mL of a 50% concentrated HF solution (Fisher Scientific, Fair Lawn, NJ) at room temperature for 2 h. The resulting suspension was then washed several times using deionized water and centrifuged to separate the powders. In some cases, to align the flakes and produce free-standing discs, the treated powders were cold pressed at a load corresponding to a stress of 1 GPa in a steel die. From Ref. 58.

A.2.2 Nitride Ti_4N_3 MXene

MXenes have a layered hexagonal crystal structure with P63/mmc symmetry, where M layers are nearly closed packed and X atoms fill the octahedral sites. The precursor Ti_4AlN_3, MAX phase, was produced by mixing TiH_2 (TIMET, Henderson, NV; 99.3 % -325 mesh), AlN (Alfa Aesar, Ward Hill, MA; N 32.0 % minimum, 2.5 to 4.0 µm), and TiN (Alfa Aesar, Ward Hill, MA; 99.8 %, 2 to 5 µm) powders with a molar ratio of 2 : 1 : 2. These powders were ball milled for 14 h and hot pressed for 24 h at 1275 °C and 70 MPa. The resulting Ti_4AlN_3 block was then milled using a drill bit and sieved through a 400 mesh, producing a powder with particles smaller than 37 µm. The fluoride salt was a mixture of potassium fluoride (KF), lithium fluoride (LiF) (98.5 %, -325 mesh), and sodium fluoride (NaF) (all Alfa Aesar, Ward Hill, MA) with a mass ratio of 0.59 : 0.29 : 0.12, respectively, chosen because this is the eutectic composition of these salts, which allows for this treatment to be performed at lower temperature. The Ti_4AlN_3 was then mixed with the fluoride salt mixture in a 1 : 1 mass ratio and ball milled for 6 h. The mixture, a 2 g batch of Ti_4AlN_3 and fluoride salt, was then placed into an alumina crucible. Unlike in previous methods of heating MAX phases in molten salt in air, this treatment was performed in Ar. The treatment was performed at 550 °C for 30 min, with heating and cooling rates of 10 °C/min.

After the molten salt treatment, XRD detected the several fluorides including cryolite (Na_3AlF_6) and other similar Al-containing fluorides: K_2NaAlF_6, K_3AlF_6, AlF_3 and $LiNa_2AlF_6$. Diluted sulfuric acid (H_2SO_4) (Fisher Scientific, Fair Lawn, NJ; > 95 %) was used to remove these compounds present in the Ti_4N_3 product, since cryolite is soluble in

H_2SO_4. This was done by washing the nitride and salt mixture in 8M H_2SO_4 for 1 h with stirring with a magnetic Teflon coated bar in a ratio of 10 mL 8 M H_2SO_4 : 1 g Ti_4N_3-fluoride mixture. The mixture was then rinsed with deionized (DI) water, centrifuged at 3,500 rpm for 2 min and decanted to separate and dispose of the acid. Rinsing with DI water and centrifuging was repeated until the supernatant liquid in the centrifuge tube had a pH of at least 6. After the last decanting the sediment was then filtered on a polypropylene membrane (3501 Coated PP, Celgard LLC, Charlotte, NC) and will henceforth be referred to as multilayered Ti_4N_3.

To delaminate the multilayered MXene into few-layer and monolayer flakes, the powder was mixed with 40 wt.% tetrabutylammonium hydroxide (TBAOH) (Acros Organics, Morris Plains, NJ; 40% in water) in a ratio of 10 mL TBAOH : 1 g Ti_4N_3 by hand-shaking for 5 min. This procedure has been applied to other MXene systems for this purpose. To separate and remove the TBAOH, the powder was then washed with DI water and centrifuged at 3,500 rpm for 5 min and the supernatant was decanted to remove the residual TBAOH. After that, DI water was added to the residue Ti_4N_3 powder and probe sonicated for 30 min. To separate the smaller delaminated Ti_4N_3 flakes, this suspension was centrifuged at 5,000 rpm for 15 min, and the supernatant suspension was filtered onto a polypropylene membrane to collect these flakes. Theses flakes are henceforth referred to as delaminated Ti_4N_3 From Ref. 45.

BIBLIOGRAPHY

(1) International Energy Outlook 2017 https://www.eia.gov/outlooks/ieo/pdf/0484(2017).pdf.

(2) Annual Energy Outlook 2018 with projections to 2050 https://www.eia.gov/outlooks/aeo/pdf/AEO2018.pdf (accessed Apr 6, 2018).

(3) Whittingham, M. S. History, Evolution, and Future Status of Energy Storage. *Proc. IEEE* **2012**, *100*, 1518–1534.

(4) Goodenough, J. B.; Kim, Y. Challenges for Rechargeable Li Batteries. *Chem. Mater.* **2010**, *22*, 587–603.

(5) Chu, S.; Cui, Y.; Liu, N. The Path towards Sustainable Energy. *Nat. Mater.* **2017**, *16*, 16–22.

(6) Laursen, A. B.; Kegnæs, S.; Dahl, S.; Chorkendorff, I. Molybdenum Sulfides—efficient and Viable Materials for Electro - and Photoelectrocatalytic Hydrogen Evolution. *Energy Environ. Sci.* **2012**, *5*, 5577.

(7) Morales-Guio, C. G.; Hu, X. Amorphous Molybdenum Sulfides as Hydrogen Evolution Catalysts. *Acc. Chem. Res.* **2014**, *47*, 2671–2681.

(8) Chhowalla, M.; Shin, H. S.; Eda, G.; Li, L. J.; Loh, K. P.; Zhang, H. The Chemistry of Two-Dimensional Layered Transition Metal Dichalcogenide Nanosheets. *Nat. Chem.* **2013**, *5*, 263–275.

(9) Callejas, J. F.; Read, C. G.; Roske, C. W.; Lewis, N. S.; Schaak, R. E. Synthesis, Characterization, and Properties of Metal Phosphide Catalysts for the Hydrogen-Evolution Reaction. *Chem. Mater.* **2016**, *28*, 6017–6044.

(10) Popczun, E. J.; McKone, J. R.; Read, C. G.; Biacchi, A. J.; Wiltrout, A. M.; Lewis, N. S.; Schaak, R. E. Nanostructured Nickel Phosphide as an Electrocatalyst for the Hydrogen Evolution Reaction. *J. Am. Chem. Soc.* **2013**, *135*, 9267–9270.

(11) Zeng, M.; Li, Y. Recent Advances in Heterogeneous Electrocatalysts for the Hydrogen Evolution Reaction. *J. Mater. Chem. A* **2015**, *3*, 14942–14962.

(12) Faber, M. S.; Jin, S. Earth-Abundant Inorganic Electrocatalysts and Their Nanostructures for Energy Conversion Applications. *Energy Environ. Sci.* **2014**, *7*, 3519–3542.

(13) Cabán-Acevedo, M.; Stone, M. L.; Schmidt, J. R.; Thomas, J. G.; Ding, Q.; Chang, H.-C.; Tsai, M.-L.; He, J.-H.; Jin, S. Efficient Hydrogen Evolution Catalysis Using Ternary Pyrite-Type Cobalt Phosphosulphide. *Nat. Mater.* **2015**, *14*, 1245–1251.

(14) Vesborg, P. C. K.; Seger, B.; Chorkendorff, I. Recent Development in Hydrogen Evolution Reaction Catalysts and Their Practical Implementation. *J. Phys. Chem. Lett.* **2015**, *6*, 951–957.

(15) Novoselov, K. S.; Falʹko, V. I.; Colombo, L.; Gellert, P. R.; Schwab, M. G.; Kim, K. A Roadmap for Graphene. *Nature* **2012**, *490*, 192–200.

(16) Geim, A. K.; Novoselov, K. S. The Rise of Graphene. *Nat. Mater.* **2007**, *6*, 183–191.

(17) Novoselov, K. S.; Geim, A. K.; Morozov, S. V; Jiang, D.; Zhang, Y.; Dubonos, S. V; Grigorieva, I. V; Firsov, A. A. Electric Field Effect in Atomically Thin Carbon Films. *Science (80-.).* **2004**, *306*, 666–669.

(18) Novoselov, K. S.; Jiang, D.; Schedin, F.; Booth, T. J.; Khotkevich, V. V; Morozov, S. V; Geim, a K. Two-Dimensional Atomic Crystals. *Proc. Natl. Acad. Sci. U. S. A.* **2005**, *102*, 10451–10453.

(19) Geim, A. K.; Grigorieva, I. V. Van Der Waals Heterostructures. *Nature* **2013**, *499*, 419–425.

(20) Mak, K. F.; Lee, C.; Hone, J.; Shan, J.; Heinz, T. F. Atomically Thin MoS2: A New Direct-Gap Semiconductor. *Phys. Rev. Lett.* **2010**, *105*, 136805.

(21) Voiry, D.; Salehi, M.; Silva, R.; Fujita, T.; Chen, M.; Asefa, T.; Shenoy, V. B.; Eda, G.; Chhowalla, M. Conducting MoS 2 Nanosheets as Catalysts for Hydrogen Evolution Reaction. *Nano Lett.* **2013**, *13*, 6222–6227.

(22) Voiry, D.; Fullon, R.; Yang, J.; de Carvalho Castro e Silva, C.; Kappera, R.; Bozkurt, I.; Kaplan, D.; Lagos, M. J.; Batson, P. E.; Gupta, G.; *et al.* The Role of Electronic Coupling between Substrate and 2D MoS2 Nanosheets in Electrocatalytic Production of Hydrogen. *Nat. Mater.* **2016**, *15*, 1003–1009.

(23) Li, H.; Tsai, C.; Koh, A. L.; Cai, L.; Contryman, A. W.; Fragapane, A. H.; Zhao, J.; Han, H. S.; Manoharan, H. C.; Abild-Pedersen, F.; *et al.* Activating and Optimizing MoS2 Basal Planes for Hydrogen Evolution through the Formation of Strained Sulphur Vacancies. *Nat. Mater.* **2016**, *15*, 48–53.

(24) Butler, S. Z.; Hollen, S. M.; Cao, L.; Cui, Y.; Gupta, J. A.; Gutiérrez, H. R.; Heinz, T. F.; Hong, S. S.; Huang, J.; Ismach, A. F.; *et al.* Progress, Challenges, and Opportunities in Two-Dimensional Materials beyond Graphene. *ACS Nano* **2013**, *7*, 2898–2926.

(25) Goodenough, J. B.; Park, K. S. The Li-Ion Rechargeable Battery: A Perspective. *J. Am. Chem. Soc.* **2013**, *135*, 1167–1176.

(26) Yoshino, A.; Sanechika, K.; Nakajima, T. Secondary Battery. 1989293, 1985.

(27) Yoshino, A. The Birth of the Lithium-Ion Battery. *Angew. Chem. Int. Ed. Engl.* **2012**, *51*, 5798–5800.

(28) Tarascon, J. M.; Armand, M. Issues and Challenges Facing Rechargeable Lithium Batteries. *Nature* **2001**, *414*, 359–367.

(29) Lu, L.; Han, X.; Li, J.; Hua, J.; Ouyang, M. A Review on the Key Issues for Lithium-Ion Battery Management in Electric Vehicles. *J. Power Sources* **2013**, *226*, 272–288.

(30) Nitta, N.; Yushin, G. High-Capacity Anode Materials for Lithium-Ion Batteries: Choice of Elements and Structures for Active Particles. *Part. Part. Syst. Charact.* **2014**, *31*, 317–336.

(31) Chan, C. C.; Wong, Y. S. Electric Vehicles Charge Forward. *IEEE Power Energy Mag.* **2004**, *2*, 24–33.

(32) Brandmeyer;, J. E.; Frechtel, P.; Byron, M. Z.; Elkins, J.; Hemby, J.; Rao, V. Trends in Monitored Concentrations of Carbon Monoxide. *Natl. Air Qual. Emiss. Trends Rep.* **2003**, 25–33.

(33) Lewis, N. S. Powering the Planet. *MRS Bull.* **2007**, *32*, 808.

(34) Lewis, N. S.; Nocera, D. G. Powering the Planet: Chemical Challenges in Solar Energy Utilization. *Proc. Natl. Acad. Sci.* **2006**, *103*, 15729–15735.

(35) Turner, J. A. Sustainable Hydrogen Production. *Science (80-.).* **2004**, *305*, 972–974.

(36) Chu, S.; Majumdar, A. Opportunities and Challenges for a Sustainable Energy Future. *Nature* **2012**, *488*, 294–303.

(37) Ding, Q.; Song, B.; Xu, P.; Jin, S. Efficient Electrocatalytic and Photoelectrochemical Hydrogen Generation Using MoS 2 and Related Compounds. *Chem* **2016**, *1*, 699–726.

(38) Jaramillo, T. F.; Jorgensen, K. P.; Bonde, J.; Nielsen, J. H.; Horch, S.; Chorkendorff, I. Identification of Active Edge Sites for Electrochemical H2 Evolution from MoS2 Nanocatalysts. *Science (80-.).* **2007**, *317*, 100–102.

(39) Kappera, R.; Voiry, D.; Yalcin, S. E.; Branch, B.; Gupta, G.; Mohite, A. D.; Chhowalla, M. Phase-Engineered Low-Resistance Contacts for Ultrathin MoS2 Transistors. *Nat. Mater.* **2014**, *13*, 1–7.

(40) Voiry, D.; Yamaguchi, H.; Li, J.; Silva, R.; Alves, D. C. B.; Fujita, T.; Chen, M.; Asefa, T.; Shenoy, V. B.; Eda, G.; *et al.* Enhanced Catalytic Activity in Strained Chemically Exfoliated WS2 Nanosheets for Hydrogen Evolution. *Nat. Mater.* **2013**, *12*, 850–855.

(41) Walter, M. G.; Warren, E. L.; McKone, J. R.; Boettcher, S. W.; Mi, Q.; Santori, E. a.; Lewis, N. S. Solar Water Splitting Cells. *Chem. Rev.* **2010**, *110*, 6446–6473.

(42) Novoselov, K. S.; Mishchenko, A.; Carvalho, A.; Castro Neto, A. H. 2D Materials and van Der Waals Heterostructures. *Science.* **2016**, *353*, aac9439.

(43) Zhang, J.; Jia, S.; Kholmanov, I.; Dong, L.; Er, D.; Chen, W.; Guo, H.; Jin, Z.; Shenoy, V. B.; Shi, L.; *et al.* Janus Monolayer Transition-Metal Dichalcogenides. *ACS Nano* **2017**, *11*, 8192–8198.

(44) Lu, A.-Y.; Zhu, H.; Xiao, J.; Chuu, C.-P.; Han, Y.; Chiu, M.-H.; Cheng, C.-C.; Yang, C.-W.; Wei, K.-H.; Yang, Y.; *et al.* Janus Monolayers of Transition Metal Dichalcogenides. *Nat. Nanotechnol.* **2017**, *12*, 744–749.

(45) Urbankowski, P.; Anasori, B.; Makaryan, T.; Er, D.; Kota, S.; Walsh, P. L.; Zhao, M.; Shenoy, V. B.; Barsoum, M. W.; Gogotsi, Y. Synthesis of Two-Dimensional Titanium Nitride Ti 4 N 3 (MXene). *Nanoscale* **2016**, *8*, 11385–11391.

(46) Kohn, W.; Sham, L. J. Self-Consistent Equations Including Exchange and Correlation Effects. *Phys. Rev.* **1965**, *140*, A1133–A1138.

(47) Sham, L. J.; Kohn, W. One-Particle Properties of an Inhomogeneous Interacting Electron Gas. *Phys. Rev.* **1966**, *145*, 561–567.

(48) Ceder, G. Opportunities and Challenges for First-Principles Materials Design and Applications to Li Battery Materials. *MRS Bull.* **2010**, *35*, 693–701.

(49) Nørskov, J. K.; Bligaard, T.; Rossmeisl, J.; Christensen, C. H. Towards the Computational Design of Solid Catalysts. *Nat. Chem.* **2009**, *1*, 37–46.

(50) Dunn, B.; Kamath, H.; Tarascon, J.-M. Electrical Energy Storage for the Grid: A Battery of Choices. *Science (80-.).* **2011**, *334*, 928–935.

(51) Chen, H.; Cong, T. N.; Yang, W.; Tan, C.; Li, Y.; Ding, Y. Progress in Electrical Energy Storage System: A Critical Review. *Prog. Nat. Sci.* **2009**, *19*, 291–312.

(52) Slater, M. D.; Kim, D.; Lee, E.; Johnson, C. S. Sodium-Ion Batteries. *Adv. Funct. Mater.* **2013**, *23*, 947–958.

(53) Pan, H.; Hu, Y.-S.; Chen, L. Room-Temperature Stationary Sodium-Ion Batteries for Large-Scale Electric Energy Storage. *Energy Environ. Sci.* **2013**, *6*, 2338.

(54) Eftekhari, A. Potassium Secondary Cell Based on Prussian Blue Cathode. *J. Power Sources* **2004**, *126*, 221–228.

(55) DiVincenzo, D. P.; Mele, E. J. Cohesion and Structure in Stage-1 Graphite Intercalation Compounds. *Phys. Rev. B* **1985**, *32*, 2538–2553.

(56) Datta, D.; Li, J.; Koratkar, N.; Shenoy, V. B. Enhanced Lithiation in Defective Graphene. *Carbon N. Y.* **2014**, *80*, 305–310.

(57) Naguib, M.; Mashtalir, O.; Carle, J.; Presser, V.; Lu, J.; Hultman, L.; Gogotsi, Y.; Barsoum, M. W. Two-Dimensional Transition Metal Carbides. *ACS Nano* **2012**, *6*, 1322–1331.

(58) Naguib, M.; Kurtoglu, M.; Presser, V.; Lu, J.; Niu, J.; Heon, M.; Hultman, L.; Gogotsi, Y.; Barsoum, M. W. Two-Dimensional Nanocrystals Produced by Exfoliation of Ti3AlC2. *Adv. Mater.* **2011**, *23*, 4248–4253.

(59) Barsoum, M. W. The MN+1AXN Phases: A New Class of Solids. *Prog. Solid State Chem.* **2000**, *28*, 201–281.

(60) Sun, Z.; Music, D.; Ahuja, R.; Li, S.; Schneider, J. M. Bonding and Classification of Nanolayered Ternary Carbides. *Phys. Rev. B* **2004**, *70*, 92102.

(61) Ghidiu, M.; Lukatskaya, M. R.; Zhao, M.-Q.; Gogotsi, Y.; Barsoum, M. W. Conductive Two-Dimensional Titanium Carbide “clay” with High Volumetric Capacitance. *Nature* **2014**.

(62) Halim, J.; Lukatskaya, M. R.; Cook, K. M.; Lu, J.; Smith, C. R.; Näslund, L.-Å.; May, S. J.; Hultman, L.; Gogotsi, Y.; Eklund, P.; *et al.* Transparent Conductive Two-Dimensional Titanium Carbide Epitaxial Thin Films. *Chem. Mater.* **2014**, *26*, 2374–2381.

(63) Anasori, B.; Lukatskaya, M. R.; Gogotsi, Y. 2D Metal Carbides and Nitrides (MXenes) for Energy Storage. *Nat. Rev. Mater.* **2017**, *2*, 16098.

(64) Anasori, B.; Xie, Y.; Beidaghi, M.; Lu, J.; Hosler, B. C.; Hultman, L.; Kent, P. R. C.; Gogotsi, Y.; Barsoum, M. W. Two-Dimensional, Ordered, Double Transition Metals Carbides (MXenes). *ACS Nano* **2015**, *9*, 9507–9516.

(65) Naguib, M.; Halim, J.; Lu, J.; Cook, K. M.; Hultman, L.; Gogotsi, Y.; Barsoum, M. W. New Two-Dimensional Niobium and Vanadium Carbides as Promising Materials for Li-Ion Batteries. *J. Am. Chem. Soc.* **2013**, *135*, 15966–15969.

(66) Shein, I. R.; Ivanovskii, A. L. Planar Nano-Block Structures Tin+1Al0.5Cn and Tin+1Cn (n=1, and 2) from MAX Phases: Structural, Electronic Properties and Relative Stability from First Principles Calculations. *Superlattices Microstruct.* **2012**, *52*, 147–157.

(67) Shein, I. R.; Ivanovskii, A. L. Graphene-like Titanium Carbides and Nitrides Tin+1Cn, Tin+1Nn (n=1, 2, and 3) from de-Intercalated MAX Phases: First-Principles Probing of Their Structural, Electronic Properties and Relative Stability. *Comput. Mater. Sci.* **2012**, *65*, 104–114.

(68) Khazaei, M.; Arai, M.; Sasaki, T.; Chung, C.-Y.; Venkataramanan, N. S.; Estili, M.; Sakka, Y.; Kawazoe, Y. Novel Electronic and Magnetic Properties of Two-Dimensional Transition Metal Carbides and Nitrides. *Adv. Funct. Mater.* **2013**, *23*, 2185–2192.

(69) Xie, Y.; Kent, P. R. C. Hybrid Density Functional Study of Structural and Electronic

Properties of Functionalized Ti_{n+1}X_{n} (X=C, N) Monolayers. *Phys. Rev. B* **2013**, *87*, 235441.

(70) Kurtoglu, M.; Naguib, M.; Gogotsi, Y.; Barsoum, M. W. First Principles Study of Two-Dimensional Early Transition Metal Carbides. *MRS Commun.* **2012**, *2*, 133–137.

(71) Naguib, M.; Come, J.; Dyatkin, B.; Presser, V.; Taberna, P.-L.; Simon, P.; Barsoum, M. W.; Gogotsi, Y. MXene: A Promising Transition Metal Carbide Anode for Lithium-Ion Batteries. *Electrochem. commun.* **2012**, *16*, 61–64.

(72) Mashtalir, O.; Naguib, M.; Mochalin, V. N.; Dall'Agnese, Y.; Heon, M.; Barsoum, M. W.; Gogotsi, Y. Intercalation and Delamination of Layered Carbides and Carbonitrides. *Nat. Commun.* **2013**, *4*, 1716.

(73) Come, J.; Naguib, M.; Rozier, P.; Barsoum, M. W.; Gogotsi, Y.; Taberna, P.-L.; Morcrette, M.; Simon, P. A Non-Aqueous Asymmetric Cell with a Ti2C-Based Two-Dimensional Negative Electrode. *J. Electrochem. Soc.* **2012**, *159*, A1368–A1373.

(74) Tang, Q.; Zhou, Z.; Shen, P. Are MXenes Promising Anode Materials for Li Ion Batteries? Computational Studies on Electronic Properties and Li Storage Capability of Ti3C2 and Ti3C2X2 (X = F, OH) Monolayer. *J. Am. Chem. Soc.* **2012**, *134*, 16909–16916.

(75) Zhong, Y.; Xia, X.; Shi, F.; Zhan, J.; Tu, J.; Fan, H. J. Transition Metal Carbides and Nitrides in Energy Storage and Conversion. *Adv. Sci.* **2016**, *3*, 1500286.

(76) Naguib, M.; Mochalin, V. N.; Barsoum, M. W.; Gogotsi, Y. 25th Anniversary Article: MXenes: A New Family of Two-Dimensional Materials. *Adv. Mater.* **2014**, *26*, 992–1005.

(77) Ye, Q.; Xiao, P.; Liu, W.; Chen, K.; Chen, T.; Xue, J.; Du, S.; Huang, Q. Exploring the Potential of Exfoliated Ternary Ultrathin Ti 4 AlN 3 Nanosheets for Fabricating Hybrid Patterned Polymer Brushes. *RSC Adv.* **2015**, *5*, 70339–70344.

(78) Kresse, G.; Hafner, J. Ab Initio Molecular Dynamics for Liquid Metals. *Phys. Rev. B* **1993**, *47*, 558–561.

(79) Kresse, G.; Furthmüller, J. Efficient Iterative Schemes for Ab Initio Total-Energy Calculations Using a Plane-Wave Basis Set. *Phys. Rev. B* **1996**, *54*, 11169–11186.

(80) Blöchl, P. E. Projector Augmented-Wave Method. *Phys. Rev. B* **1994**, *50*, 17953–17979.

(81) Perdew, J.; Burke, K.; Ernzerhof, M. Generalized Gradient Approximation Made Simple. *Phys. Rev. Lett.* **1996**, *77*, 3865–3868.

(82) Aydinol, M. K.; Kohan, A. F.; Ceder, G.; Cho, K.; Joannopoulos, J. Ab Initio Study of Lithium Intercalation in Metal Oxides and Metal Dichalcogenides. *Phys. Rev. B* **1997**, *56*, 1354–1365.

(83) Mills, G.; Jónsson, H.; Schenter, G. K. Reversible Work Transition State Theory: Application to Dissociative Adsorption of Hydrogen. *Surf. Sci.* **1995**, *324*, 305–337.

(84) Chan, K. T.; Neaton, J. B.; Cohen, M. L. First-Principles Study of Metal Adatom Adsorption on Graphene. *Phys. Rev. B* **2008**, *77*, 235430.

(85) Lee, E.; Persson, K. a. Li Absorption and Intercalation in Single Layer Graphene and Few Layer Graphene by First Principles. *Nano Lett.* **2012**, *12*, 4624–4628.

(86) Mohtadi, R.; Mizuno, F. Magnesium Batteries: Current State of the Art, Issues and Future Perspectives. *Beilstein Journal of Nanotechnology*, 2014, *5*, 1291–1311.

(87) Hu, J.; Xu, B.; Yang, S. A.; Guan, S.; Ouyang, C.; Yao, Y. 2D Electrides as Promising Anode Materials for Na-Ion Batteries from First-Principles Study. *ACS Appl. Mater. Interfaces* **2015**, *7*, 24016–24022.

(88) Jing, Y.; Zhou, Z.; Cabrera, C. R.; Chen, Z. Metallic VS 2 Monolayer: A Promising 2D Anode Material for Lithium Ion Batteries. *J. Phys. Chem. C* **2013**, *117*, 25409–25413.

(89) Kang, J.; Li, J.; Li, S.-S.; Xia, J.-B.; Wang, L.-W. Electronic Structural Moiré Pattern Effects on MoS2/MoSe2 2D Heterostructures. *Nano Lett.* **2013**, *13*, 5485–5490.

(90) Er, D.; Li, J.; Naguib, M.; Gogotsi, Y.; Shenoy, V. B. Ti 3 C 2 MXene as a High Capacity Electrode Material for Metal (Li, Na, K, Ca) Ion Batteries. *ACS Appl. Mater. Interfaces* **2014**, *6*, 11173–11179.

(91) Liu, Y.; Artyukhov, V. I.; Liu, M.; Harutyunyan, A. R.; Yakobson, B. I. Feasibility of Lithium Storage on Graphene and Its Derivatives. *J. Phys. Chem. Lett.* **2013**, *4*, 1737–1742.

(92) Castro Neto, A. H.; Guinea, F.; Peres, N. M. R.; Novoselov, K. S.; Geim, A. K. The Electronic Properties of Graphene. *Rev. Mod. Phys.* **2009**, *81*, 109–162.

(93) Mukherjee, R.; Thomas, A. V; Datta, D.; Singh, E.; Li, J.; Eksik, O.; Shenoy, V. B.; Koratkar, N. Defect-Induced Plating of Lithium Metal within Porous Graphene Networks. *Nat. Commun.* **2014**, *5*, 3710.

(94) Datta, D.; Li, J.; Shenoy, V. B. Defective Graphene as a High-Capacity Anode Material for Na- and Ca-Ion Batteries. *ACS Appl. Mater. Interfaces* **2014**, *6*, 1788–1795.

(95) Zhang, P.; Crespi, V. H.; Chang, E.; Louie, S. G.; Cohen, M. L. Computational Design of Direct-Bandgap Semiconductors That Lattice-Match Silicon. *Nature* **2001**, *409*, 69–71.

(96) Lusk, M. T.; Carr, L. D. Creation of Graphene Allotropes Using Patterned Defects. *Carbon N. Y.* **2009**, *47*, 2226–2232.

(97) Enyashin, A. N.; Ivanovskii, A. L. Graphene Allotropes. *Phys. status solidi* **2011**, *248*, 1879–1883.

(98) Lusk, M. T.; Carr, L. D. Nanoengineering Defect Structures on Graphene. *Phys. Rev. Lett.* **2008**, *100*, 1–4.

(99) Kotakoski, J.; Krasheninnikov, A. V.; Kaiser, U.; Meyer, J. C. From Point Defects in Graphene to Two-Dimensional Amorphous Carbon. *Phys. Rev. Lett.* **2011**, *106*, 105505.

(100) Appelhans, D. J.; Carr, L. D.; Lusk, M. T. Embedded Ribbons of Graphene Allotropes: An Extended Defect Perspective. *New J. Phys.* **2010**, *12*, 125006.

(101) Sharma, B. R.; Manjanath, A.; Singh, A. K. Pentahexoctite: A New Two-Dimensional Allotrope of Carbon. *Sci. Rep.* **2014**, *4*, 7164.

(102) Kim, B. G.; Choi, H. J. Graphyne: Hexagonal Network of Carbon with Versatile Dirac Cones. *Phys. Rev. B - Condens. Matter Mater. Phys.* **2012**, *86*, 1–5.

(103) Li, G.; Li, Y. Y. Y.; Liu, H.; Guo, Y.; Li, Y. Y. Y.; Zhu, D. Architecture of

Graphdiyne Nanoscale Films. *Chem. Commun.* **2010**, *46*, 3256.

(104) Yang, N.; Liu, Y.; Wen, H.; Tang, Z.; Zhao, H.; Li, Y.; Wang, D. Photocatalytic Properties of Graphdiyne and Graphene Modified TiO 2 : From Theory to Experiment. *ACS Nano* **2013**, *7*, 1504–1512.

(105) Meyer, J. C.; Kisielowski, C.; Erni, R.; Rossell, M. D.; Crommie, M. F.; Zettl, A. Direct Imaging of Lattice Atoms and Topological Defects in Graphene Membranes. *Nano Lett.* **2008**, *8*, 3582–3586.

(106) Robertson, A. W.; Montanari, B.; He, K.; Allen, C. S.; Wu, Y. a.; Harrison, N. M.; Kirkland, A. I.; Warner, J. H. Structural Reconstruction of the Graphene Monovacancy. *ACS Nano* **2013**, *7*, 4495–4502.

(107) Ugeda, M. M.; Brihuega, I.; Guinea, F.; Gómez-Rodríguez, J. M. Missing Atom as a Source of Carbon Magnetism. *Phys. Rev. Lett.* **2010**, *104*, 1–4.

(108) Li, L.; Reich, S.; Robertson, J. Defect Energies of Graphite: Density-Functional Calculations. *Phys. Rev. B - Condens. Matter Mater. Phys.* **2005**, *72*, 1–10.

(109) Thrower, P. A.; Mayer, R. M. Point Defects and Self-Diffusion in Graphite. *Phys. Status Solidi* **1978**, *47*, 11–37.

(110) Lahiri, J.; Lin, Y.; Bozkurt, P.; Oleynik, I. I.; Batzill, M. An Extended Defect in Graphene as a Metallic Wire. *Nat. Nanotechnol.* **2010**, *5*, 326–329.

(111) Kotakoski, J.; Meyer, J. C.; Kurasch, S.; Santos-Cottin, D.; Kaiser, U.; Krasheninnikov, A. V. Stone-Wales-Type Transformations in Carbon Nanostructures Driven by Electron Irradiation. *Phys. Rev. B* **2011**, *83*, 245420.

(112) Stone, A. J.; Wales, D. J. Theoretical Studies of Icosahedral C60 and Some Related Species. *Chem. Phys. Lett.* **1986**, *128*, 501–503.

(113) Terrones, H.; Terrones, M.; Hernández, E.; Grobert, N.; Charlier, J.-C.; Ajayan, P. M. New Metallic Allotropes of Planar and Tubular Carbon. *Phys. Rev. Lett.* **2000**, *84*, 1716–1719.

(114) Banhart, F.; Kotakoski, J.; Krasheninnikov, A. V. Structural Defects in Graphene. *ACS Nano* **2011**, *5*, 26–41.

(115) Long, M.; Tang, L.; Wang, D.; Li, Y.; Shuai, Z. Electronic Structure and Carrier Mobility in Graphdiyne Sheet and Nanoribbons: Theoretical Predictions. *ACS Nano* **2011**, *5*, 2593–2600.

(116) Baughman, R. H.; Eckhardt, H.; Kertesz, M. Structure-Property Predictions for New Planar Forms of Carbon: Layered Phases Containing sp2 and Sp Atoms. *J. Chem. Phys.* **1987**, *87*, 6687.

(117) Malko, D.; Neiss, C.; Viñes, F.; Görling, A. Competition for Graphene: Graphynes with Direction-Dependent Dirac Cones. *Phys. Rev. Lett.* **2012**, *108*, 86804.

(118) Song, Q.; Wang, B.; Deng, K.; Feng, X.; Wagner, M.; Gale, J. D.; Müllen, K.; Zhi, L. Graphenylene, a Unique Two-Dimensional Carbon Network with Nondelocalized Cyclohexatriene Units. *J. Mater. Chem. C* **2013**, *1*, 1–5.

(119) Yu, Y.-X. Graphenylene: A Promising Anode Material for Lithium-Ion Batteries with High Mobility and Storage. *J. Mater. Chem. A* **2013**, *1*, 13559.

(120) Hudspeth, M. A.; Whitman, B. W.; Barone, V.; Peralta, J. E. Electronic Properties of the Biphenylene Sheet and Its One-Dimensional Derivatives. *ACS Nano* **2010**, *4*, 4565–4570.

(121) Tang, W.; Sanville, E.; Henkelman, G. A Grid-Based Bader Analysis Algorithm without Lattice Bias. *J. Phys. Condens. Matter* **2009**, *21*, 84204.

(122) Liang, Y.; Yoo, H. D.; Li, Y.; Shuai, J.; Calderon, H. A.; Robles Hernandez, F. C.; Grabow, L. C.; Yao, Y. Interlayer-Expanded Molybdenum Disulfide Nanocomposites for Electrochemical Magnesium Storage. *Nano Lett.* **2015**, *15*, 2194–2202.

(123) Banerjee, S.; Pati, S. K. Anodic Performance of Black Phosphorus in Magnesium-Ion Batteries: The Significance of Mg–P Bond-Synergy. *Chem. Commun.* **2016**, *52*, 8381–8384.

(124) Yoo, H. D.; Shterenberg, I.; Gofer, Y.; Gershinsky, G.; Pour, N.; Aurbach, D. Mg Rechargeable Batteries: An on-Going Challenge. *Energy Environ. Sci.* **2013**, *6*, 2265.

(125) Wu, D.; Li, X.; Xu, B.; Twu, N.; Liu, L.; Ceder, G. NaTiO2: A Layered Anode Material for Sodium-Ion Batteries. *Energy Environ. Sci.* **2015**, *8*, 195–202.

(126) Greeley, J.; Jaramillo, T. F.; Bonde, J.; Chorkendorff, I. B.; Nørskov, J. K. Computational High-Throughput Screening of Electrocatalytic Materials for Hydrogen Evolution. *Nat. Mater.* **2006**, *5*, 909–913.

(127) Morales-Guio, C. G.; Stern, L.-A.; Hu, X. Nanostructured Hydrotreating Catalysts for Electrochemical Hydrogen Evolution. *Chem. Soc. Rev.* **2014**, *43*, 6555.

(128) Crabtree, G. W.; Dresselhaus, M. S.; Buchanan, M. V. The Hydrogen Economy. *Phys. Today* **2004**, *57*, 39–44.

(129) Yang, J.; Shin, H. S. Recent Advances in Layered Transition Metal Dichalcogenides for Hydrogen Evolution Reaction. *J. Mater. Chem. A* **2014**, *2*, 5979–5985.

(130) Yan, Y.; Xia, B.; Xu, Z.; Wang, X. Recent Development of Molybdenum Sulfides as Advanced Electrocatalysts for Hydrogen Evolution Reaction. *ACS Catal.* **2014**, *4*, 1693–1705.

(131) Merki, D.; Hu, X. Recent Developments of Molybdenum and Tungsten Sulfides as Hydrogen Evolution Catalysts. *Energy Environ. Sci.* **2011**, *4*, 3878.

(132) Hinnemann, B.; Moses, P. G.; Bonde, J.; Jørgensen, K. P.; Nielsen, J. H.; Horch, S.; Chorkendorff, I.; Nørskov, J. K. Biomimetic Hydrogen Evolution: MoS 2 Nanoparticles as Catalyst for Hydrogen Evolution. *J. Am. Chem. Soc.* **2005**, *127*, 5308–5309.

(133) Xie, J.; Zhang, J.; Li, S.; Grote, F.; Zhang, X.; Zhang, H.; Wang, R.; Lei, Y.; Pan, B.; Xie, Y. Controllable Disorder Engineering in Oxygen-Incorporated MoS 2 Ultrathin Nanosheets for Efficient Hydrogen Evolution. *J. Am. Chem. Soc.* **2013**, *135*, 17881–17888.

(134) Wang, H.; Lu, Z.; Xu, S.; Kong, D.; Cha, J. J.; Zheng, G.; Hsu, P.-C.; Yan, K.; Bradshaw, D.; Prinz, F. B.; *et al.* Electrochemical Tuning of Vertically Aligned MoS2 Nanofilms and Its Application in Improving Hydrogen Evolution Reaction. *Proc. Natl. Acad. Sci.* **2013**, *110*, 19701–19706.

(135) Merki, D.; Vrubel, H.; Rovelli, L.; Fierro, S.; Hu, X. Fe, Co, and Ni Ions Promote the Catalytic Activity of Amorphous Molybdenum Sulfide Films for Hydrogen Evolution. *Chem. Sci.* **2012**, *3*, 2515.

(136) Merki, D.; Fierro, S.; Vrubel, H.; Hu, X. Amorphous Molybdenum Sulfide Films as

Catalysts for Electrochemical Hydrogen Production in Water. *Chem. Sci.* **2011**, *2*, 1262–1267.

(137) Jaramillo, T. F.; Bonde, J.; Zhang, J.; Ooi, B.-L.; Andersson, K.; Ulstrup, J.; Chorkendorff, I. Hydrogen Evolution on Supported Incomplete Cubane-Type [Mo 3 S 4] 4+ Electrocatalysts. *J. Phys. Chem. C* **2008**, *112*, 17492–17498.

(138) Chen, Z.; Cummins, D.; Reinecke, B. N.; Clark, E.; Sunkara, M. K.; Jaramillo, T. F. Core–shell MoO 3 –MoS 2 Nanowires for Hydrogen Evolution: A Functional Design for Electrocatalytic Materials. *Nano Lett.* **2011**, *11*, 4168–4175.

(139) Kibsgaard, J.; Chen, Z.; Reinecke, B. N.; Jaramillo, T. F. Engineering the Surface Structure of MoS2 to Preferentially Expose Active Edge Sites for Electrocatalysis. *Nat. Mater.* **2012**, *11*, 963–969.

(140) Kibsgaard, J.; Jaramillo, T. F.; Besenbacher, F. Building an Appropriate Active-Site Motif into a Hydrogen-Evolution Catalyst with Thiomolybdate [Mo3S13]2− Clusters. *Nat. Chem.* **2014**, *6*, 248–253.

(141) Lukowski, M. A.; Daniel, A. S.; Meng, F.; Forticaux, A.; Li, L.; Jin, S. Enhanced Hydrogen Evolution Catalysis from Chemically Exfoliated Metallic MoS 2 Nanosheets. *J. Am. Chem. Soc.* **2013**, *135*, 10274–10277.

(142) Tsai, C.; Abild-Pedersen, F.; Nørskov, J. K. Tuning the MoS 2 Edge-Site Activity for Hydrogen Evolution via Support Interactions. *Nano Lett.* **2014**, *14*, 1381–1387.

(143) Li, Y.; Wang, H.; Xie, L.; Liang, Y.; Hong, G.; Dai, H. MoS 2 Nanoparticles Grown on Graphene: An Advanced Catalyst for the Hydrogen Evolution Reaction. *J. Am. Chem. Soc.* **2011**, *133*, 7296–7299.

(144) Yang, J.; Voiry, D.; Ahn, S. J.; Kang, D.; Kim, A. Y.; Chhowalla, M.; Shin, H. S. Two-Dimensional Hybrid Nanosheets of Tungsten Disulfide and Reduced Graphene Oxide as Catalysts for Enhanced Hydrogen Evolution. *Angew. Chemie Int. Ed.* **2013**, *52*, 13751–13754.

(145) Chen, J.-R.; Odenthal, P. M.; Swartz, A. G.; Floyd, G. C.; Wen, H.; Luo, K. Y.; Kawakami, R. K. Control of Schottky Barriers in Single Layer MoS 2 Transistors with Ferromagnetic Contacts. *Nano Lett.* **2013**, *13*, 3106–3110.

(146) Das, S.; Chen, H.-Y.; Penumatcha, A. V.; Appenzeller, J. High Performance Multilayer MoS 2 Transistors with Scandium Contacts. *Nano Lett.* **2013**, *13*, 100–105.

(147) Yoon, Y.; Ganapathi, K.; Salahuddin, S. How Good Can Monolayer MoS 2 Transistors Be? *Nano Lett.* **2011**, *11*, 3768–3773.

(148) Popov, I.; Seifert, G.; Tománek, D. Designing Electrical Contacts to MoS2 Monolayers: A Computational Study. *Phys. Rev. Lett.* **2012**, *108*, 156802.

(149) Liu, H.; Neal, A. T.; Ye, P. D. Channel Length Scaling of MoS 2 MOSFETs. *ACS Nano* **2012**, *6*, 8563–8569.

(150) Liu, H.; Si, M.; Deng, Y.; Neal, A. T.; Du, Y.; Najmaei, S.; Ajayan, P. M.; Lou, J.; Ye, P. D. Switching Mechanism in Single-Layer Molybdenum Disulfide Transistors: An Insight into Current Flow across Schottky Barriers. *ACS Nano* **2014**, *8*, 1031–1038.

(151) Kaushik, N.; Nipane, A.; Basheer, F.; Dubey, S.; Grover, S.; Deshmukh, M. M.; Lodha, S. Schottky Barrier Heights for Au and Pd Contacts to MoS2. *Appl. Phys.*

Lett. **2014**, *105*, 113505.

(152) Liu, H.; Si, M.; Najmaei, S.; Neal, A. T.; Du, Y.; Ajayan, P. M.; Lou, J.; Ye, P. D. Statistical Study of Deep Submicron Dual-Gated Field-Effect Transistors on Monolayer Chemical Vapor Deposition Molybdenum Disulfide Films. *Nano Lett.* **2013**, *13*, 2640–2646.

(153) Allain, A.; Kang, J.; Banerjee, K.; Kis, A. Electrical Contacts to Two-Dimensional Semiconductors. *Nat. Mater.* **2015**, *14*, 1195–1205.

(154) Kappera, R.; Voiry, D.; Yalcin, S. E.; Jen, W.; Acerce, M.; Torrel, S.; Branch, B.; Lei, S.; Chen, W.; Najmaei, S.; *et al.* Metallic 1T Phase Source/drain Electrodes for Field Effect Transistors from Chemical Vapor Deposited MoS 2. *APL Mater.* **2014**, *2*, 92516.

(155) Liao, L.; Zhu, J.; Bian, X.; Zhu, L.; Scanlon, M. D.; Girault, H. H.; Liu, B. MoS 2 Formed on Mesoporous Graphene as a Highly Active Catalyst for Hydrogen Evolution. *Adv. Funct. Mater.* **2013**, *23*, 5326–5333.

(156) Chang, Y.-H.; Lin, C.-T.; Chen, T.-Y.; Hsu, C.-L.; Lee, Y.-H.; Zhang, W.; Wei, K.-H.; Li, L.-J. Highly Efficient Electrocatalytic Hydrogen Production by MoS X Grown on Graphene-Protected 3D Ni Foams. *Adv. Mater.* **2013**, *25*, 756–760.

(157) Komsa, H.-P.; Kotakoski, J.; Kurasch, S.; Lehtinen, O.; Kaiser, U.; Krasheninnikov, A. V. Two-Dimensional Transition Metal Dichalcogenides under Electron Irradiation: Defect Production and Doping. *Phys. Rev. Lett.* **2012**, *109*, 35503.

(158) Zhou, W.; Zou, X.; Najmaei, S.; Liu, Z.; Shi, Y.; Kong, J.; Lou, J.; Ajayan, P. M.; Yakobson, B. I.; Idrobo, J.-C. Intrinsic Structural Defects in Monolayer Molybdenum Disulfide. *Nano Lett.* **2013**, *13*, 2615–2622.

(159) Hong, J.; Hu, Z.; Probert, M.; Li, K.; Lv, D.; Yang, X.; Gu, L.; Mao, N.; Feng, Q.; Xie, L.; *et al.* Exploring Atomic Defects in Molybdenum Disulphide Monolayers. *Nat. Commun.* **2015**, *6*, 6293.

(160) Kong, D.; Wang, H.; Cha, J. J.; Pasta, M.; Koski, K. J.; Yao, J.; Cui, Y. Synthesis of MoS 2 and MoSe 2 Films with Vertically Aligned Layers. *Nano Lett.* **2013**, *13*, 1341–1347.

(161) Yang, L.; Hong, H.; Fu, Q.; Huang, Y.; Zhang, J.; Cui, X.; Fan, Z.; Liu, K.; Xiang, B. Single-Crystal Atomic-Layered Molybdenum Disulfide Nanobelts with High Surface Activity. *ACS Nano* **2015**, *9*, 6478–6483.

(162) Dong, L.; Lou, J.; Shenoy, V. B. Large In-Plane and Vertical Piezoelectricity in Janus Transition Metal Dichalchogenides. *ACS Nano* **2017**, *11*, 8242–8248.

(163) Kresse, G.; Joubert, D. From Ultrasoft Pseudopotentials to the Projector Augmented-Wave Method. *Phys. Rev. B* **1999**, *59*, 1758–1775.

(164) Monkhorst, H. J.; Pack, J. D. Special Points for Brillouin-Zone Integrations. *Phys. Rev. B* **1976**, *13*, 5188–5192.

(165) Wellendorff, J.; Lundgaard, K. T.; Møgelhøj, A.; Petzold, V.; Landis, D. D.; Nørskov, J. K.; Bligaard, T.; Jacobsen, K. W. Density Functionals for Surface Science: Exchange-Correlation Model Development with Bayesian Error Estimation. *Phys. Rev. B* **2012**, *85*, 235149.

(166) Wang, H.; Yuan, H.; Sae Hong, S.; Li, Y.; Cui, Y. Physical and Chemical Tuning of Two-Dimensional Transition Metal Dichalcogenides. *Chem. Soc. Rev.* **2015**, *44*,

2664–2680.

(167) Tsai, C.; Chan, K.; Abild-Pedersen, F.; Nørskov, J. K. Active Edge Sites in MoSe2 and WSe2 Catalysts for the Hydrogen Evolution Reaction: A Density Functional Study. *Phys. Chem. Chem. Phys.* **2014**, *16*, 13156–13164.

(168) Splendiani, A.; Sun, L.; Zhang, Y.; Li, T.; Kim, J.; Chim, C. Y.; Galli, G.; Wang, F. Emerging Photoluminescence in Monolayer MoS2. *Nano Lett.* **2010**, *10*, 1271–1275.

(169) Li, F.; Wei, W.; Zhao, P.; Huang, B.; Dai, Y. Electronic and Optical Properties of Pristine and Vertical and Lateral Heterostructures of Janus MoSSe and WSSe. *J. Phys. Chem. Lett.* **2017**, *8*, 5959–5965.

(170) Landau, L. D., Lifshitž, E. M., Sykes, J. B. & Reid, W. H. *Course of Theoretical Physics: Theory of Elasticity*; Butterworth-Heinemann, 1986.

(171) Shenoy, V. B.; Reddy, C. D.; Zhang, Y.-W. Spontaneous Curling of Graphene Sheets with Reconstructed Edges. *ACS Nano* **2010**, *4*, 4840–4844.

(172) Tang, S.; Wang, H.; Zhang, Y.; Li, A.; Xie, H.; Liu, X.; Liu, L.; Li, T.; Huang, F.; Xie, X.; *et al.* Precisely Aligned Graphene Grown on Hexagonal Boron Nitride by Catalyst Free Chemical Vapor Deposition. *Sci. Rep.* **2013**, *3*, 2666.

(173) Xue, J.; Sanchez-Yamagishi, J.; Bulmash, D.; Jacquod, P.; Deshpande, A.; Watanabe, K.; Taniguchi, T.; Jarillo-Herrero, P.; LeRoy, B. J. Scanning Tunnelling Microscopy and Spectroscopy of Ultra-Flat Graphene on Hexagonal Boron Nitride. *Nat. Mater.* **2011**, *10*, 282–285.

(174) Yang, W.; Chen, G.; Shi, Z.; Liu, C.-C.; Zhang, L.; Xie, G.; Cheng, M.; Wang, D.; Yang, R.; Shi, D.; *et al.* Epitaxial Growth of Single-Domain Graphene on Hexagonal Boron Nitride. *Nat. Mater.* **2013**, *12*, 792–797.

(175) Colson, J. W.; Dichtel, W. R. Rationally Synthesized Two-Dimensional Polymers. *Nat. Chem.* **2013**, *5*, 453–465.

(176) Carter, S. A.; Angelopoulos, M.; Karg, S.; Brock, P. J.; Scott, J. C. Polymeric Anodes for Improved Polymer Light-Emitting Diode Performance. *Appl. Phys. Lett.* **1997**, *70*, 2067–2069.

(177) Arias, A. C.; Granström, M.; Thomas, D. S.; Petritsch, K.; Friend, R. H. Doped Conducting-Polymer–semiconducting-Polymer Interfaces: Their Use in Organic Photovoltaic Devices. *Phys. Rev. B* **1999**, *60*, 1854–1860.

(178) Côté, A. P.; Benin, A. I.; Ockwig, N. W.; O'Keeffe, M.; Matzger, A. J.; Yaghi, O. M. Porous, Crystalline, Covalent Organic Frameworks. *Science* **2005**, *310*, 1166–1170.

(179) Spitler, E. L.; Koo, B. T.; Novotney, J. L.; Colson, J. W.; Uribe-Romo, F. J.; Gutierrez, G. D.; Clancy, P.; Dichtel, W. R. A 2D Covalent Organic Framework with 4.7-Nm Pores and Insight into Its Interlayer Stacking. *J. Am. Chem. Soc.* **2011**, *133*, 19416–19421.

(180) Wan, S.; Guo, J.; Kim, J.; Ihee, H.; Jiang, D. A Photoconductive Covalent Organic Framework: Self-Condensed Arene Cubes Composed of Eclipsed 2D Polypyrene Sheets for Photocurrent Generation. *Angew. Chemie* **2009**, *121*, 5547–5550.

(181) Wan, S.; Guo, J.; Kim, J.; Ihee, H.; Jiang, D. A Belt-Shaped, Blue Luminescent, and Semiconducting Covalent Organic Framework. *Angew. Chemie - Int. Ed.* **2008**, *47*,

8826–8830.

(182) Ding, H.; Li, Y.; Hu, H.; Sun, Y.; Wang, J.; Wang, C.; Wang, C.; Zhang, G.; Wang, B.; Xu, W.; *et al.* A Tetrathiafulvalene-Based Electroactive Covalent Organic Framework. *Chem. - A Eur. J.* **2014**, *20*, 14614–14618.

(183) Spitler, E. L.; Dichtel, W. R. Lewis Acid-Catalysed Formation of Two-Dimensional Phthalocyanine Covalent Organic Frameworks. *Nat. Chem.* **2010**, *2*, 672–677.

(184) Ding, X.; Guo, J.; Feng, X.; Honsho, Y.; Guo, J.; Seki, S.; Maitarad, P.; Saeki, A.; Nagase, S.; Jiang, D. Synthesis of Metallophthalocyanine Covalent Organic Frameworks That Exhibit High Carrier Mobility and Photoconductivity. *Angew. Chemie Int. Ed.* **2011**, *50*, 1289–1293.

(185) Ding, X.; Chen, L.; Honsho, Y.; Feng, X.; Saengsawang, O.; Guo, J.; Saeki, A.; Seki, S.; Irle, S.; Nagase, S.; *et al.* An N-Channel Two-Dimensional Covalent Organic Framework. *J. Am. Chem. Soc.* **2011**, *133*, 14510–14513.

(186) Gutzler, R.; Perepichka, D. F. π-Electron Conjugation in Two Dimensions. *J. Am. Chem. Soc.* **2013**, *135*, 16585–16594.

(187) Wang, H.-X.; Wang, Q.; Zhou, K.-G.; Zhang, H.-L. Graphene in Light: Design, Synthesis and Applications of Photo-Active Graphene and Graphene-like Materials. *Small* **2013**, *9*, 1266–1283.

(188) Bonaccorso, F.; Colombo, L.; Yu, G.; Stoller, M.; Tozzini, V.; Ferrari, a. C.; Ruoff, R. S.; Pellegrini, V. Graphene, Related Two-Dimensional Crystals, and Hybrid Systems for Energy Conversion and Storage. *Science (80-.).* **2015**, *347*, 1246501–1246501.

(189) Geim, A. K. Graphene: Status and Prospects. *Science* **2009**, *324*, 1530–1534.

(190) Adjizian, J.-J.; Briddon, P.; Humbert, B.; Duvail, J.-L.; Wagner, P.; Adda, C.; Ewels, C. Dirac Cones in Two-Dimensional Conjugated Polymer Networks. *Nat. Commun.* **2014**, *5*, 5842.

(191) Kishigi, K.; Ueno, K.; Miyamoto, E.; Hasegawa, Y. Dirac Cones on the Generalized Honeycomb Lattice. *J. Phys. Conf. Ser.* **2011**, *334*, 12047.

(192) Nagai, A.; Chen, X.; Feng, X.; Ding, X.; Guo, Z.; Jiang, D. A Squaraine-Linked Mesoporous Covalent Organic Framework. *Angew. Chem. Int. Ed.* **2013**, *52*, 3770–3774.

(193) Dogru, M.; Bein, T. On the Road towards Electroactive Covalent Organic Frameworks. *Chem. Commun.* **2014**, *50*, 5531–5546.

(194) Lukose, B.; Kuc, A.; Frenzel, J.; Heine, T. On the Reticular Construction Concept of Covalent Organic Frameworks. *Beilstein J. Nanotechnol.* **2010**, *1*, 60–70.

(195) Shockley, W.; Queisser, H. J. Detailed Balance Limit of Efficiency of P-N Junction Solar Cells. *J. Appl. Phys.* **1961**, *32*, 510–519.

(196) Van Mullekom, H. A. M.; Vekemans, J. A. J. M.; Havinga, E. E.; Meijer, E. W. Developments in the Chemistry and Band Gap Engineering of Donor–acceptor Substituted Conjugated Polymers. *Mater. Sci. Eng. R Reports* **2001**, *32*, 1–40.

(197) Feng, X.; Ding, X.; Jiang, D. Covalent Organic Frameworks. *Chem. Soc. Rev.* **2012**, *41*, 6010–6022.

(198) Nagai, A.; Guo, Z.; Feng, X.; Jin, S.; Chen, X.; Ding, X.; Jiang, D. Pore Surface Engineering in Covalent Organic Frameworks. *Nat. Commun.* **2011**, *2*, 1–8.

(199) Feng, X.; Chen, L.; Honsho, Y.; Saengsawang, O.; Liu, L.; Wang, L.; Saeki, A.; Irle, S.; Seki, S.; Dong, Y.; *et al.* An Ambipolar Conducting Covalent Organic Framework with Self-Sorted and Periodic Electron Donor-Acceptor Ordering. *Adv. Mater.* **2012**, *24*, 3026–3031.

(200) Dogru, M.; Handloser, M.; Auras, F.; Kunz, T.; Medina, D.; Hartschuh, A.; Knochel, P.; Bein, T. A Photoconductive Thienothiophene-Based Covalent Organic Framework Showing Charge Transfer Towards Included Fullerene. *Angew. Chem. Int. Ed.* **2013**, *125*, 2992–2996.

(201) Kresse, G.; Hafner, J. Ab Initio Molecular-Dynamics Simulation of the Liquid-Metal–amorphous-Semiconductor Transition in Germanium. *Phys. Rev. B* **1994**, *49*, 14251–14269.

(202) Kresse, G.; Furthmüller, J. Efficiency of Ab-Initio Total Energy Calculations for Metals and Semiconductors Using a Plane-Wave Basis Set. *Comput. Mater. Sci.* **1996**, *6*, 15–50.

(203) Tkatchenko, A.; Scheffler, M. Accurate Molecular Van Der Waals Interactions from Ground-State Electron Density and Free-Atom Reference Data. *Phys. Rev. Lett.* **2009**, *102*, 73005.

(204) Lukose, B.; Kuc, A.; Heine, T. The Structure of Layered Covalent-Organic Frameworks. *Chemistry* **2011**, *17*, 2388–2392.

(205) Gorte, R. J. Ceria in Catalysis: From Automotive Applications to the Water-Gas Shift Reaction. *AIChE J.* **2010**, *56*, 1126–1135.

(206) Sugiura, M. Oxygen Storage Materials for Automotive Catalysts: Ceria-Zirconia Solid Solutions. *Catal. Surv. from Asia* **2003**, *7*, 77–87.

(207) Adler, S. B.; Lane, J.; Steele, B. Electrode Kinetics of Porous Mixed-Conducting Oxygen Electrodes. *J. Electrochem. Soc.* **1996**, *143*, 3554.

(208) Dyer, P. N.; Richards, R. E.; Russek, S. L.; Taylor, D. M. Ion Transport Membrane Technology for Oxygen Separation and Syngas Production. *Solid State Ionics* **2000**, *134*, 21–33.

(209) Sugiura, M.; Ozawa, M.; Suda, A.; Suzuki, T.; Kanazawa, T. Development of Innovative Three-Way Catalysts Containing Ceria-Zirconia Solid Solutions with High Oxygen Storage/release Capacity. *Bull. Chem. Soc. Jpn.* **2005**, *78*, 752–767.

(210) Shelef, M.; Graham, G. W.; McCABE, R. W. CERIA AND OTHER OXYGEN STORAGE COMPONENTS IN AUTOMOTIVE CATALYSTS. *Catal. Sci. Ser.* **2002**, *2*, 343--372.

(211) Kašpar, J.; Fornasiero, P.; Hickey, N. Automotive Catalytic Converters: Current Status and Some Perspectives. In *Catalysis Today*; 2003; Vol. 77, pp. 419–449.

(212) Bunluesin, T.; Gorte, R. J.; Graham, G. W. Studies of the Water-Gas-Shift Reaction on Ceria-Supported Pt, Pd, and Rh: Implications for Oxygen-Storage Properties. *Appl. Catal. B Environ.* **1998**, *15*, 107–114.

(213) Liu, X.; Ruettinger, W.; Xu, X.; Farrauto, R. Deactivation of Pt/CeO2 Water-Gas Shift Catalysts due to Shutdown/startup Modes for Fuel Cell Applications. *Appl. Catal. B Environ.* **2005**, *56*, 69–75.

(214) Craciun, R.; Shereck, B.; Gorte, R. J. Kinetic Studies of Methane Steam Reforming on Ceria-Supported Pd. *Catal. Letters* **1998**, *51*, 149–153.

(215) Heck, R. M.; Farrauto, R. J. Automobile Exhaust Catalysts. *Applied Catalysis A: General*, 2001, *221*, 443–457.

(216) Marrocchelli, D.; Bishop, S. R.; Tuller, H. L.; Yildiz, B. Understanding Chemical Expansion in Non-Stoichiometric Oxides: Ceria and Zirconia Case Studies. *Adv. Funct. Mater.* **2012**, *22*, 1958–1965.

(217) Adler, S. B. Chemical Expansivity of Electrochemical Ceramics. *J. Am. Ceram. Soc.* **2001**, *84*, 2117–2119.

(218) Bishop, S. R.; Duncan, K. L.; Wachsman, E. D. Thermo-Chemical Expansion in Strontium-Doped Lanthanum Cobalt Iron Oxide. *J. Am. Ceram. Soc.* **2010**, *93*, 4115–4121.

(219) Kuebler, J.; Vogt, U. F.; Haberstock, D.; Sfeir, J.; Mai, A.; Hocker, T.; Roos, M.; Harnisch, U. Simulation and Validation of Thermo-Mechanical Stresses in Planar SOFCs. *Fuel Cells* **2010**, *10*, 1066–1073.

(220) Atkinson, A.; Ramos, T. Chemically-Induced Stresses in Gadolinium-Doped Ceria Solid Oxide Fuel Cell Electrolytes. *Solid State Ionics*, 1997, *95*, 249–258.

(221) Blond, E.; Richet, N. Thermomechanical Modelling of Ion-Conducting Membrane for Oxygen Separation. *J. Eur. Ceram. Soc.* **2008**, *28*, 793–801.

(222) Bishop, S. R.; Tuller, H. L.; Kuru, Y.; Yildiz, B. Chemical Expansion of Nonstoichiometric Pr0.1Ce0.9O2−δ: Correlation with Defect Equilibrium Model. *J. Eur. Ceram. Soc.* **2011**, *31*, 2351–2356.

(223) Sato, K.; Yashiro, K.; Kawada, T.; Yugami, H.; Hashida, T.; Mizusaki, J. Fracture Process of Nonstoichiometric Oxide Based Solid Oxide Fuel Cell under Oxidizing/reducing Gradient Conditions. *J. Power Sources* **2010**, *195*, 5481–5486.

(224) Swaminathan, N.; Qu, J.; Sun, Y. An Electrochemomechanical Theory of Defects in Ionic Solids. I. Theory. *Philos. Mag.* **2007**, *87*, 1705–1721.

(225) Wang, Y.; Duncan, K.; Wachsman, E.; Ebrahimi, F. The Effect of Oxygen Vacancy Concentration on the Elastic Modulus of Fluorite-Structured Oxides. *Solid State Ionics* **2007**, *178*, 53–58.

(226) Kossoy, A.; Frenkel, A. I.; Wang, Q.; Wachtel, E.; Lubomirsky, I. Local Structure and Strain-Induced Distortion in Ce0.8Gd0.2O1.9. *Adv. Mater.* **2010**, *22*, 1659–1662.

(227) Kossoy, A.; Feldman, Y.; Korobko, R.; Wachtel, E.; Lubomirsky, I.; Maier, J. Influence of Point-Defect Reaction Kinetics on the Lattice Parameter of Ce0.8Gd0.2O1.9. *Adv. Funct. Mater.* **2009**, *19*, 634–641.

(228) Kuru, Y.; Bishop, S. R.; Kim, J.-J.; Yildiz, B.; Tuller, H. L. Chemical Expansion and Frozen-In Oxygen Vacancies in Pr-Doped Ceria. *ECS Trans.* **2011**, *35*, 1131–1136.

(229) Mogensen, M.; Sammes, N.; Tompsett, G. Physical, Chemical and Electrochemical Properties of Pure and Doped Ceria. *Solid State Ionics* **2000**, *129*, 63–94.

(230) Armstrong, T. R.; Stevenson, J. W.; Pederson, L. R.; Raney, P. E. Dimensional Instability of Doped Lanthanum Chromite. *J. Electrochem. Soc.* **1996**, *143*, 2919.

(231) Zinkevich, M.; Djurovic, D.; Aldinger, F. Thermodynamic Modelling of the Cerium-Oxygen System. *Solid State Ionics* **2006**, *177*, 989–1001.

(232) Ling, S. High-Concentration Point-Defect Chemistry: Statistical-Thermodynamic

Approach Applied to Nonstoichiometric Cerium Dioxides. *Physical Review B*, 1994, *49*, 864–880.

(233) Xu, Y.; Shelton, W. A. O2 Reduction by Lithium on Au(111) and Pt(111). *J. Chem. Phys.* **2010**, *133*, 24703.

(234) Bishop, S. R.; Marrocchelli, D.; Chatzichristodoulou, C.; Perry, N. H.; Mogensen, M. B.; Tuller, H. L.; Wachsman, E. D. Chemical Expansion: Implications for Electrochemical Energy Storage and Conversion Devices. *Annu. Rev. Mater. Res.* **2014**, *44*, 205–239.

(235) Sheldon, B. W.; Shenoy, V. B. Space Charge Induced Surface Stresses: Implications in Ceria and Other Ionic Solids. *Phys. Rev. Lett.* **2011**, *106*, 216104.

(236) Skorodumova, N.; Ahuja, R.; Simak, S.; Abrikosov, I.; Johansson, B.; Lundqvist, B. Electronic, Bonding, and Optical Properties of CeO2 and Ce2O3 from First Principles. *Phys. Rev. B* **2001**, *64*, 115108.

(237) Shannon, R. D. Revised Effective Ionic Radii and Systematic Studies of Interatomic Distances in Halides and Chalcogenides. *Acta Crystallogr. Sect. A* **1976**, *32*, 751–767.

(238) Goff, J. P.; Hayes, W.; Hull, S.; Hutchings, M. T.; Clausen, K. N. Defect Structure of Yttria-Stabilized Zirconia and Its Influence on the Ionic Conductivity at Elevated Temperatures. *Phys. Rev. B* **1999**, *59*, 14202–14219.

(239) Dholabhai, P. P.; Adams, J. B.; Crozier, P.; Sharma, R. Oxygen Vacancy Migration in Ceria and Pr-Doped Ceria: A DFT+U Study. *J. Chem. Phys.* **2010**, *132*, 94104.

(240) Gillan, M. J. The Elastic Dipole Tensor for Point Defects in Ionic Crystals. *J. Phys. C Solid State Phys.* **1984**, *17*, 1473–1488.

(241) Wachtel, E.; Lubomirsky, I. The Elastic Modulus of Pure and Doped Ceria. *Scr. Mater.* **2011**, *65*, 112–117.

(242) Xu, H.; Behera, R. K.; Wang, Y.; Ebrahimi, F.; Sinnott, S. B.; Wachsman, E. D.; Phillpot, S. R. A Critical Assessment of Interatomic Potentials for Ceria with Application to Its Elastic Properties. *Solid State Ionics* **2010**, *181*, 551–556.

(243) Hull, S.; Norberg, S. T. T.; Ahmed, I.; Eriksson, S. G. G.; Marrocchelli, D.; Madden, P. a. A. Oxygen Vacancy Ordering within Anion-Deficient Ceria. *J. Solid State Chem.* **2009**, *182*, 2815–2821.

(244) Chiang, H.; Blumenthal, R. N.; Fournelle, R.; Foumelle, R. A. A High Temperature Lattice Parameter and Dilatometer Study of the Defect Structure of Nonstoichiometric Cerium Dioxide. *Solid State Ionics* **1993**, *66*, 85–95.

(245) Bishop, S. R. R.; Duncan, K. L. L.; Wachsman, E. D. D. Defect Equilibria and Chemical Expansion in Non-Stoichiometric Undoped and Gadolinium-Doped Cerium Oxide. *Electrochim. Acta* **2009**, *54*, 1436–1443.

(246) Kofstad, P.; Hed, A. Z. Defect Structure Model for Nonstoichiometric CeO2. *J. Am. Ceram. Soc.* **1967**, *50*, 681–682.

(247) Kevane, C. Oxygen Vacancies and Electrical Conduction in Metal Oxides. *Phys. Rev.* **1964**, *133*, A1431–A1436.

(248) Panlener, R. J.; Blumenthal, R. N.; Garnier, J. E. A Thermodynamic Study of Nonstoichiometric Cerium Dioxide. *J. Phys. Chem. Solids* **1975**, *36*, 1213–1222.

(249) Faber, J.; Seitz, M. A.; Mueller, M. H. Defect Characterization in CeO2−x at

Elevated temperatures—I. *J. Phys. Chem. Solids* **1976**, *37*, 903–907.

(250) Daubert, TE and Danner, R. Physical and Thermodynamic Properties of Pure Compounds: Data Compilation. *Hemisphere, New York* **1989**, *2001*.

(251) Tsunekawa, S.; Sahara, R.; Kawazoe, Y.; Ishikawa, K. Lattice Relaxation of Monosize CeO2−x Nanocrystalline Particles. *Appl. Surf. Sci.* **1999**, *152*, 53–56.

(252) Tsunekawa, S.; Ishikawa, K.; Li, Z.-Q.; Kawazoe, Y.; Kasuya, A. Origin of Anomalous Lattice Expansion in Oxide Nanoparticles. *Phys. Rev. Lett.* **2000**, *85*, 3440–3443.

(253) Mamontov, E.; Egami, T.; Pennsyl, V.; Brezny, R.; Koranne, M.; Grace, W. R.; Grace, C.; Da, V.; Tyagi, S. Lattice Defects and Oxygen Storage Capacity of Nanocrystalline Ceria and Ceria-Zirconia. *J. Phys. Chem. B* **2000**, *104*, 11110–11116.

(254) Cazorla, C.; Boronat, J. Simulation and Understanding of Atomic and Molecular Quantum Crystals. *Rev. Mod. Phys.* **2017**, *89*, 35003.

(255) Heyd, J.; Scuseria, G. E.; Ernzerhof, M. Hybrid Functionals Based on a Screened Coulomb Potential. *J. Chem. Phys.* **2003**, *118*, 8207–8215.

(256) Becke, A. D. Density-functional Thermochemistry. III. The Role of Exact Exchange. *J. Chem. Phys.* **1993**, *98*, 5648–5652.

(257) Perdew, J. P.; Ernzerhof, M.; Burke, K. Rationale for Mixing Exact Exchange with Density Functional Approximations. *J. Chem. Phys.* **1996**, *105*, 9982–9985.

(258) Zhao, Y.; Truhlar, D. G. The M06 Suite of Density Functionals for Main Group Thermochemistry, Thermochemical Kinetics, Noncovalent Interactions, Excited States, and Transition Elements: Two New Functionals and Systematic Testing of Four M06-Class Functionals and 12 Other Function. *Theor. Chem. Acc.* **2008**, *120*, 215–241.

(259) Grimme, S. Semiempirical GGA-Type Density Functional Constructed with a Long-Range Dispersion Correction. *J. Comput. Chem.* **2006**, *27*, 1787–1799.

(260) Grimme, S.; Antony, J.; Ehrlich, S.; Krieg, H. A Consistent and Accurate Ab Initio Parametrization of Density Functional Dispersion Correction (DFT-D) for the 94 Elements H-Pu. *J. Chem. Phys.* **2010**, *132*, 154104.

(261) VASP. The VASP Manual https://www.vasp.at/index.php/documentation (accessed Apr 5, 2018).

(262) Kim, S. J.; Choi, K.; Lee, B.; Kim, Y.; Hong, B. H. Materials for Flexible, Stretchable Electronics: Graphene and 2D Materials. *Annu. Rev. Mater. Res.* **2015**, *45*, 63–84.

(263) Li, Y.; Fu, Z.-Y.; Su, B. Hierarchically Structured Porous Materials for Energy Conversion and Storage. *Adv. Funct. Mater.* **2012**, *22*, 4634–4667.

(264) Nykvist, B.; Nilsson, M. Rapidly Falling Costs of Battery Packs for Electric Vehicles. *Nat. Clim. Chang.* **2015**, *5*, 329–332.

(265) Peng, L.; Zhu, Y.; Chen, D.; Ruoff, R. S.; Yu, G. Two-Dimensional Materials for Beyond-Lithium-Ion Batteries. *Adv. Energy Mater.* **2016**, *6*, 1–21.

(266) Vitek, V. Intrinsic Stacking Faults in Body-Centred Cubic Crystals. *Philos. Mag.* **1968**, *18*, 773–786.

(267) Kim, T.; Vohs, J. M.; Gorte, R. J. Thermodynamic Investigation of the Redox

Properties of Ceria−Zirconia Solid Solutions. *Ind. Eng. Chem. Res.* **2006**, *45*, 5561–5565.